Earthquakes, elevations and continental plateaux: An investigation into the absence of large thrust earthquakes at high elevations within fold-and-thrust belts.

CATHERINE REBECCA MARIE GODDARD

Earthquakes, elevations and continental plateaux

An investigation into the absence of large thrust earthquakes at high elevations within fold-and-thrust belts.

Catherine Rebecca Marie Goddard

This thesis was submitted to the University of Durham in full fulfilment of the requirements for the degree of Master of Science by Research

Department of Earth Science

Durham University

2016

Abstract

Large thrust earthquakes (M ≥ 5) are rare at high elevations in continental fold-and-thrust belts. For example, Nissen et al's (2011) work infers a cut-off in M ≥ 5 earthquakes at ~ 1250 m in the Zagros. Data from the Zagros, Himalayas, Qilian Shan and Longmen Shan fold-and-thrust belts are analysed to test three hypotheses for this cut-off phenomenon. (1) Fold-and-thrust belts deform via the critical Coulomb wedge model, which favours thrusting at lower elevations. (2) Fold-and-thrust belts are controlled by minimum work processes, which suppress thrusts at high elevations. (3) A thickened ductile zone within the sedimentary layer of fold-and-thrust belts inhibits earthquake propagation.

Earthquake magnitude vs. elevation analysis revealed an abrupt cut-off in M ≥ 5 earthquakes at threshold elevations which were dependant on the locality. These elevations ranged from 1250 m in the Zagros to 4000 m in the Qilian Shan. Cut-offs were then compared to their corresponding slope geometries determined by swath profile analysis. Two significant changes in gradient were identified; one at the edge of the plateau and one correlating with the elevation of the earthquake cut-offs, where the slope gradient decreased but remained positive.

Brittle-ductile transitions, first in the basal decollement and then in the lower wedge, are considered to account for such major variations in the slope geometry (Hypothesis 1). The abrupt cut-off in M ≤ 5 earthquakes at the second gradient change supports the theory that the fold-and-thrust belts have a limiting elevation, defined by Gravitational Potential Energy (Hypothesis 2). For this reason, a hybrid of Hypotheses 1 and 2 is proposed to explain the reduction in M ≥ 5 earthquakes with elevation, in which ductile deformation in the critical Coulomb wedge limits M ≥ 5 earthquakes, but convergence continues aseismically until the formation of a plateau with its height determined by minimum work processes.

To explore the relevance of Hypothesis 3, dual lithology triaxial loading experiments were conducted as an analogue to study the influence of brittle-ductile behaviour on fault propagation. Brittle faults were found to propagate aseismically into a ductile medium offering an explanation for the high elevation regions of aseismic convergence.

Table of Contents

List of Tables

List of Figures

Acknowledgements

Firstly, a huge thank you to my primary supervisor Prof. Mark Allen, without whose vision this project would never have existed. There are many things I have to thank him for, not least making available grant funding for the research project, supporting my attendance at two conferences, endless patience with me in the face of constant questioning and also his open door policy (which he may have lived to regret). I would also like to thank my co-supervisors Dr Nicola De Paola and Dr Stefan Nielsen for providing specialist advice and guidance in the areas of experimental rock mechanics and applied mathematics respectively. Additionally; for access to laboratory facilities and training me on their use. My experimental work also owes a lot to their PhD student Chris Harbord, for stimulating discussion and invaluable hands on advice when operating the equipment.

I owe a huge thank you to Dr Chris Saville whose help was above and beyond the call of duty and who effectively became an unofficial co-supervisor. Dr Eddie Dempsey made available the use of his microscope and was ever-helpful with the interpretation of micrographs. The thin sections were prepared at very short notice by Ian Chaplin who rose to the occasion without complaint. A collective thank you to all other members of the department, especially those who had the misfortune to occupy desks within earshot of mine. Their stimulating conversation, cups of coffee at just the right moment and myriad words of wisdom from those who have been through it all before were invaluable.

I owe a huge amount of gratitude to my family, in particular my parents, for providing all the elements of a post graduate life support system and for continual support and encouragement throughout my Masters.

Finally, there is little doubt that I would not have been able to complete this year successfully without the help of Jamie Schofield. His proof reading, advice and endless patience kept me going through even the most disheartening of moments.

Chapter 1

Introduction

1. Introduction

1.1 Project rationale

It has been observed that larger thrust earthquakes (M ≥ ~5) are rare at high elevations in continental fold-and-thrust belts. For example; the cut-off is at 1250 m in the Zagros fold-and-thrust belt (Nissen et al. 2011), while thrust events are rare above 3500 m in the Himalayas and other fold-and-thrust belts marginal to the Tibetan Plateau (Allen pers. comm.). A definitive explanation for this phenomenon has yet to be established, but various theories have been advanced. A reduction in thrust earthquakes has been linked to aspects of the critical Coulomb wedge model (Dahlen 1990) and also to a minimum work model (Molnar & Lyon-Caen 1988) which suggests that higher elevation regions resist major seismogenic thrusting due to the additional gravitational potential energy (G.P.E) associated with increasing the height of the plateau.

The Gutenberg-Richter frequency-magnitude relationship could mean that the lack of large thrust earthquakes is merely an artefact, or 'seismogenic gap', arising from too short an observation period (Scholz 1968). However, the frequency–magnitude relationship does not always hold. Segments of known major faults, such as the San Andreas, tend to rupture fairly regularly with fault-characteristic maximum magnitude events while small events tend to be less frequent than predicted by the Gutenberg-Richter relationship (Sibson 1989). Even if the lack of seismicity can be statistically justified as merely the consequence of too short an observation period, it is likely that in areas of such high earthquake activity dynamic stress transfer would have induced failure on any faults that were late in their seismic cycle (Freed 2005).

The destructive nature of large earthquakes, as demonstrated by the 8,000 fatalities of the 2015 Nepalese event (Fan & Shearer 2015), provides an imperative for developing knowledge of earthquake occurrence patterns and magnitude relationships. Therefore, any attempt to understand the controlling mechanisms of the distribution of high magnitude thrust earthquakes is of fundamental societal as well as scientific importance.

1.2 Context

This section reviews two models that have previously been put forward to explain the absence of large thrust earthquakes at high elevations in addition to introducing a new model proposed by Dr N. De Paola of Durham University.

1.2.1 The critical Coulomb wedge hypothesis

The simple fact that compressional fold-and-thrust belts worldwide tend to show the same structural features suggests the fundamental mechanics of continental deformation can be generalised (Masek & Duncan 1998). It has subsequently been accepted that regional topography in most foreland fold-and-thrust belts results from tectonic wedging of crustal rocks (Mouthereau et al. 2006) and that systems maintain this wedge-shaped, self-similar critical form during orogeny (Roe & Brandon 2011).

The classical critical Coulomb wedge model (Figure 1.1) describes an end-member situation where the detachment slips at a constant shear stress (Wang & Hu 2006), the strength of the wedge is limited by the Coulomb failure criterion and both the wedge and the base are

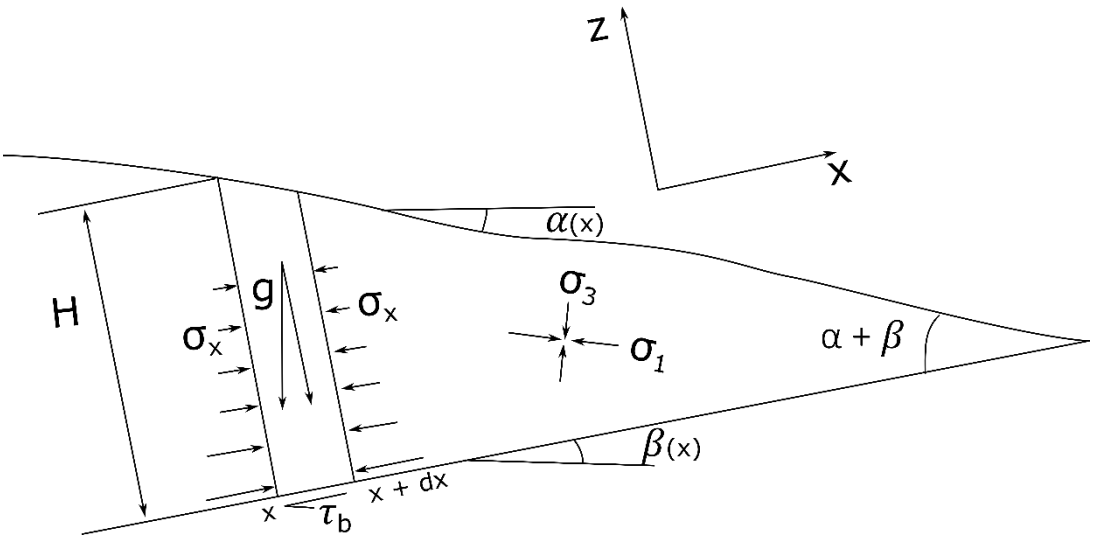

Figure 1.1: Schematic diagram of an idealised critical Coulomb wedge. Wedge material is subject to horizontal compression and is assumed to be everywhere on the verge of failure. The force balance on an arbitrary column of width dx is shown. Within the diagram, g refers to gravitational acceleration, H to the thickness of the wedge, α+β is the critical taper angle, τ_b is the shear stress along the basal decollement and σ_1 and σ_3 refer to the maximum and minimum principal stresses (Davis et al. 1983).

assumed to be constantly on the verge of failure (Mouthereau et al. 2006). A cohesionless and homogenous wedge (Davis et al. 1983) is assumed within most models and the basal decollement is considered to be consistently weaker than the material composing the wedge, providing a locus for stable sliding (Dahlen et al. 1984). Below this basal decollement minimal deformation is observed (Chapple 1978) and within the wedge deformation is found to be present in the form of imbricated thrust faults which verge towards the wedge toe (Dahlen 1990). The quasi –static balanced forces on an infinitesimal segment of the wedge between x and dx (Figure 1.1) in a thin –skinned model being pushed up a vertical incline can be approximated by the following equation:

$$\rho g H(\beta + \mu_B) + \frac{d}{dx}\int_0^H \sigma_{xx}\, dz \;\approx\; 0 \qquad \text{Eq. 1.1}$$

Where μ_B is the coefficient of basal friction and $\sigma_{xx} \approx \sigma_1$

The magnitude of the critical taper angle (Figure 1.1) is governed by the relative magnitudes of the frictional resistance of the basal plane and the compressive strength of the wedge material (Dahlen 1990) as described in the following equation:.

$$\alpha + \beta \approx \left(\frac{1 - \sin\emptyset}{1 + \sin\emptyset}\right)(\beta + \mu_B) \qquad \text{Eq. 1.2}$$

Where ø is the angle of internal friction

A change in either of these properties will, therefore, result in a change in the topographic gradient. An increase in the frictional resistance will result in an increase in taper angle whereas an increase in the wedge strength will decrease this angle (Dahlen 1990). In a homogenous wedge, with uniform compressive strength, it can be assumed that a change in surface slope must result from a change in the basal friction. To generalise; stable friction in a homogeneous wedge produces a constant critical taper whereas changes in the basal friction of the decollement or the strength of the wedge material will produce a critical wedge with a varying topographic slope (Miyakawa et al. 2010).

The standard critical Coulomb wedge theory nowhere directly addresses the reduction in thrust earthquakes at high elevations; however, it alludes to processes that may induce such a cut-off. Laboratory sandbox experiments demonstrated that the first faults form near the rigid buttress at the back of the incipient wedge but that active faulting then moves towards the toe (Dahlen 1990). Therefore, the lack of thrust earthquakes at high elevations could be due to more favourable shear stress for reverse faulting at the toe of the wedge.

An alternative argument is that the seismicity pattern is the result of a change in the deformation mechanism. The existence of a brittle-ductile transition at around 10-15 km depth ultimately limits the height of very wide fold-and-thrust belts and accretionary wedges. Succinctly; a non-eroding or slowly eroding wedge can only grow self-similar if the basal behaviour is purely frictional (Dahlen 1990). As thrust earthquakes are the major builders of topography, a reduction in thrust earthquakes can reasonably be inferred from a lack of topographic growth. The slope of the wedge should, therefore, decrease inland as the wedge thickness (H) increases (Figure 1.1) and the deformation mechanism transitions from brittle to ductile (Davis et al. 1983). Firstly, this change to distributed deformation will inhibit the seismicity occurring on the basal decollement and within the lower portion of the wedge (Williams et al. 1994). Secondly, without a sufficient surface slope, basal sliding cannot occur because the surface slope contributes to the stress state within the wedge and as a result yielding in the whole wedge will not take place (Chapple 1978). A schematic of the modified brittle-ductile critical Coulomb wedge is shown in Figure 1.2. If this brittle-ductile transition within the wedge results in the cut-off in $M \geq 5$ earthquakes then the loss of seismicity should also correlate to the change in slope or ‘plateau’ edge.

Despite regional similarities between various fold-and-thrust belts, the interior structural deformation varies significantly from wedge to wedge. The link between the critical Coulomb wedge model and the lack of large thrust earthquakes is hence still in need of further examination.

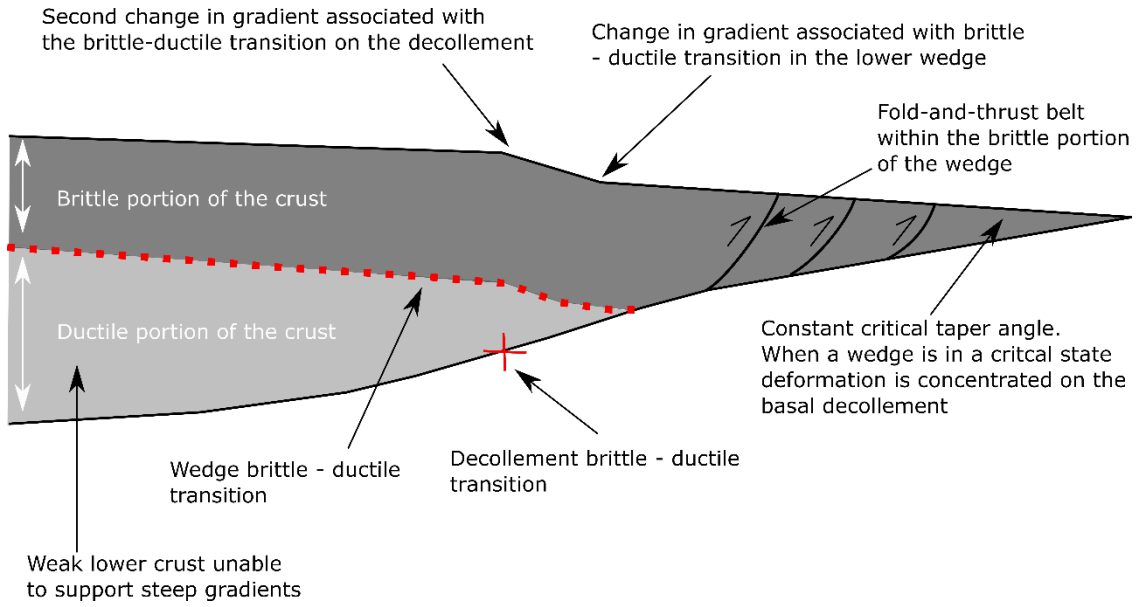

Figure 1.2: Schematic diagram to demonstrate the link between the regional slope in a critical Coulomb wedge and the brittle-ductile transition of the basal decollement and lower wedge. Image is an interpretation of the model presented in Williams et al.(1994).

1.2.2 The gravitational potential energy (G.P.E.) hypothesis

It can be shown, via the principle that slip occurs on fault paths that involve the least mechanical work, that lateral expansion of continental plateaux occurs primarily due to a need to minimise the increase in G.P.E associated with convergence (Masek & Duncan 1998; Molnar & Lyon-Caen 1988). As a mountain range increases in height, the energy required for a small amount of crustal thickening is greater than that provided by the driving force of the plates (Figure 1.3). Therefore, the mean height of the plateau and the thickness of the crust should reach a limiting value dependent on the driving force on the system and the strength of the crust (Molnar & Lyon-Caen 1988). If convergence is energetically inhibited in this way, then thrusting must also be inhibited.

Observations from the Tibetan Plateau and its surrounding fold-and-thrust belts, where strain is concentrated round the plateau edges, is consistent with a 'thin skinned' model where plateau elevation is limited by G.P.E. The 'thin skin' assumption pertains to a situation where the stresses which act upon the top and the base of the lithosphere are negligible and not included (England & Houseman 1988). A strong correlation between models and studied orogenic belts means there is good evidence that the latter are controlled, on a crustal scale, by minimum work processes.

It could be argued that the presence of normal faulting at the highest elevations in the southern Tibetan Plateau (Elliott et al. 2010) is inconsistent with the idea of a G.P.E limited elevation (Molnar & Lyon-Caen 1988). However, the presence of such faulting could be explained by other mechanisms that would not be inconsistent with a minimum work model. These include association with strike-slip movement, bookshelf faulting (Tapponnier et al. 2001) or shear tractions made by the northward movement of the Indian Shield beneath the plateau (Styron et al. 2015).

In addition, delamination of the lower proportion of the continental lithosphere could have elevated the plateau to a height that is no longer in equilibrium (England & Houseman 1988). Figure 1.4 shows an example where the buoyancy conditions have been perturbed, the

vertical stress in the interior of plateau is greater than the horizontal stress and normal faulting and thrust faulting can occur simultaneously in the plateau and fold-and-thrust belt respectively. Normal faulting is, therefore, not necessarily inconsistent with a minimum work model should an external influence have perturbed the system.

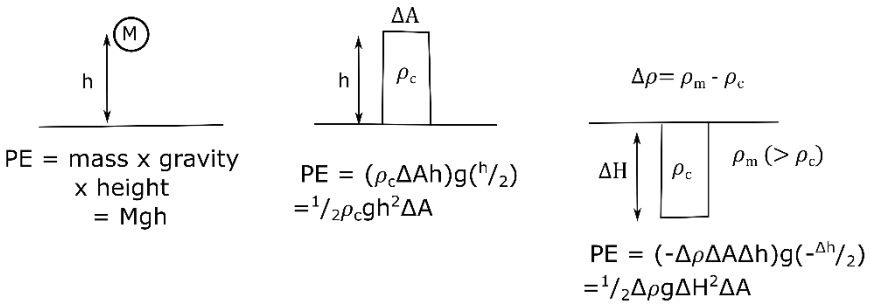

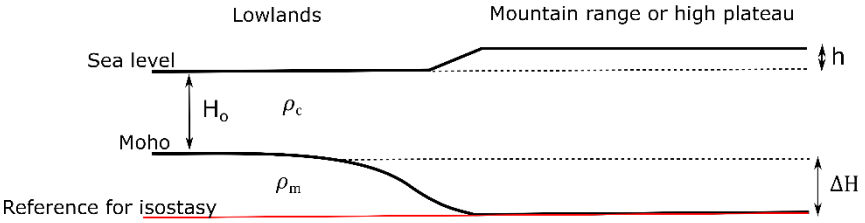

Assuming isostasy then: $H_o\rho_c + \Delta H\rho_m = (H_o + h + \Delta H)\rho_c$

$H_o\rho_c + \Delta H\rho_m = H_o\rho_c + h\rho_c + \Delta H\rho_c$

$\Delta H\rho_m - \Delta H\rho_c = h\rho_c$

$\Delta H(\rho_m - \rho_c) = h\rho_c$

Taking the Moho as the reference for PE:

$PE_{A(Lowlands)} = {}^1/_2 \rho_c g H_o^2$

$PE_{A(Mountains)} = {}^1/_2 \rho_c g(H_o + h)^2 + {}^1/_2 \Delta\rho g \Delta H^2$

$PE_{A(Mountains)} - PE_{A(Lowlands)} = \rho_c gh(^h/_2 + H_o + {}^{\Delta H}/_2)$

Therefore the averaged PE within the mountain range/plateau is greater than that within the surrounding lowlands.

Figure 1.3: Schematic of the G.P.E. for various situations taken from Molnar & Lyon-Caen's (1988) paper. Top figure displays the potential energy referenced to zero potential energy where ΔA represents the cross sectional area, ρ_m is the mantle density, ρ_c is the crustal density and g is the gravitational acceleration. The lower diagram represents the difference in potential energy per unit area between areas of plateau which contain deep crustal roots and lowland areas. Potential energy is calculated with reference to the Moho. The potential energy of a column depends on the reference depth but as long as isostasy applies the difference in potential energy per unit area is independent (Molnar & Lyon-Caen 1988).

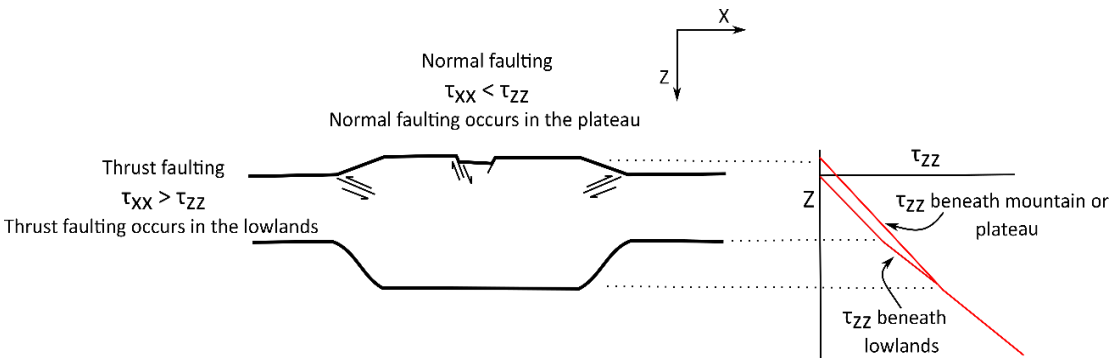

Figure 1.4: Schematic diagram to show the spatial relationship of thrust and normal faulting on the flanks of mountain ranges and beneath their high plateaux. Stresses applied to the base of the lithosphere are negligible so that the assumption that the horizontal stress (τ_{xx}) is constant and can be generalised to be independent of the horizontal position x holds. The vertical stress at any one point is dependent on elevation. On the right τ_{zz} is plotted as a function of depth beneath mountains/plateaux and beneath lowlands. At all depths τ_{zz} plateau ≥ τ_{zz} lowlands. Therefore, due to the constant nature of τ_{xx} should τ_{xx} be less than τ_{zz} in the plateau but greater than τ_{zz} in the lowlands and flanks of the range then the occurrence of normal faulting in the plateau and thrust faulting in the flanks and lowlands can be explained (Molnar & Lyon-Caen 1988).

Modelling by Masek & Duncan (1998) to assess the proposition that convergence is controlled by work minimisation predicted that faults initially choose short, direct routes to the surface in order to minimise the path length. With evolution of the plateau, and hence an increase in topography, faults tend to favour longer paths which avoid excessive topographic uplifting. A migration of thrust faults away from areas of increased G.P.E. is consistent with such models.

However, Molnar & Lyon-Caen's (1988) study neglected to consider the frictional work associated with deformation and the evolution of fault systems throughout a mountain range. When strain weakening and the associated reduced friction are included within Masek & Duncan's (1998) analysis, the models predict paths that remain stable even when far from gravitationally optimal. Therefore, within the context of a seismological limit this model still contains areas of uncertainty. Most obvious is the tendency of plateaux to continue to rise after the loss of large magnitude earthquakes (for example M ≥ 5 thrust earthquakes are rare above 3500 m in the Himalayas and Tibetan Plateau, far below the 5000 m average elevation of the plateau interior).

1.2.3 The thickening ductile interlayer hypothesis

The following hypothesis is a new unpublished idea generated in conjunction with this research project by Dr N. De Paola and is explored alongside more conventional theories as a novel perspective on the seismicity problem.

The general structure of fold-and-thrust belts tends to comprise sediments overlying a stronger crystalline basement. Sedimentary rocks are weaker than crystalline basement and hence undergo the transition from brittle to ductile behaviour at lower temperature-pressure conditions. A simplified structural model of fold-and-thrust belts can be taken to consist of a brittle basement overlain by ductile and then brittle sediments (Figure 1.5). Ductile behaviour in the form of cataclastic/microbrittle granular flow is predominantly a pressure (depth) dependent process (Paterson & Wong 2005). With increased convergence a thickened sedimentary layer develops and, therefore, it can be expected that the thickness of the ductile portion of the sedimentary layer will increase (Figure 1.5).

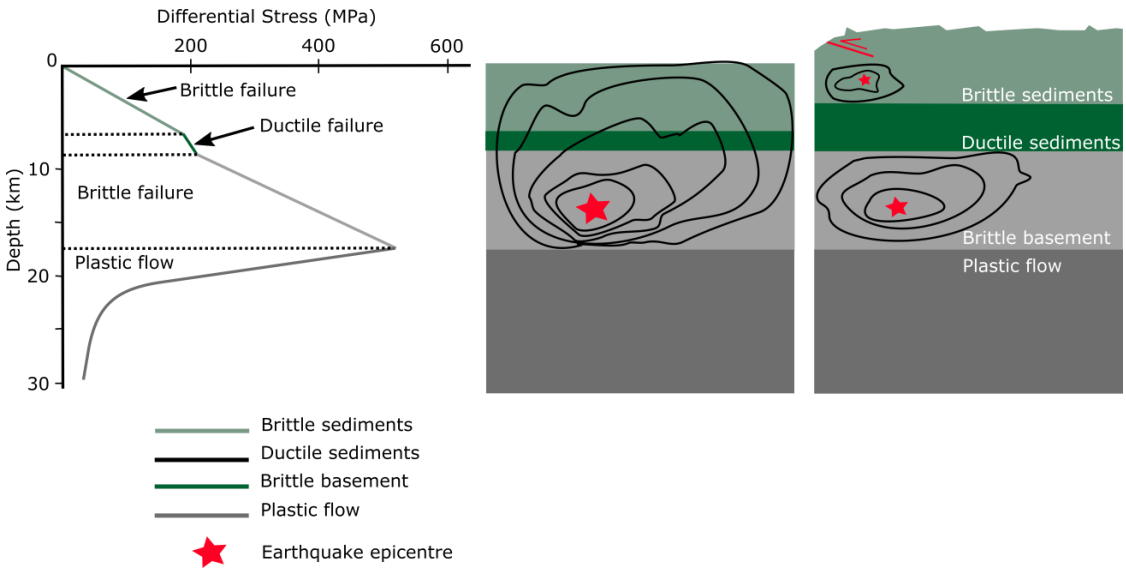

Figure 1.5: Schematic showing the effects of a thickened ductile interlayer within the sediments in a fold-and-thrust belt. Image on the left shows a depth vs differential stress graph for the crust (Paola pers. comm.).

Tectonic earthquakes can nucleate anywhere within the seismogenic layer but in almost all cases large earthquake nucleate near its base (Das & Scholz 1983). In this model it would be assumed that the majority of larger earthquakes nucleate within the basement rock. Such a thickened ductile layer is then suggested to inhibit the propagation of earthquakes initiating in the brittle basement. An earthquake's magnitude is proportional to the slip area which, in turn, can be assumed to be proportional to the length of fault that slips (Das & Scholz 1983). Assuming the thickened ductile layer inhibits the propagation (and therefore the rupture length) of a fault, it will also inhibit the maximum magnitude of the associated earthquake. This allows for shortening to occur across the range, via smaller earthquakes in the basement and the overriding brittle sediments, while large thrust earthquakes are inhibited.

This model fits well when considering the propagation of most faults, however, horizontal or low-angle faults, in theory, could propagate large distance, thus increasing the slip-area, without intersecting the ductile interlayer. This type of low-angle rupture rarely occurs and has only been observed with surface intercepting earthquakes, like that of the 2004 Mw 9.3 Sumatra earthquake and major inter-plate strike-slip faults. Both very different scenarios to the fold-and-thrust belt geometries examined within this study. Furthermore, low-angle fault geometries, due to dynamic interferences with the fault edges, result in a long, narrow rupture patch (Day, 1982; Nielsen et al., 2000). As such, the increase in area, linked with magnitude, is smaller with each incremental increase in length than with a standard fault geometry. As such, although theoretically large magnitude earthquakes can be caused by long, low-angle faults, within the context of this report it is not considered.

1.3 Project aims

Within the context set out above, the specific research questions addressed in this study are:

1. What is the relationship between earthquakes and topography and are the abrupt seismicity cut-offs previously presented by Allen et al. (pers. comm.) and Nissen et al. (2011) an accurate representation of this relationship?

2. Is the relationship between elevation and thrust earthquakes consistent throughout different fold-and-thrust belts and, therefore, can a generalised relationship be described?

3. Which, if any, of the above models is the most reasonable explanation for the reduction in large thrust earthquakes at high elevations?

4. How are uplift and crust thickening maintained after large scale thrust earthquakes have ceased?

1.4 Project hypotheses

This project explores three hypotheses:

Hypothesis 1 - The critical Coulomb wedge hypothesis: fold-and–thrust belts deform via the critical Coulomb wedge model. This model indicates that shear stresses for thrust faulting are more favourable at the toe of the wedge than within the plateau (Dahlen 1990) and therefore thrusting is concentrated at lower elevations. In addition, ductile deformation within the lower crust beneath the plateau is unable to support the steep gradients associated with brittle deformation and hence the occurrence of large thrust earthquakes.

Hypothesis 2 - The gravitational potential energy / minimum work hypothesis: as a mountain range increases in height, the energy required for small amounts of crustal thickening becomes greater than that provided by the driving force of the plates. The height of the plateau should, as a result, reach a limiting value where active thrusting ceases. In summary, the system dynamics are explained from the conservation of energy (Molnar & Lyon-Caen 1988).

Hypothesis 3 – The thickening ductile interlayer hypothesis: an increase in height, and therefore in lithostatic load, creates a thicker zone of distributed deformation within the sedimentary layer. This 'ductile interlayer' could potentially suppress the ability of large earthquakes, originating in the brittle basement, to propagate through the entire brittle crust, while still allowing smaller earthquakes to continue to develop in the basement and brittle portion of the overriding sediments.

In the following chapters these hypothesis are assessed as explanations for the reduction of large magnitude earthquakes at high elevation.

A reduction in large magnitude thrust earthquakes, as a pure result of the critical Coulomb wedge hypothesis, is predicted here to be associated with a change in deformation

mechanism, from brittle to ductile, first on the basal decollement and secondly within the lower wedge. A change in deformation mechanism will affect the critical taper angle and, therefore, the topographic slope (Section 1.2.1). Swath profiles are constructed to identify major changes in topographic slope across various localities (Chapter 3) and compared to the cut-off elevation for $M \geq 5$ earthquakes, identified in Chapter 2.

Alternatively, earthquakes of $M \geq 5$ are predicted to cease as a result of the work against G.P.E exceeding the driving force of the convergence (The gravitational potential energy / minimum work hypothesis). All M 5 earthquakes should cut-off at the same elevation. This hypothesis is tested in Chapter 2 by correlating earthquake magnitudes and elevation across various fold-and-thrust belts.

The 'thickening ductile interlayer hypothesis' is examined by using experimental analogues to investigate the $M \geq 5$ earthquake inhibiting influence of a ductile layer on a propagating fault. Triaxial experiments containing stacked cores will examine the nature of fault reactivation in a brittle medium and its propagation into a ductile one.

1.5 Project outline

This project addresses the relationship between elevation and M ≥ 5 earthquakes via a number of research techniques which operate on a range of scales. This aims to address the question via a multi-disciplinary approach. First, the proposed relationship between earthquake magnitude and elevation is quantitatively investigated. Specifically; the relationship in a small sub-sector, transecting the deformation front[1], is first examined. The regional topography is then examined via swath profiles and a plateau edge is calculated. This data is then compared to the identified relationship between M ≥ 5 earthquakes and elevation. These two approaches address the critical Coulomb wedge hypothesis and the gravitational potential energy (G.P.E.) hypothesis. Finally, experimental data is evaluated to identify how a brittle fault propagates into a ductile medium in an attempt to test Hypothesis 3.

Analysis was conducted on four well-developed active fold-and-thrust belts; the Himalayas, the Zagros, the Qilian Shan and the Longmen Shan (Figure 1.6). Localities were chosen based on the quantity of earthquake data available for each and the availability of adequate background information to aid analysis of the data. In addition, it had previously been suggested that earthquakes within these areas were limited at high elevations.

Within each section the individual contribution of the data is discussed in the context of

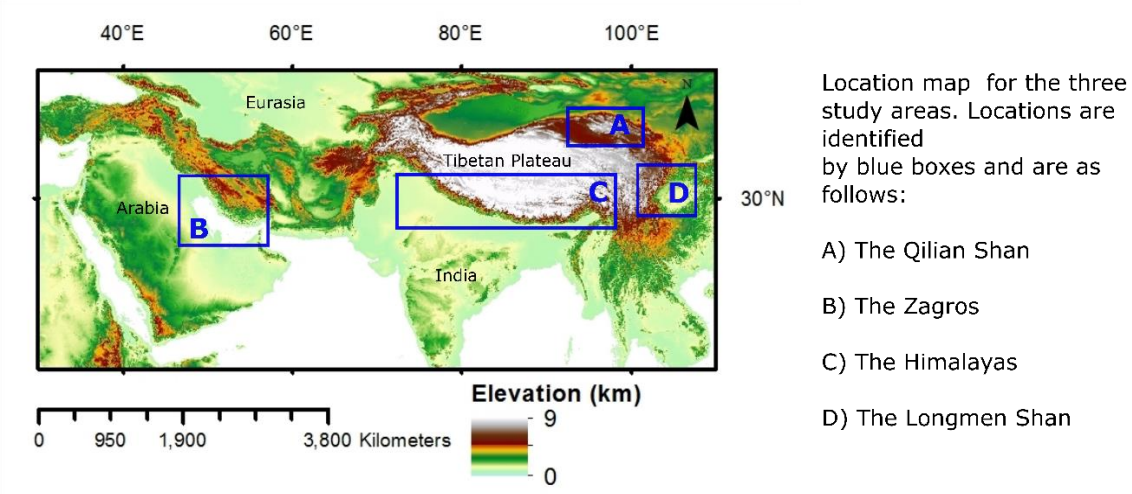

Figure 1.6: Location map for the study areas. Locations are identified by the blue boxes.

[1] The deformation front is defined as the limit of discernible deformation related to the fold-and-thrust belt, closest to the foreland.

the main research questions. In addition, areas of future work specific to each research avenue are discussed briefly in each chapter. The results from each section are then drawn together in an overview of the project, with further avenues of future work for the project as a whole being put forward.

Chapter 2

Identifying the relationship between thrust magnitude and elevation

2. Identifying the relationship between thrust magnitude and elevation

Before addressing why the previously suggested cut-off of M ≥ 5 earthquakes with elevation is observed, it is first necessary to verify that such a relationship exists within the chosen dataset. Specifically of interest is whether the empirical relationship observed in the Zagros by Nissen et al. (2011), and shown in Figure 2.1, can be quantitatively described. This study of high elevation thrust earthquakes, therefore, begins with an analysis of the relationship between thrust magnitude and elevation. Starting with the Zagros, the previously suggested (Nissen et al. 2011) elevation cut-off of M ≥ 5 earthquakes at 1250 m is examined. The same analysis is then applied to the fold-and-thrust belts at the northern (Qilian Shan) and southern (Himalayas) margins of the Tibetan Plateau. This analysis was not undertaken in the Longmen Shan for reasons explained in Section 3.3.4.

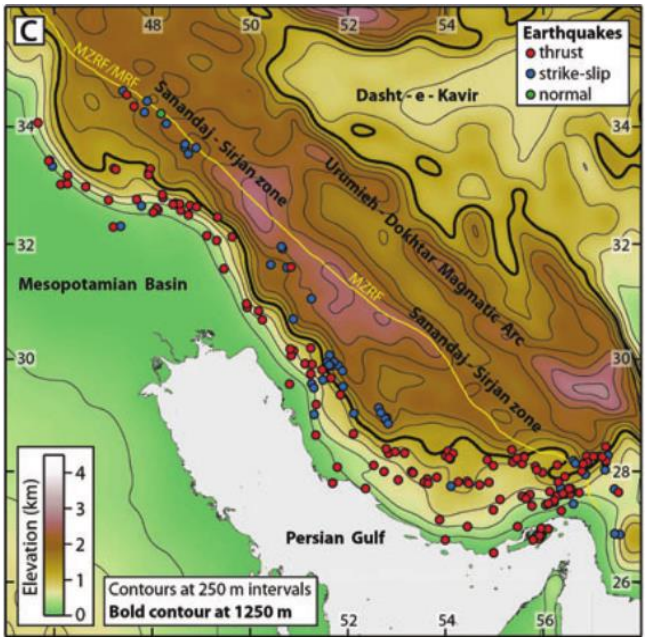

Figure 2.1: Identified seismic cut-off in the Zagros. Topography has been smoothed to 50 km using a Gaussian filter. Area has been contoured at 250 m intervals. The 1250 m contour can be seen in black (Nissen et al. 2011).

2.1 Methods

2.1.1 Earthquake data

The primary source for data is the National Earthquake Information Centre (NEIC) catalogue which extends back to the 1970s and collects data through the 'operation of modern digital national and global seismograph networks' (Earthquake.usgs.gov, 2016). Specifically, information was extracted from the Advanced National Seismic System (ANSS) Comprehensive Catalog (ComCat) within the NEIC. The magnitudes associated with the earthquakes are the best estimates made by the United States Geological Survey (USGS) at the time the earthquake was recorded, without any later modification. Because smaller earthquakes are hard to detect, events with $M < 4$ were discarded. Failing to do so would lead to an underestimation, and thus a misrepresentation of the number of smaller events in the catalogue. Focal mechanisms are not documented within the NEIC catalogue and, therefore, information on the type of earthquakes (strike-slip, thrust or normal) is unknown. However, moment–tensor solutions from the Global Centroid Moment Tensor (CMT) catalogue are forwarded to the NEIC catalogue (Ekström et al. 2012). Therefore, in some cases, it is possible to infer the associated focal mechanism by cross-referencing between the two databases.

Earthquakes that were identified in both catalogues were plotted using their NEIC coordinates, but highlighted separately from the main NEIC dataset as being known thrust events. Earthquakes within the CMT which did not match any events within the NEIC were added separately. Additionally, data were sourced from academic papers which also included focal mechanisms (Sloan et al. 2011; Talebian & Jackson 2004). Earthquakes without focal mechanisms that were located near ($\leq$ 50 km) known normal and strike-slip faults were removed from the dataset on the assumption there was a significant chance they were associated with these faults and were, therefore, not thrusts.

The locations of the earthquakes were extracted from the catalogues. In the NEIC catalogue this referred to the location of the earthquake epicentre. The earthquake coordinates were plotted on a topographic map using ArcGIS and elevations associated with each

earthquake location were extracted accordingly. The raw data were used to create graphs of elevation above mean sea level over a range of areas and therefore dataset sizes.

Prior to extracting the elevations, the topography was smoothed to reduce the elevation inaccuracies associated with mis-located epicentres. Epicentres within the earthquake catalogues USGS PDE and EHB have a mis-location error of, on average, 10 km which can in cases be up to 20 km (Nissen et al. 2011). The first publication of the CMT catalogue also identified errors of several tens of kilometres within the epicentre coordinates, and additionally errors of similar magnitudes for the hypocentral depth (Dziewonski et al. 1981). This analysis assumes similar epicentre mis-locations within the data and, as a result, the elevations are smoothed over radii of 10 km and 20 km. No appreciable difference appeared in the graphs of elevation vs. earthquake magnitude for smoothed radii of 10 km or 20 km for the Zagros and the Qilian Shan. However, in the Himalayas, potentially as a result of a more varied topography, a significant difference could be identified between the graphs using the two smoothing areas. Therefore, analysis was undertaken on graphs smoothed for 10 km in the Zagros and the Qilian Shan but 20 km in the Himalayas.

In a further attempt to remove any strike-slip and normal earthquakes from the dataset, smaller localities ('sub-sectors') within each of the locations, situated away from known major strike-slip and normal faults, were studied (Table 2.1). These sub-sectors can be seen in Figure 2.2. This assumes that a sub-sector of the fold-and-thrust belt perpendicular to the deformation front is representative of the range.

Table 2.1: Coordinates for selected small sub-sectors in the Qilian Shan and the Zagros.

Location	Max. Latitude	Min. Latitude	Max. Longitude	Min. Longitude
Qilian Shan	38º13'51.6''	36º34'12''	97º12'21.6''	94º11'20.39''
Zagros	30º0'00''	26 º0'00''	56 º0'00''	53 º0'00''

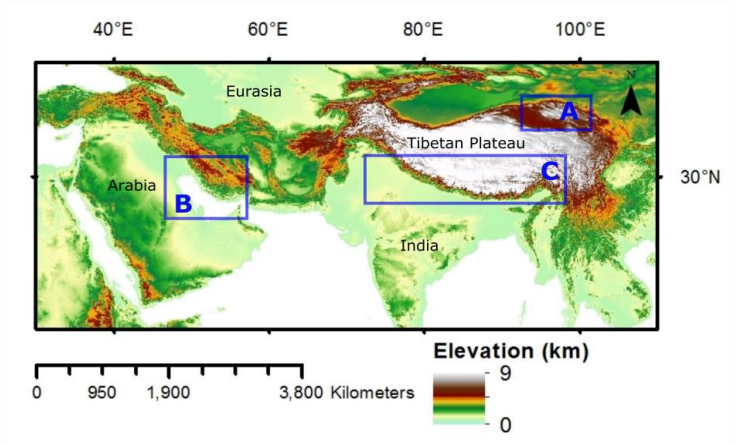

Location map for the three study areas. Locations are identified by blue boxes and are as follows:

A) The Qilian Shan

B) The Zagros

C) The Himalayas

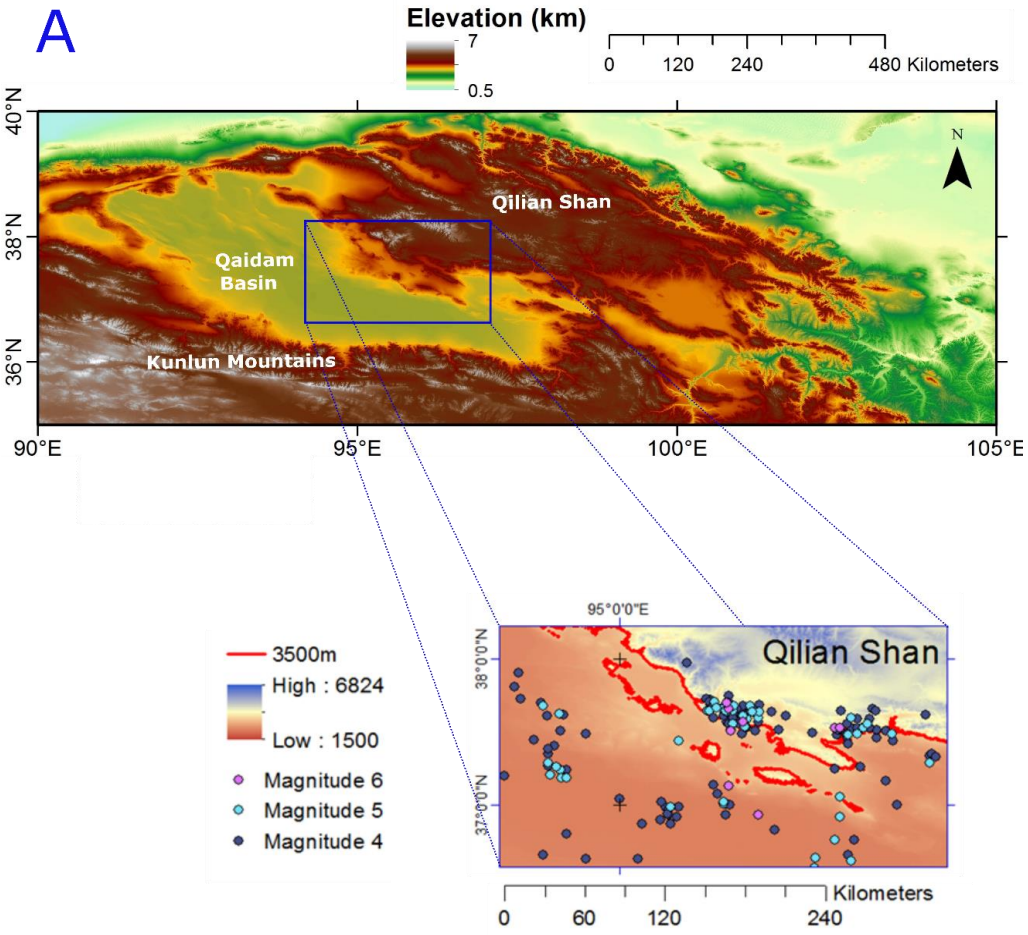

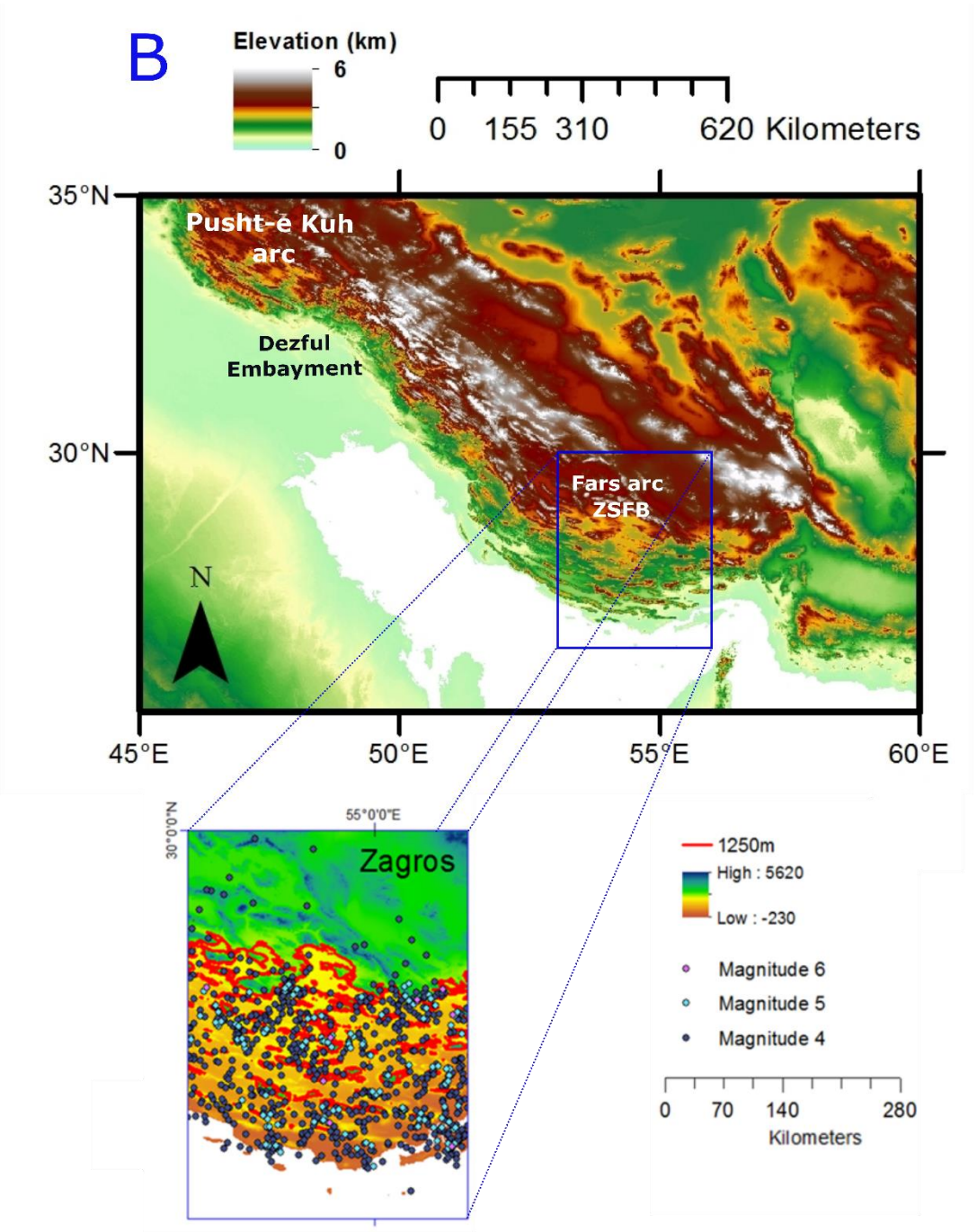

Figure 2 2: Location maps for the sub-sectors within a) the Qilian Shan and b) the Zagros. Locations were chosen away from known major strike-slip and normal faults. Earthquakes seen originate from all catalogues and are grouped by magnitude. ZSFB within 2.2b refers to the Zagros Simply Folded Belt.

Due to the complex nature of the Himalayan front, with the Karakorum strike-slip fault to the west and extensional structures in the east (Taylor & Yin 2009), there is not an area that can be confidently disassociated from normal faults and strike-slips, while at the same time presenting a large enough dataset for analysis. Data were instead extracted from six different areas along the Himalayan front (Table 2.2). These were then combined to form a representative dataset that was sufficiently large for analysis while being confidently disassociated from any strike-slip and extensional structures. The earthquake locations along the Himalayan front from the combined dataset are shown in Figure 2.3.

Table 2.2: Coordinates used for the six areas selected along the Himalayan front.

	Maximum Latitude	Minimum Latitude	Maximum Longitude	Minimum Longitude
Area 1	29°16'1.19"	25°57'50.39"	93 °53'2.4"	85 °29'31.2"
Area 2	29 °16'1.19"	27 °7'51.6"	85 °29'31.2"	83 °59'23.99"
Area 3	29 °46'26.4"	27 °27'39.59"	83 °24'21.6"	82 °1'40.8"
Area 4	33 °6'54"	28 °13'58.8"	77. °44'56.39"	77 °0'00"
Area 5	32 °29'13.2"	28 °13'58.8"	79 °4'33.59"	77 °44'56.39"
Area 6	30 °47'16.8"	28 °13'58.8"	80 °52'30"	79 °4'33.59"

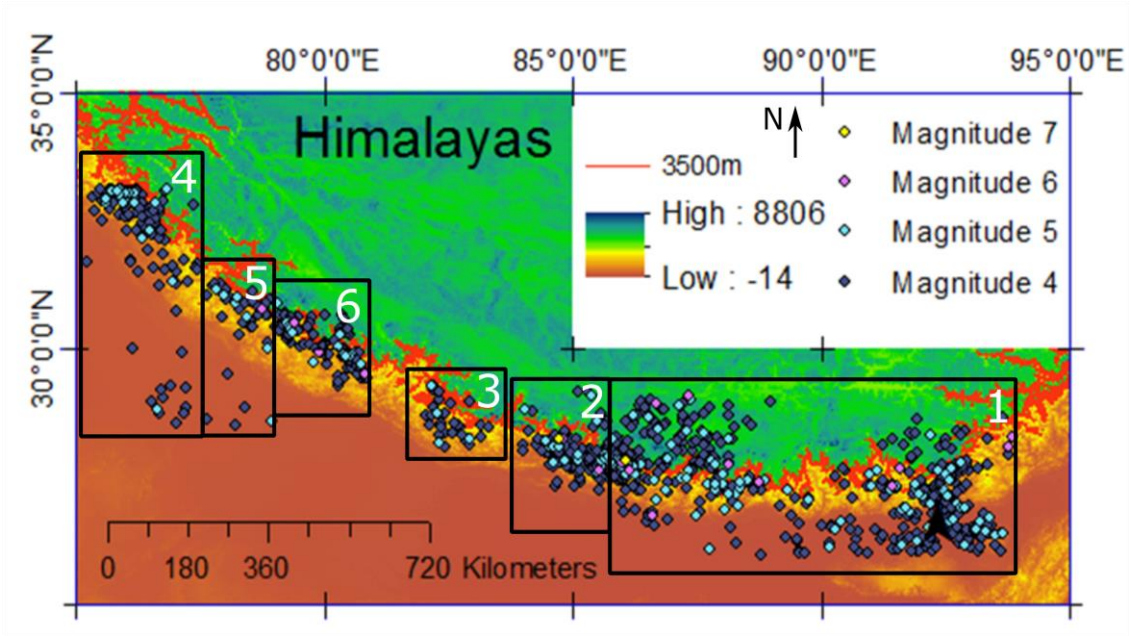

Figure 2.3: Earthquakes from within the six areas along the Himalayan front. Earthquakes seen originate from all catalogues and are grouped by magnitude.

2.1.2 Statistical methodology

The objective of the statistical analysis was to assess the nature of the relationship present and to quantify if the cut-off in seismicity was abrupt or gradual. The starting point was to define 'data envelopes'. In this case an 'envelope' refers to an upper proportion of earthquake magnitudes at each elevation thought to be representative of the overall relationship between magnitude and elevation.

The full dataset was allocated to bins set at either 250 m or 500 m steps in topographic elevation. Two envelopes of data were then extracted – corresponding to the top 10 % and top 20 % of the magnitude data points in each bin. This is illustrated in Figure 2.4 where the 10 % envelope comprises the green data points and the 20 % envelope comprises both the red and the green points. All other earthquakes were discarded and the 'top 10 %' and 'top 20 %' datasets were then re-plotted.

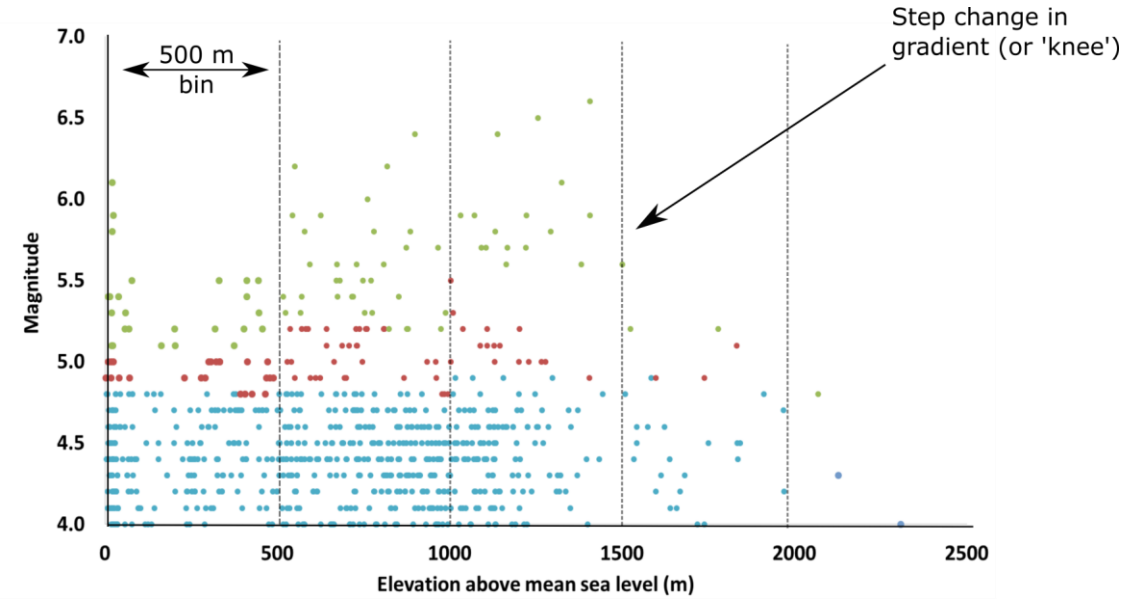

Figure 2.4: Example graph identifying the envelope and the division of the data into bins. Individual bins are separated via the vertical grey dotted lines. The 10 % envelope of the data is in green and the 20 % envelope additionally includes the red events. All other earthquake events are in blue.

The envelope bands were found to be non-linear, typically displaying a step change in gradient (or 'knee') around previously seen cut-offs in thrust earthquakes (Figure 2.4). Each of the datasets was plotted on two different graphs – one covering elevations up to the 'knee', and

the other elevations above this level. Linear regression was then applied to each of these graphs.

There is a compromise inherent in this approach. Using a greater percentage of each bin creates a more statistically reliable dataset but, at the same time reduces the degree to which the data represents the relationship between elevation and magnitude. Smaller percentages would be more representative of the relationship but were found to be more susceptible to the effects of outliers. It was for this reason that both 10 % and 20 % envelopes were considered in an effort to identify the clearest correlations.

2.1.3 Area-normalised graphs

When considering an energetic system, as done when examining the postulated lack of earthquakes of large magnitude using a G.P.E. approach, it is informative to consider the spatial distribution of earthquakes of different magnitude and their relative prevalence. Bar charts were produced showing data on the number of earthquakes at different elevations, and at different gradients. In order to analyse the effects of elevation accurately, the number of earthquakes within each elevation band were area-normalised. Areas from each band were obtained via a combination of ArcGIS and Global Mapper software. The relevant areas were isolated into individual 'shape layers' using the 'clipping' tool within ArcGIS. These layers were then exported and loaded into Global Mapper to obtain their areas. The following equation was employed to obtain the area-normalised values:

$$N_A = \frac{N}{A} \times 10^5 \qquad \text{Eq. 2.1}$$

Where N_A is the area-normalised number of earthquakes representing the number of earthquakes in the data set per km^2 occurring at the elevation in question, N is the observed number of earthquakes in the data set occurring at the elevation in question and A is the area of the particular elevation band in question measured in km^2. The 10^5 factor is required to make the values more manageable.

2.1.4 Gradient extractions

Gradients were created in ArcGIS for the smaller sub-sectors. Gradient values comprise a number in the range 0-1 with larger values indicating a steeper gradient: a gradient value of 1 would be a slope angle of 45^{o}. In order to maintain consistency with the extracted earthquake elevations, gradients were acquired from the smoothed topography. The numbers of earthquakes occurring at each gradient were area-normalised in a manner similar to that described in Section 2.1.3.

2.2 Results

2.2.1 Zagros, Iranian plateau

Graphs of earthquake magnitude against topographic elevation were plotted in order to investigate the quantitative relationship between the two variables. Data from the Zagros is shown in Figure 2.5 and presents a gradual decrease in earthquake magnitude with elevation. Analysis additionally showed some large magnitude earthquakes above the 1250 m seismic cut-off identified previously by Nissen et al. (2011). Even when known thrusts were relocated using their respective CMT co-ordinates (see Section 2.1.1) a few $M \geq 5$ events remained above the 1250 m contour. This could result from either the choice of smoothing factor or due to errors with the epicentre location.

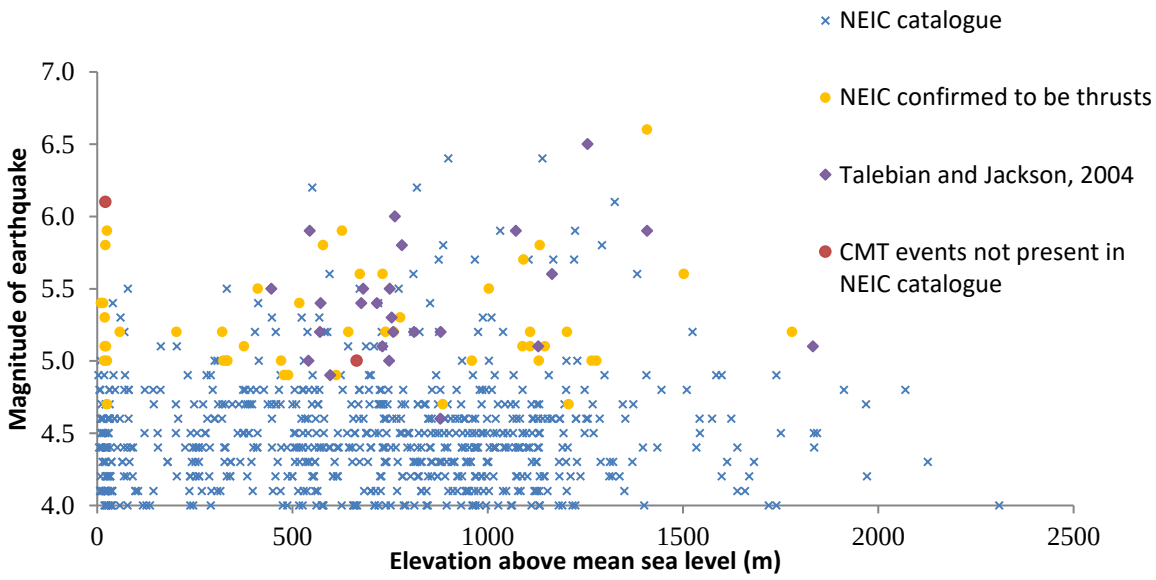

Figure 2.5: Graph showing the earthquake magnitude vs topographic elevation relationship for the small sub-sector in the Zagros (Figure 2.2b). Elevations are taken relative to mean sea level from a topography smoothed to 10 km. The majority of data was acquired from the NEIC catalogue. Events in the NEIC catalogue that were confirmed to be thrusts, via cross-coordination with the CMT catalogue, have been plotted via their NEIC coordinates and are labelled as 'NEIC confirmed to be thrusts'.

Simple regression analysis on the earthquake magnitude vs topographic elevation graph was undertaken for the top 10 % envelope of each 250 m bin. The regression analysis was separated into data above and below the 1250 m cut-off. For both graphs (Figure 2.6a & b) there was a linear fit but with an extremely low significance. For the dataset lower than

1250 m, all possible regression lines having significance levels > 95 % had a positive gradient (Figure 2.6a). This suggests that below the seismicity cut-off there is an overall increase in the maximum magnitude of earthquakes with elevation. This is contradictory to what might be expected considering the greater energy associated with large magnitude earthquakes and the increasing demands on the energy budget from G.P.E. with increasing elevation.

Large variations in the surface area corresponding to different elevations could result in a misrepresentation of the relationship between earthquake magnitude and topographic elevation. To rectify this, the number of earthquakes at each elevation was area-normalised (Figure 2.7). A lack of seismicity at higher elevations can be seen from the area-normalised data with a rapid decrease in the number of earthquakes at some point in the 1.0-1.5 km bin, consistent with the proposed 1250 m cut-off. This analysis suggests a more abrupt seismicity cut-off which in addition affects earthquakes with $M < 5$. Figure 2.8 presents evidence that the proportion of the largest earthquakes increases with elevation. For example, the number of $M = 6$ earthquakes increases from 1 % at 0.5-1.0 km to 3 % at 1.0-1.5 km. However, the percentage points increases are marginal and could merely be the result of outliers distorting a small dataset.

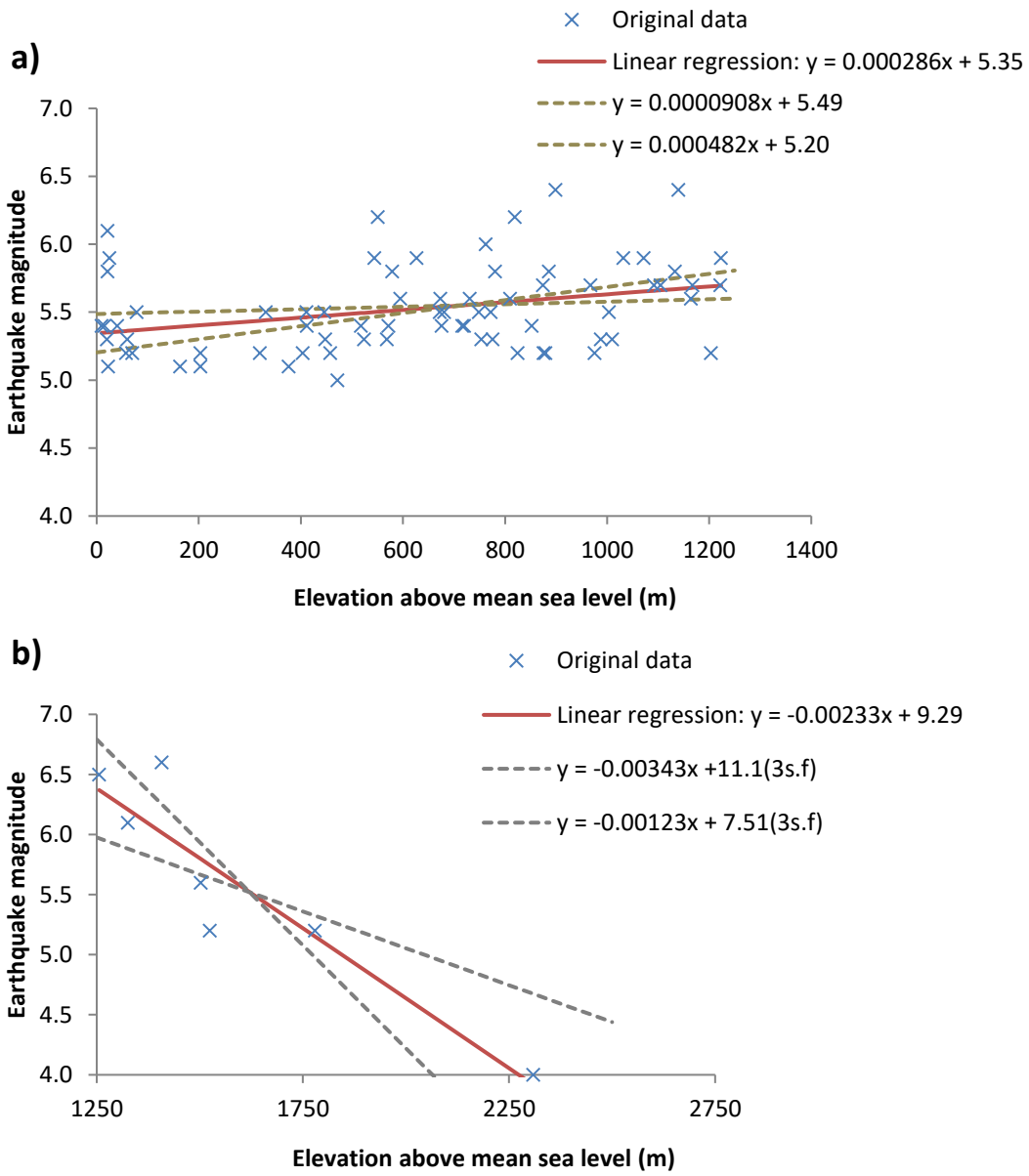

Figure 2.6: Linear regression plots for the Zagros sub-sector a) below, and b) above, the previously reported seismic cut-off. The significance value for (a) is 0.00469 and R^2 value is 0.0959. For (b) the significance value is 0.00283 and R^2 value is 0.827. The graph additionally shows the upper and lower bounds of all the linear regression lines that would remain within the 95 % significance level. Below 1250 m both the upper and the lower bound keep a positive relationship between elevation and earthquake magnitude. Analysis is conducted on the NEIC catalogue and does not include locations from the CMT catalogue. The bin width is 250 m and the envelope considers the top 10 % of the data.

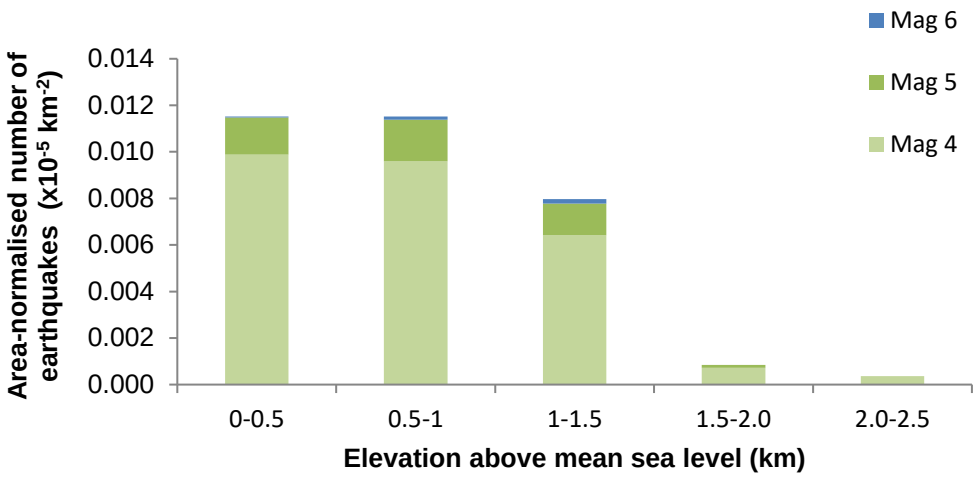

Figure 2.7: Area-normalised graph showing the relationship between topographic elevation and earthquake magnitude from the smaller sub-sector in the Zagros defined in Figure 2.2b.

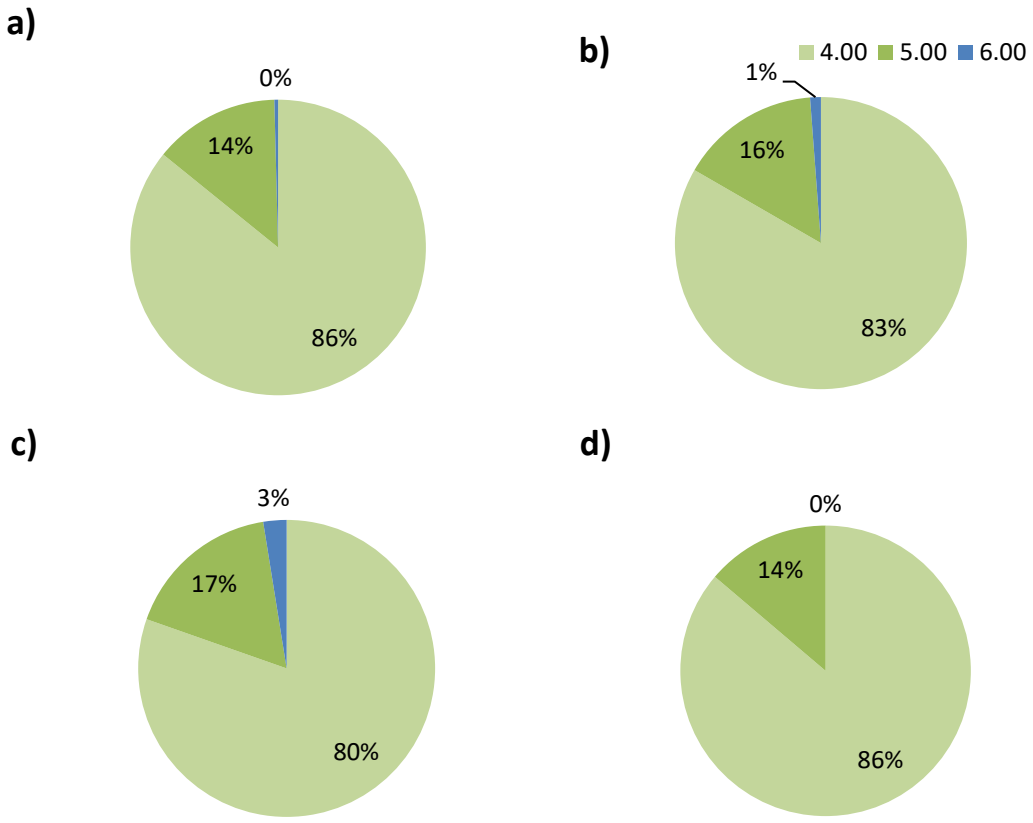

Figure 2.8: Pie charts representing the data in Figure 2.7. Each pie chart displays the break down in earthquake magnitude for a defined elevation band. The elevations are: a) 0-500m, b) 0-1000 m, c) 1000-1500 m and d) 1500-2000 m

2.2.2 Himalayas

A cut-off in M ≥ 5 earthquakes at 3500 m has previously been noted (Allen pers. comm.) to occur universally around the Tibetan Plateau (Figure 2.9). This has been proposed to link to Molnar & Lyon-Caen's (1988) minimum work theory. From Figure 2.10 an abrupt and complete cessation in the occurrence of thrust earthquakes within the CMT catalogue (red points) can be identified between 3000 m and 4000 m, consistent with these previous observations. However, Figure 2.10 also indicates that data from the less comprehensive NEIC catalogue shows earthquakes continuing to occur above this elevation with magnitudes of up to M = 5.5.

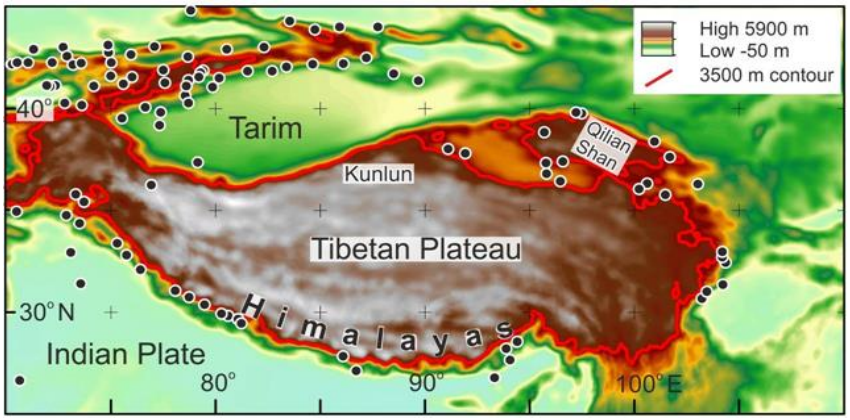

Figure 2.9: Previously identified cut-off in M ≥ 5 earthquakes in the fold-and-thrust belts surrounding the Tibetan plateau based on data taken from Sloan et al. (2011) and supplemented by the CMT catalogue. (Allen et al in prep)

The inaccurate depth measurements associated with the NEIC catalogue (see Section 2.1.1) mean one possible explanation for M ≥ 5 earthquakes above 3500 m is that some hypocentres may be located in the strong Indian Shield, rather than in the overriding plate. The under-thrusting of the Indian Shield has been previously associated with unusually large numbers of earthquakes at depths of 80-100 km within northwest Tibet (Craig et al. 2012). Therefore, the data presented in the NEIC, due to its lack of definitive depth measurements, cannot be confidently dissociated from the India Shield and, as such, used to assess the elevation associated with the seismicity cut-off. Hereinafter, the approximate cut-off in major thrust earthquakes is based on the CMT catalogue and thus considered to occur at 3500 m.

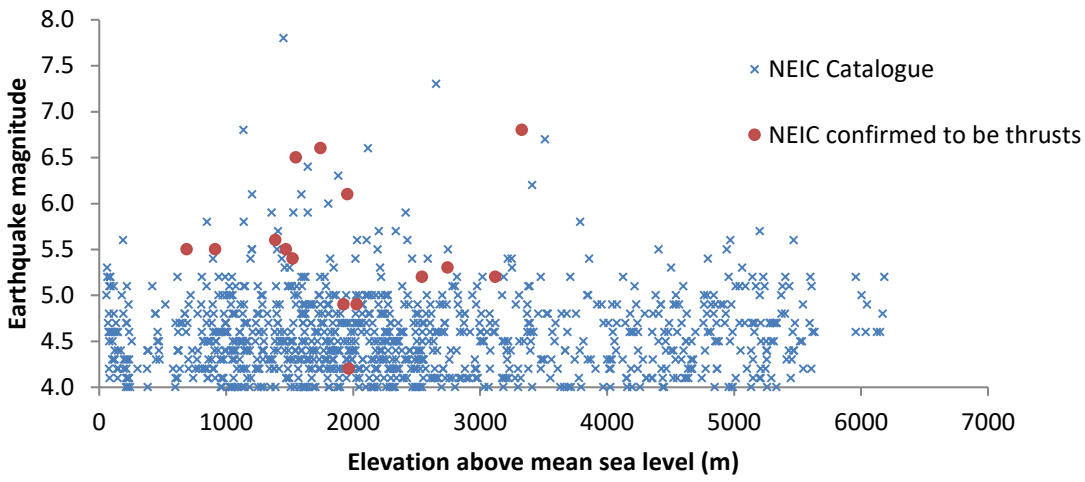

Figure 2.10: Graph showing the earthquake magnitude vs topographic elevation relationship for the Himalayas. Prior to extracting earthquake locations the topography was smoothed over a radius of 20 km. Events in the NEIC catalogue that were confirmed to be thrusts, via cross-coordination with the CMT catalogue, have been plotted via their NEIC coordinates and are labelled as 'NEIC confirmed to be thrusts'.

Linear regression analysis was again undertaken by dividing the data into two separate sets based on the predicted change in relationship at 3500 m. The data, both below (Figure 2.11a) and above (Figure 2.11b) the 3500 m cut-off, displayed a linear relationship with extremely low gradients. At the lower elevations the gradient of the linear fit was found to be slightly positive, whereas within the higher dataset it was negative (see the red lines in Figure 2.11). This being said, both sections could fit either positive or negative gradients to the data while remaining within the 95 % significance level. The grey dotted lines in Figure 2.11 demonstrate the range in possible regression lines that remain within this significance level. Despite having reasonably high significance levels the graphs have low R^2 values, which is not unexpected given their low gradients.

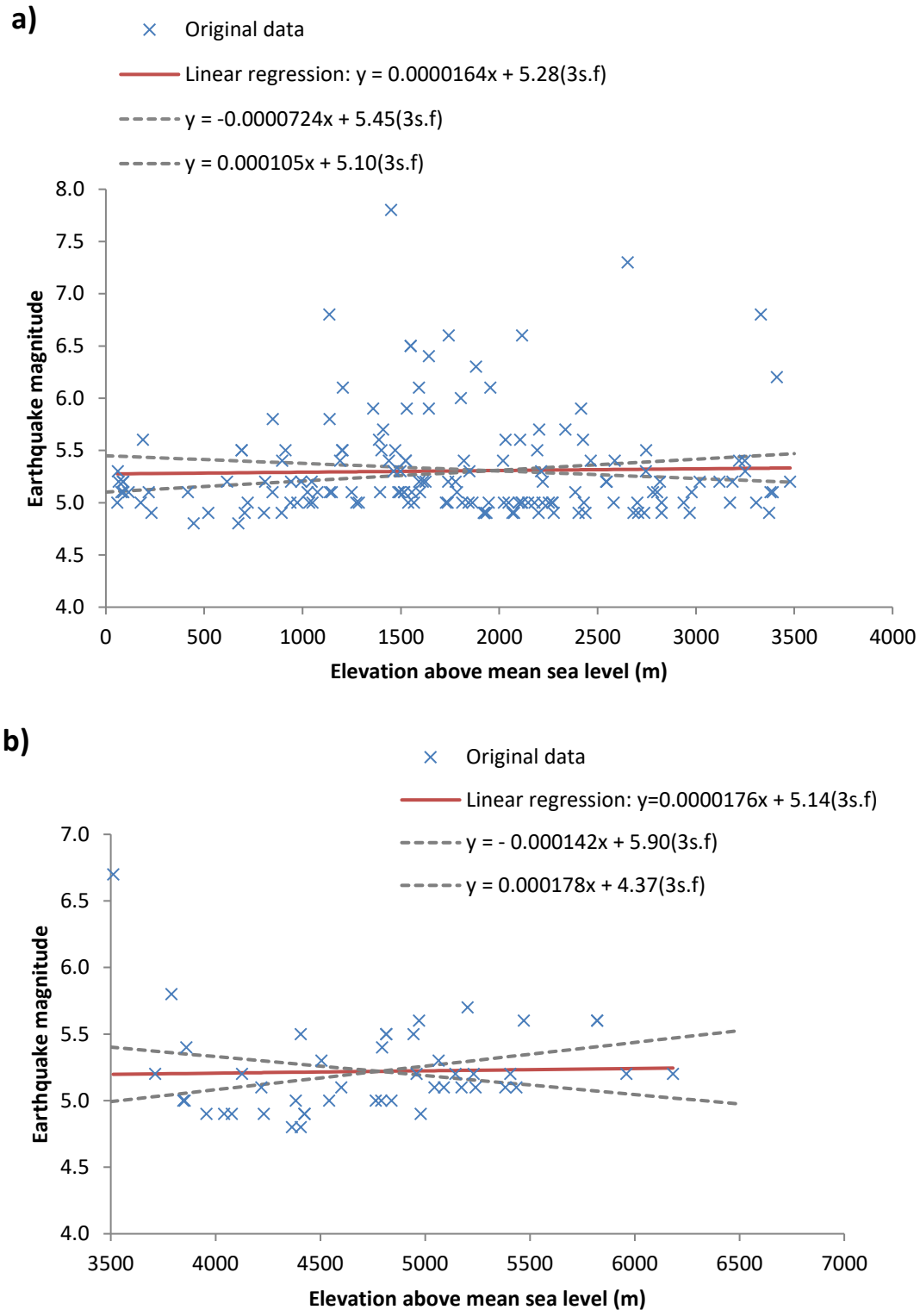

Figure 2.11: Linear regression plots for the Himalayas a) below, and b) above, the defined seismic cut-off. The significance value for (a) is 0.71592 and R^2 value is 0.00084. For (b) the significance value is 0.82548 and R^2 value is 0.00109. The bin with is 500 m and the envelope considers the top 20 % of the data. The graph additionally shows the upper and lower bounds of all the linear regression lines that would remain within the 95 % significance level. In both cases the gradient of the regression line can be seen to switch from positive to negative while remaining at 95 % significance.

It could be argued that the essentially zero gradient in both linear regression graphs might have resulted from a less representative data envelope. The analysis of the Zagros presented in Figure 2.5 used the upper 10 % of each bin while the graphs for the Himalayas in Figure 2.11 used the upper 20 %. However, the Himalayan graphs using 10 % showed a similar, but even less statistically significant relationship. Overall, such statistical analysis therefore does not present evidence for a linear relationship between elevation and earthquake magnitude in the Himalayas.

Due to the extent and complexity of the regions in the Himalayas, accurate extraction of the areas associated with each elevation band could not be undertaken. Therefore, for the Himalayas a full analysis of the relationship between elevation and earthquake magnitude was not possible.

2.2.3 Qilian Shan, Northern Tibetan Plateau

Earthquake magnitude was plotted against topographic elevation for the selected sub-sector in the Qilian Shan (Figure 2.12). The initial relationship shows a sudden cut-off of all earthquakes at approximately 4000 m, 500 m above the cut-off of $M \geq 5$ seen within the CMT catalogue in the Himalayas. Replotting the data from the CMT catalogue with their CMT locations, rather than their NEIC locations, reduces the elevations slightly but still shows earthquakes above the 3500 m contour. Therefore, the 3500 m cut-off in seismicity in the Himalayas, validated in the previous section, cannot be extrapolated to the entire Tibetan Plateau.

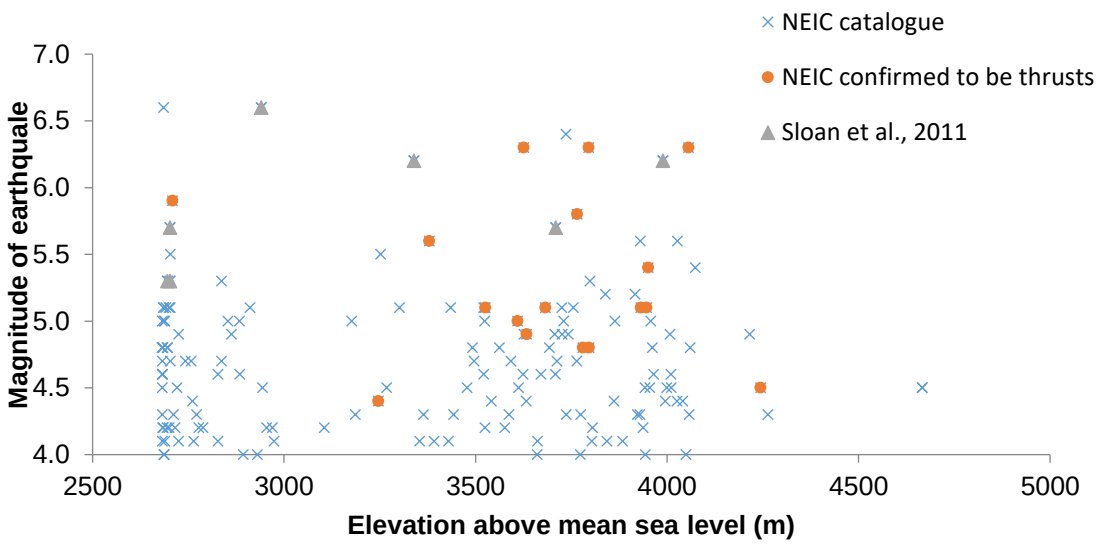

Figure 2.12: Graph showing the earthquake magnitude vs topographic elevation relationship for the small sub-sector in the Qilian Shan (Figure 2.2a). Elevations are taken in relation to mean elevation above sea level from a topography smoothed to 10 km. The majority of data was acquired from the NEIC catalogue. Events in the NEIC catalogue that were confirmed to be thrusts, via cross-coordination with the CMT catalogue, have been plotted via their NEIC coordinates and are labelled as 'NEIC confirmed to be thrusts'.

--

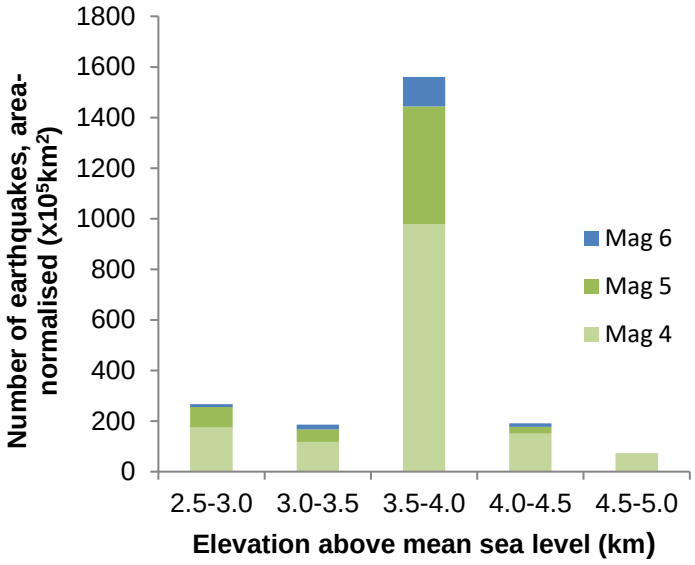

Figure 2.13: Area-normalised graph showing the relationship between topographic elevation and earthquake magnitude from the smaller sub-sector in the Qilian Shan defined in Figure 2.2a.

Linear regression analysis was undertaken for the Qilian Shan, but due to the smaller dataset the elevation vs. magnitude data were plotted on a single graph (rather than separate graphs below and above a cut-off). Again, due to the extremely small dataset the analysis of the envelope appeared to vary significantly with different bin widths and percentages of the data. All analyses showed that the gradient can be either positive or negative while remaining within the 95% significance level. Therefore, no clear evidence for any relationship was detected from this dataset. The full set of graphs and statistics are presented in Appendix A.

Figure 2.13 displays an area-normalised graph of elevation plotted against earthquake prevalence. Each bar has been subdivided for earthquake magnitude. There appears to be a significant concentration of seismicity within the elevation band 3500-4000 m. Initially, this was thought to represent a peak in association with the plateau edge, suggesting a relationship between slope gradient and seismicity. Looking at the break down in magnitude of each earthquake (Figure 2.14) it can be seen that the proportion of M = 6 earthquakes is again greatest within the 3500-4000 m band. The proportion of larger earthquakes ($M \geq 5$) appears overall to decrease once the putative seismicity cut-off at 4000 m is passed, but the proportion of M = 6 earthquakes remains the same. However, it should be noted that the area analysed is small and, therefore, may be affected by statistical outliers.

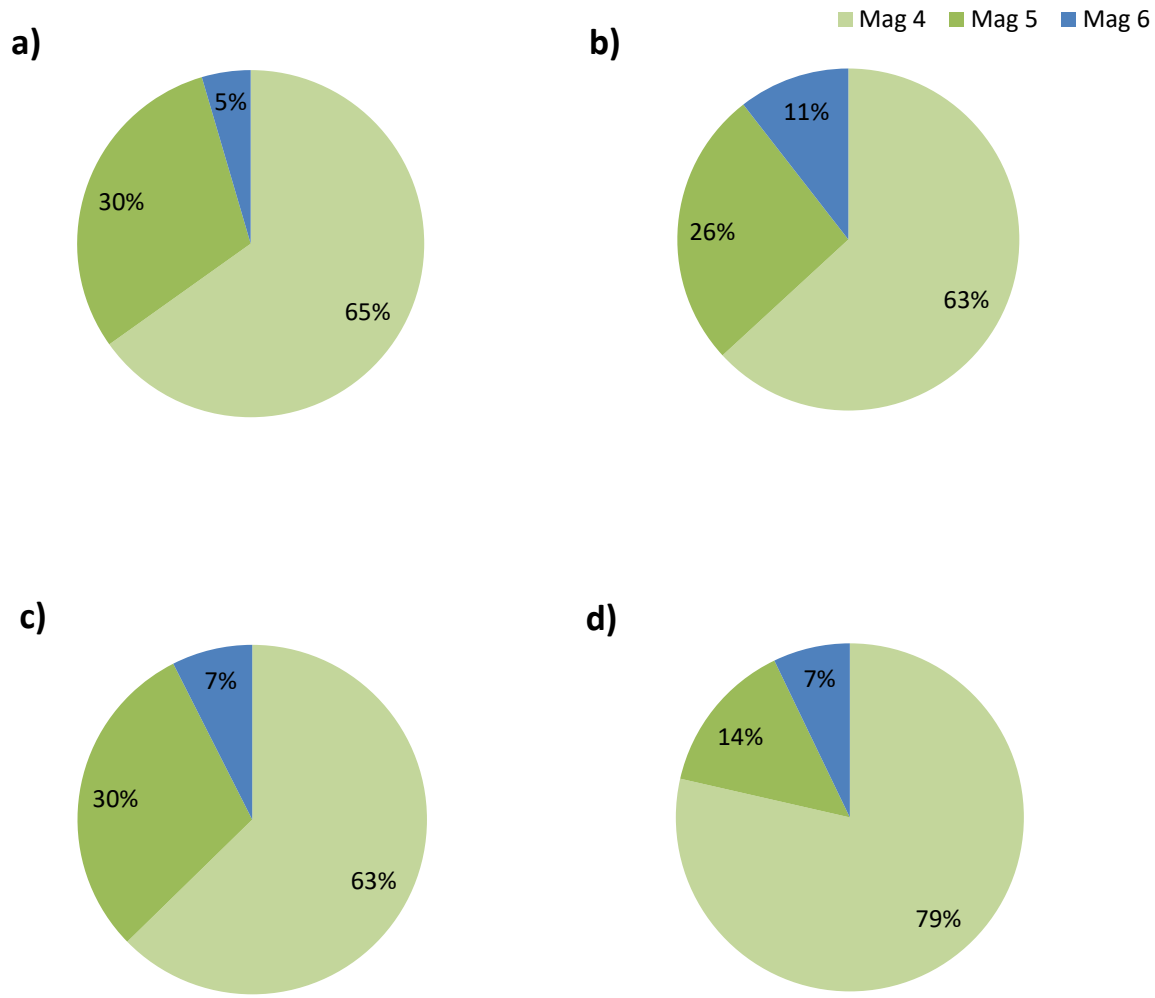

Figure 2.14: Pie chart representation of the data in Figure 2.13. Each pie chart displays the break down in earthquake magnitude for a defined elevation band. The elevations are a) 2.5-3.0 km, b) 3.0-3.5 km, c) 3.5-4.0 km and d) 4.0-4.5 km. At the highest elevation (4.5-5.0 km) there are only earthquakes of magnitude 4 and therefore that graph is not presented.

2.2.4 Aftershocks in the Qilian Shan

The observed spatial distribution of earthquakes presented two strong clusters situated at, or just above, the 3500 m contour (Figure 2.15). Generally, the clustering of earthquakes suggests that a proportion of the events are aftershocks triggered by preceding earthquakes due to mechanisms such as static or dynamic stress changes, fluid flow or after-slip (Gu et al. 2013). Should these clusters be the result of aftershocks, then the peak at 3500-4000 m could be accentuated as a result of dynamic stress transfer. Re-examination of the dates associated with earthquakes within the NEIC catalogue of the two clusters indicated that many of the focal mechanisms appeared to occur in association with a preceding large earthquake event. The full list of earthquake events can be seen within Appendix A. An attempt to extract these 'aftershocks' from clusters 1 and 2 was undertaken.

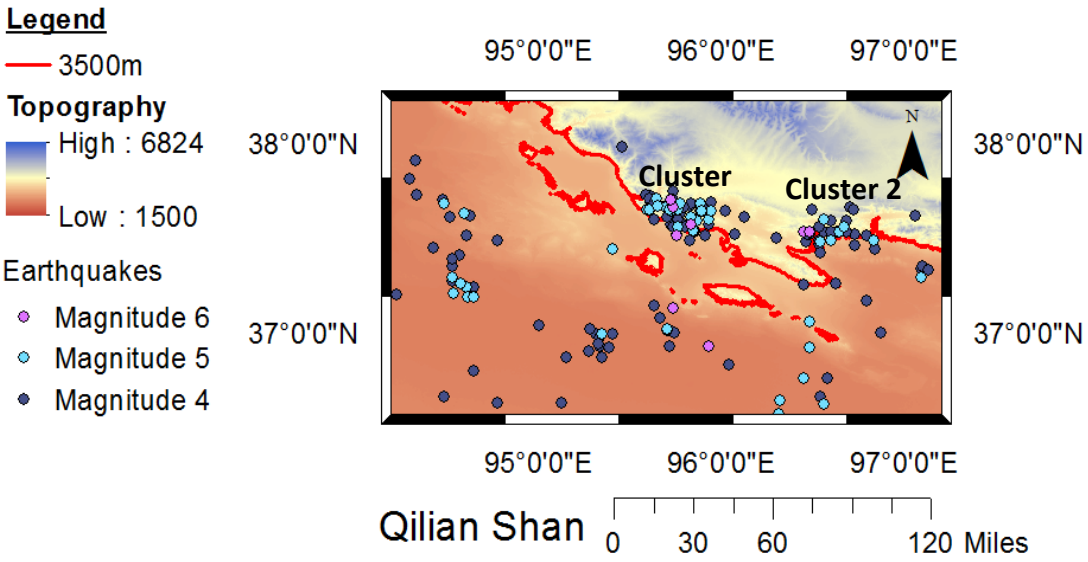

Figure 2.15: Qilian Shan showing the aftershock clusters.

Any earthquake, regardless of size, can trigger another earthquake. Currently there is no distinct difference in the relaxation mechanism for mainshock, foreshock and aftershock events. Identification of an aftershock relies on correctly identifying the triggering relationship (Gu et al. 2013). A detailed review of each earthquake to determine which constitutes an

aftershock is beyond the scope of this study. Therefore, the relationship is generalised and larger earthquakes are regarded as the 'mainshock' and smaller earthquakes as the 'aftershock'. Some aftershock classification includes in the definition of an 'aftershock' those earthquakes which are indirectly triggered by the mainshock or are themselves triggered by an aftershock (Gu et al. 2013). For simplicity, only direct aftershocks are considered. First a number of scaling laws relating to aftershocks are reviewed in an attempt to identify a systematic way of excising aftershocks from the data.

Båth's law states that the difference in magnitude between a mainshock magnitude M_{ms} and its largest detected aftershock with magnitude M_{as}^{max} is expressed as given in Eq. 2.2:

$$\Delta M = M_{ms} - M_{as}^{max} \qquad \text{Eq. 2.2}$$

This ΔM is approximately a constant, independent of the mainshock magnitude, usually taken as 1.2 (Shcherbakov et al. 2004). From this it could be crudely established which earthquakes are too large to be considered aftershocks. If this is the case, then most of what were considered aftershocks (earthquakes occurring after $M \geq 5$ events) were in fact larger than would be predicted by Eq. 2.2. Due to the clear spatio-temporal clustering it can be concluded that within this analysis Båth's law is an inappropriate way to refine the data.

Omari's law (Eq. 2.3), which defines the relationship between time and the occurrence of aftershocks, is thought to be the simplest, and most accurate way to estimate earthquake interactions (Helmstetter & Sornette 2002):

$$\textit{Rate of Earthquakes triggered by a mainshock} = \frac{1}{t^p} \qquad \text{Eq. 2.3}$$
$$\textit{Where p is approximately equal to 1}$$

Omari's law (Eq. 2.3) can be used to assume that most aftershocks are triggered within hours or days of a mainshock.

Implementing an arbitrary rule to distinguish between aftershocks and mainshock introduces a degree of subjectivity (Gu et al. 2013). However, the constants particular to each earthquake system and the small datasets of the selected sub-sectors means that despite these

efforts there is still inadequate information to establish which earthquakes are aftershocks via an empirical law. Therefore, a systematic way to remove earthquakes considered to be aftershocks was implemented based on the assumption extracted from Omari's law that earthquakes are triggered within short time periods of the mainshock.

Graphs for the Qilian Shan were modified working under two assumptions. Firstly, every earthquake occurring on the same day as an $M \geq 5$ earthquake is an aftershock, and secondly, any earthquake occurring within a month of the mainshock earthquake is an aftershock. De-clustering schemes such as this, which are based on a sharp space-time aftershock window following a large earthquake, could be incorrect as a result of an inappropriate observation window. They are also at risk of missing long range triggering relationships. In addition, the spatio-temporal clustering indicates that the majority of earthquakes are likely to be affected by preceding ones (Gu et al. 2013). Considering the time and data constraints on this study this systematic approach into identifying aftershocks is nonetheless considered to be an acceptable way of estimating at least the lower bound of earthquake aftershocks.

Irrespective of eliminating earthquakes occurring on the same day, or earthquakes occurring within the same month (the latter of which removes 60 % of the earthquakes within the clusters), the peak of earthquakes at 3500-4000 m remains (Figure 2.16). Therefore, the peak present at 3500 m, which is the same as the seismicity cut-off in the Himalayas, is likely to be genuine rather than an artefact of aftershock clustering. In addition, the proportion of larger earthquakes increases with elevation until the identified 4000 m seismicity cut-off after which $M = 4$ events become prominent once more. This cluster does, however, seem to be located on a known thrust fault ridge, the Tergun Daba Shan (Chen et al. 2002). Therefore, the relationship shown may be a local, rather than regional one, and the correlation with this peak and the cut-off in the Himalayas merely a coincidence. Nevertheless, this analysis has demonstrated that aftershocks have minimal influence on the limiting effect that topographic elevation has on earthquake magnitude.

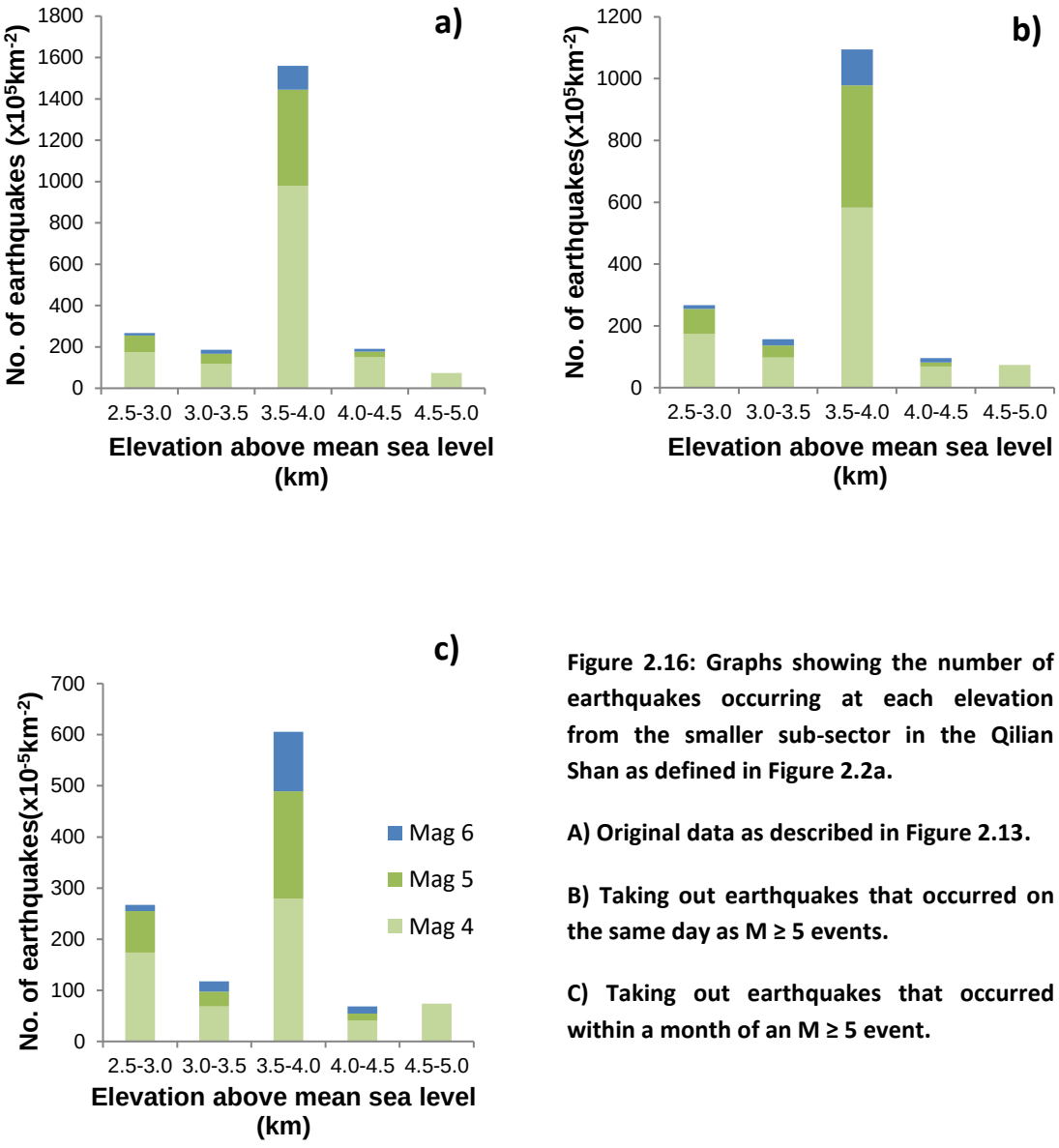

Figure 2.16: Graphs showing the number of earthquakes occurring at each elevation from the smaller sub-sector in the Qilian Shan as defined in Figure 2.2a.

A) Original data as described in Figure 2.13.

B) Taking out earthquakes that occurred on the same day as M ≥ 5 events.

C) Taking out earthquakes that occurred within a month of an M ≥ 5 event.

2.2.5 Earthquake magnitude and gradient

As a result of the initial analysis in Section 2.2.4, an investigation was undertaken into the effects of gradient on the number and magnitude of earthquakes that occur.

The Zagros demonstrated no relationship between gradient and earthquake concentration at shallower slopes but showed a significant increase in the number of earthquakes at the highest gradients (Figure 2.17). However, due to the small size of the sub-sector selected for analysis, the variation in gradient was found to be so minimal that it was picking up individual anticlines. The highest gradients were found to be associated with a significant anticline on the High Zagros Fault (Figure 2.18).

This result confirms that the anticlines with the steepest flanks are those that are most active. Therefore, this can be utilised from a natural hazard perspective as evidence that such steep flanks are statistically more likely to pose the highest seismic risk. However, the location errors of the epicentres within the original dataset, as well as the effect outliers would have on such a small area, does reduce the significance and utility of this graph.

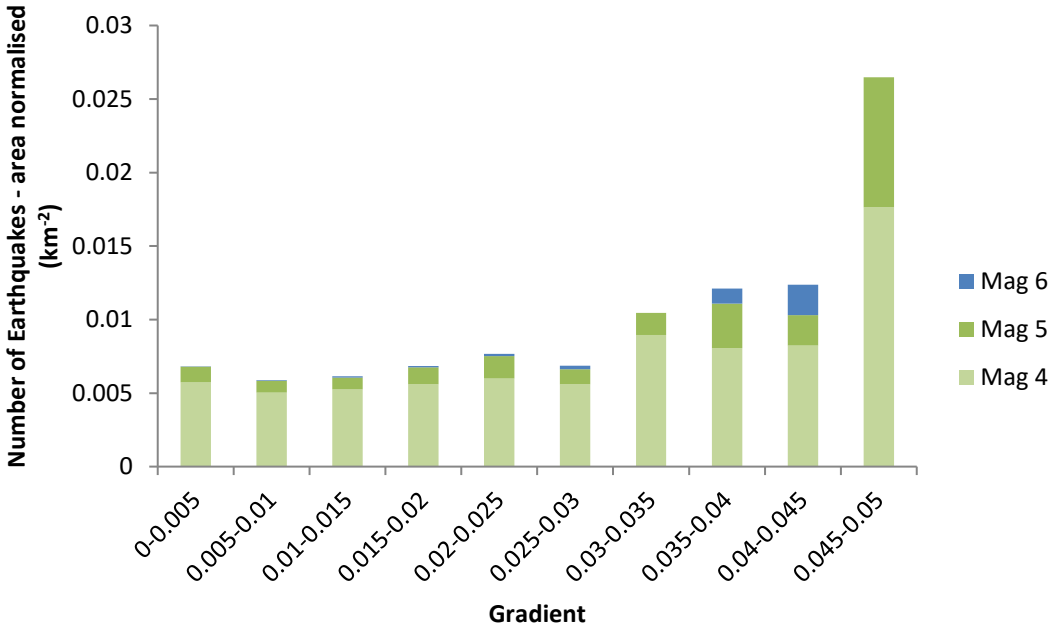

Figure 2.17: Area-normalised number of earthquakes vs gradient for the selected sub-sector of the Zagros as defined in Figure 2.2b.

In an attempt to identify a more regional effect of gradient the size of each gradient band was increased. Figure 2.19 displays this modified area-normalised graph. The small size of the sub-sector analysed in the Zagros still meant that the variation in gradients was minimal but this grouping at least no longer picked out variations within individual folds. This analysis (Figure 2.20) identified that the proportion of large magnitude earthquakes occurring at high gradients is greater. This then poses the question of which came first: are the gradients steep due to active faulting in the area or are the large earthquakes occurring due to the steepness of slope making the area more unstable.

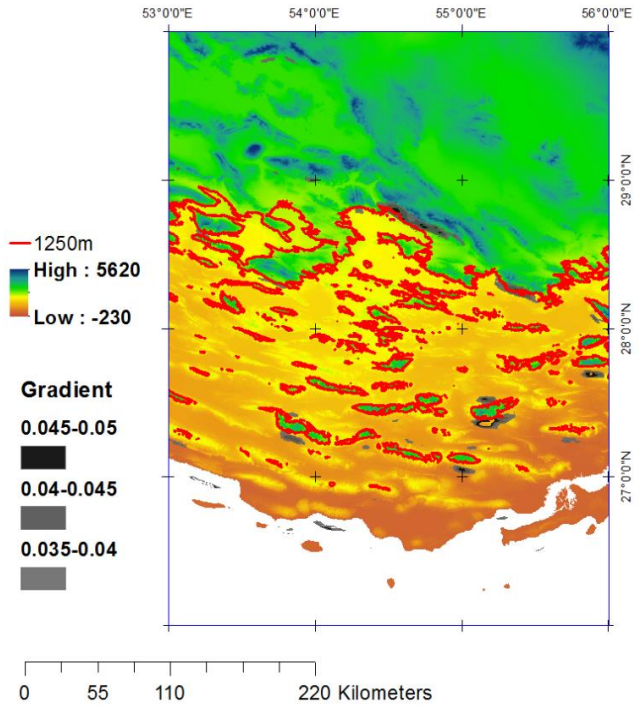

Figure 2.18: Overlaying those gradients with a high area- normalised number of earthquakes onto topography for the smaller sub-sector of the Zagros.

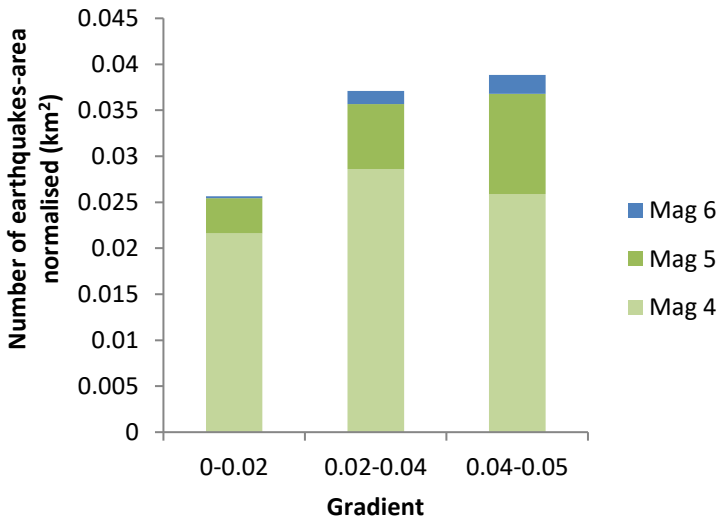

Figure 2.19: Grouping of gradients found in Figure 2.17 to obtain a more regional representation for the number of earthquakes occurring at different gradients within the sub-sector of the Zagros.

The graph of gradient against area-normalised number of earthquakes for the Qilian Shan is shown in Figure 2.21. Again, an increase in the number of earthquakes can be seen as the gradient increases. However, no earthquakes occur in the steepest regions which is contrary to what would be expected from the theory that gradient has an effect on earthquake activity.

It appears unlikely that such a small variation in slope over such small distances, as seen in the sub-sectors analysed in the Qilian Shan and the Zagros, would affect the stress distribution on a fault at depth. It is more likely that steep gradients are the result of localisation of thrusting, and could be used as a predictive tool. In conclusion; areas of steep gradients in active regions are probably more susceptible to earthquake thrusting. The lack of earthquakes in the steepest gradients within the Qilian Shan may be the result of the extremely small absolute difference in gradient between the various bands.

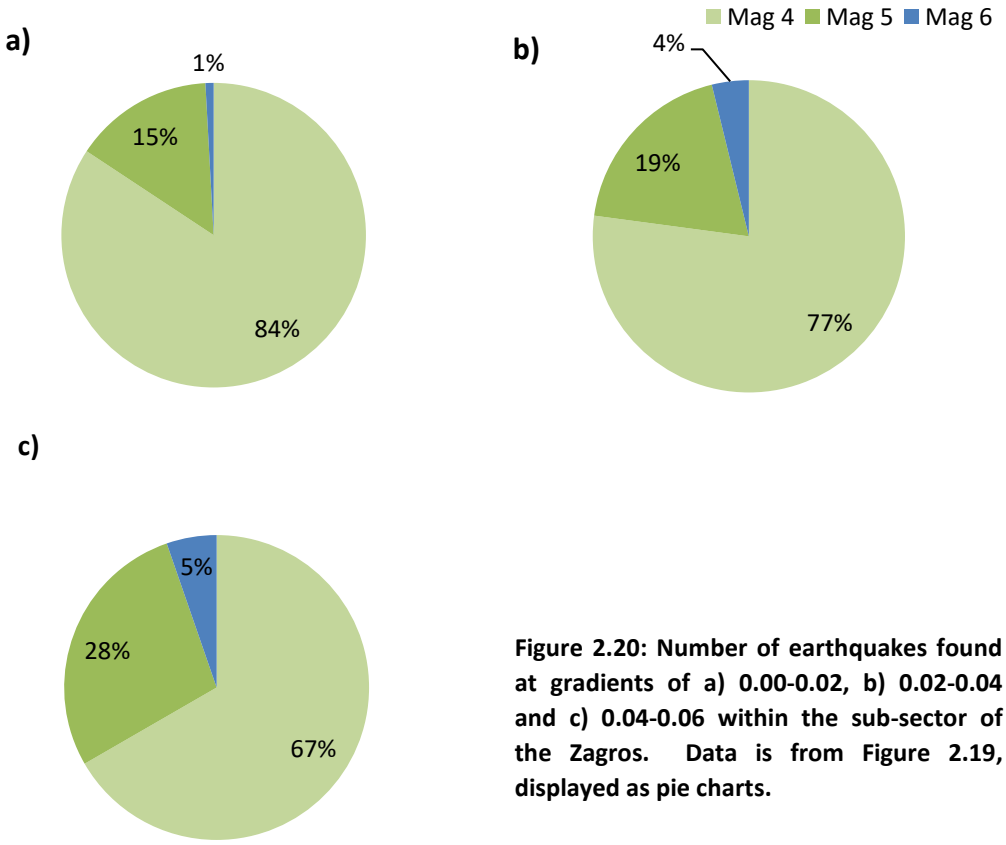

Figure 2.20: Number of earthquakes found at gradients of a) 0.00-0.02, b) 0.02-0.04 and c) 0.04-0.06 within the sub-sector of the Zagros. Data is from Figure 2.19, displayed as pie charts.

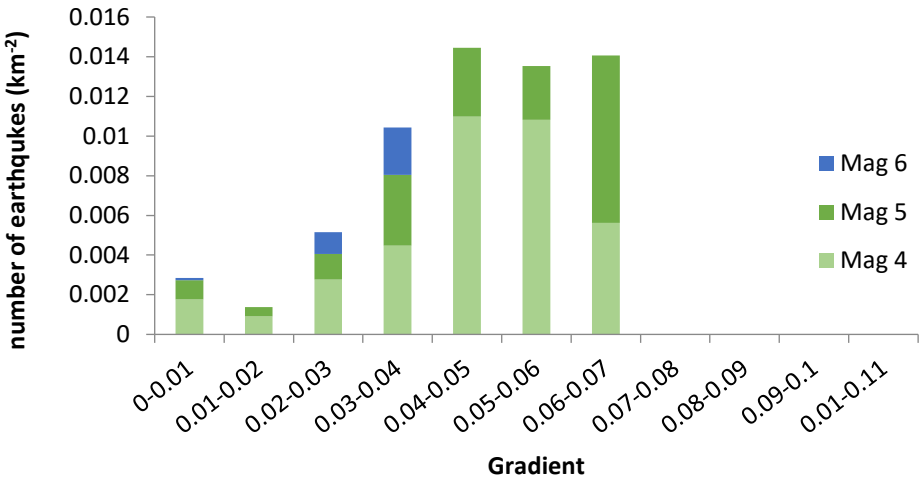

Figure 2.21: Area-normalised number of earthquakes occurring at different gradients for the selected sub-sector in the Qilian Shan as defined in Figure 2.2a.

2.3 Discussion

2.3.1 Overview of the magnitude vs topographic elevation relationship

Quantitative analysis was undertaken to evaluate the relationship between topographic elevation and earthquake magnitude in the Zagros (Figure 2.5). In addition, the possibility of a similar relationship within the Qilian Shan (Figure 2.12) and the Himalayas (Figure 2.10) has been explored. From the area-normalised work in the Zagros (Figure 2.7), the cut-off in seismicity associated with $M \geq 5$ earthquakes (Nissen et al., 2011) is also found to include $M = 4$ events. From this, it could be inferred that earthquakes of all sizes have the potential to 'cut-off' simultaneously. Therefore, in the Zagros a quantitative confirmation of the 1250 m cut-off in seismicity previously suggested by Nissen et al. (2011) is considered to be valid.

Such a clear conclusion could not be reached for the other two locations due to the paucity of data available. The inability of the Himalayan data to be area-normalised meant that a complete analysis of the area could not be undertaken. Earthquakes from the Qilian Shan were taken from such a small sub-sector that it has been shown to represent movement only on a few individual faults rather than portraying regional trends. This method of analysis, therefore, may be more applicable in some locations than others. Despite this, the thrust data (confirmed by the CMT catalogue) indicates an abrupt change in relationship between earthquakes and elevation at 3500 m (Figure 2.10) and 4000 m (Figure 2.12) in the Himalayas and Qilian Shan respectively.

Faults are so influenced by stress perturbations that to separate them into individual events is impossible and misrepresentative (Helmstetter & Sornette 2002). The interplay between earthquake events and the presence of aftershocks could be argued to perturb any relationship identified. However, dynamic stress transfer will merely induce or retard failure and should not affect the magnitude of different earthquake events (Freed 2005). The analysis presented here (Figure 2.16) of the Qilian Shan shows that the overall envelope of the graphs, and therefore the relationship between the two variables, is not affected by attempts at excising

aftershocks, despite reducing the data within the clusters by up to 60 %. Therefore, although aftershocks may misrepresent the frequency of large earthquakes, they have minimal influence on the limiting effect that topographic elevation has on earthquake magnitude.

The lack of focal mechanisms within the main NEIC dataset, and the poor relationship identified within the statistical analysis, call into question the validity of these initial graphs. The ability to associate a seismic cut-off with a single topographic elevation is arguably unrealistic when one considers the 'known unknown' of possible epicentre mis-locations by 10s of kilometres (Nissen et al. 2011). The inconsistency of epicentre location for the same events across different catalogues (see Section 2.1.1) is evidence for such errors.

This analysis was also conducted under the major assumption that small sub-sectors are representative of the whole deformation front. With varying convergence rates, structural signatures and the presence of different lithologies along the plateau fronts, one has to question the applicability of generalising across a range. Specifically, the presence of a weak decollement of salt in the south-east of the Zagros has been inferred to alter the tectonic behaviour and topographic profile from east to west (McQuarrie 2004). Such small sub-sectors can, in addition, be dominated by a few major faults (as observed within the Qilian Shan) which concentrate seismicity and present graphical trends which are not typical of the range. In summary, although the data is promising, the limitations within the dataset should not be underestimated.

2.3.2 The influence of energetics on earthquake magnitude and location

The uniformity of the seismicity cut-off of $M \geq 5$ thrusts at 1250 m within the Zagros (Figure 2.7), 4000 m in the Qilian Shan (Figure 2.12) and 3500 m within the CMT catalogue for the Himalayas (Figure 2.10) implies a consistent cut-off in seismicity at a certain elevation throughout a fold-and-thrust belt. Such a pattern appears more consistent with the G.P.E. or 'minimum work' hypothesis than the critical Coulomb wedge hypothesis. However, the energetics associated with an earthquake are extremely complex, being affected by; host rock

lithology, the dynamic & static frictional values of the fault, depth, pressure, temperature, geochemistry & pressure of the pore fluid and the mineralogy of the fault zone. Fault zone properties can be highly variable even between separate earthquake events on the same fault surface (Shipton et al. 2006). Therefore, the likelihood of a uniform cut-off in seismicity given such a heterogeneous geology appears somewhat counterintuitive. Furthermore, the energy released in the seismic moment is relatively low (between 5-20 % of the energy budget) and, therefore, reducing the seismic moment does not 'free up' much energy to use against an increasing G.P.E.

However, if the damage zones which are associated with faulting are taken into consideration, there is a significant increase in the amount of energy consumed in an earthquake event. Internal deformation is the main sink of energy and is associated with the extent of damage zone deformation (Shipton et al. 2006). Earthquake magnitude is associated with earthquake length. Therefore, as faults connect and grow over time, larger earthquakes may be associated with more complex damage zones and hence larger energy sinks. Thus, although reducing the seismic moment itself does not 'free up' much energy, the reduction in internal deformation does. The reduction in large magnitude earthquakes could 'free up' sufficient energy to offset against increased G.P.E.

Notwithstanding the above complexities of an earthquake system, a minimum work model does appear to offer an explanation for the observed increase in large magnitude earthquakes as the cut-off is approached. As larger earthquakes require more energy, one would expect the proportion of $M \geq 5$ earthquakes to reduce with elevation due to the increasing demand of G.P.E. on the energy budget. Instead, the opposite trend is seen. Modelling by Masek & Duncan (1998) proposes that faults remain active because of weakening when they are far from gravitationally stable. This suggests that deformation will not respond to slight variations in topography if the minimum work to deform along a pre-existing weak plane is less than that of forming a new fault surface at a lower elevation. Therefore, fewer, larger, more stable faults could be the most favourable energetic formation, at least for a time until a critical elevation where the work against gravity is just too extensive (Masek & Duncan 1998). This

matches well with evidence presented throughout this chapter, and as such supports the idea of a system that is at least influenced by minimum work processes.

2.4 Conclusion

This chapter has examined the relationship between topographic elevation and earthquake magnitude in addition to exploring the significance of gradient. From this analysis it can be concluded that seismicity appears to cut-off in the Zagros at the 1250 m contour as expected from previous analysis (Nissen et al. 2011), and applies to smaller earthquakes ($M < 5$) than previously suggested. In the Himalayas and the Qilian Shan the method was more problematic. However, a cut-off in thrust earthquakes has been found at elevations of 3500 m in the Himalayas and 4000 m in the Qilian Shan. In addition, it is found that the proportion of large magnitude earthquake increases with elevation and, as a result, minimum work processes are influential on earthquake distribution.

The variation in elevation of the seismicity cut-off, between that seen in the Himalayas/Tibetan Plateau (3500 - 4000 m) and that seen in the Zagros (1250 m) could be due to different stages within the orogeny's lifetime. Alternatively, a variation in the convergence rate could affect the energy balance of a fold-and-thrust system and, as a result the maximum elevation which could be obtained. The latter matches well with the data presented here as the convergence rates found in the Zagros and the Himalaya are 6.5 +/- 2mmyr^{-1} (Vernant et al. 2004) and 15-20 mmyr^{-1} (Zhang et al. 2004) respectively.

2.5 Future work

An obvious direction for future work would be to extend this analysis to a greater number of fold-and-thrust belts. In particular, it would be of interest to examine additional fold-and-thrust belts on the fringes of the Tibetan Plateau to see if the orogeny displays a single universal cut-off in seismicity. If this is the case it would further support the idea of an energetically controlled system. Extending the sub-sector examined in the Qilian Shan to create a larger dataset may allow for a more accurate characterisation of the magnitude elevation relationship. Area-normalisation within the Himalayas would give a representation of the proportional increase in large earthquakes with elevation and could be used to support trends seen at other locations.

An additional avenue to explore would be the relationship between lithostatic load and earthquake magnitude. Hypothesis 3, set out in Chapter 1, postulates that an increase in lithostatic load creates a thicker zone of distributed deformation within the sedimentary layer which suppresses large earthquakes. The lithostatic load at any point will depend on the height of the column of rock above it, which in turn depends on the earthquake hypocentre. This parameter could provide an alternative to height above mean sea level (topographic elevation) as a correlant for earthquake behaviour.

Limitations with the dataset prevented the exploration of this relationship within this study. Although each earthquake is assigned a 'depth', nowhere within the NEIC catalogue, from which the bulk of the data is taken, does it indicate the datum line to which such depths are relative. The Earthquake Hazard Program indicated (pers. comm.) that the depth reference frame is dependent on the event, and that the inaccuracies within depth measurements rendered the frame irrelevant. It is therefore not possible to establish whether the depths given are relative to mean sea-level or to the topographic surface. Furthermore, where an accurate depth measurement could not be obtained, an arbitrary value of either 33 km or 5 km was assigned. In the particular case of the Zagros data, hypocentre locations were suggested which were well below the approximate 40-55 km depth of the Moho (Paul et al. 2010; Nissen et al. 2011). This

is clearly unlikely. Such unknowns within the data render it not possible to explore the relationship between lithostatic load and magnitude. Should more accurate depth data be established then this would be a clear topic for future work.

Chapter 3

Analysis of the regional topography via swath profiles

3. Analysis of the regional topography via swath profiles

This chapter investigates the critical Coulomb wedge model as an explanation for the reduction in $M \geq 5$ earthquakes via the quantitative identification of plateau edges. In addition to topographic profile analysis for the specific regions under evaluation, this project has developed a generic quantitative method for identifying the location of a plateau edge. This is the first time that such a numerical analysis of a plateau's geometry has been reported. The technique will be of wider application in studies of fold-and-thrust wedges.

Within this chapter the term 'transect' refers to a single profile through a region. A 'swath profile' refers to the condensed elevation data of a corridor through a region and the 'swath profile width' refers to the half width of that corridor (Figure 3.1a). For example; a swath width of 50 km would consider elevations over a corridor of total width 100 km. For each point along the transect the swath profile calculates a 'maximum', 'minimum' and 'average' topography. The 'maximum' and 'minimum' refer to the maximum and minimum elevation within a corridor at any given point along the transect. The 'average' profile represents the average elevation of the corridor at that point along the transect (Figure 3.1b). The Maximum, minimum and average values for each swath profile are computed automatically by the 'Path Profile' tool in Global Mapper. The complete collection of swath profiles is given in Appendix B.

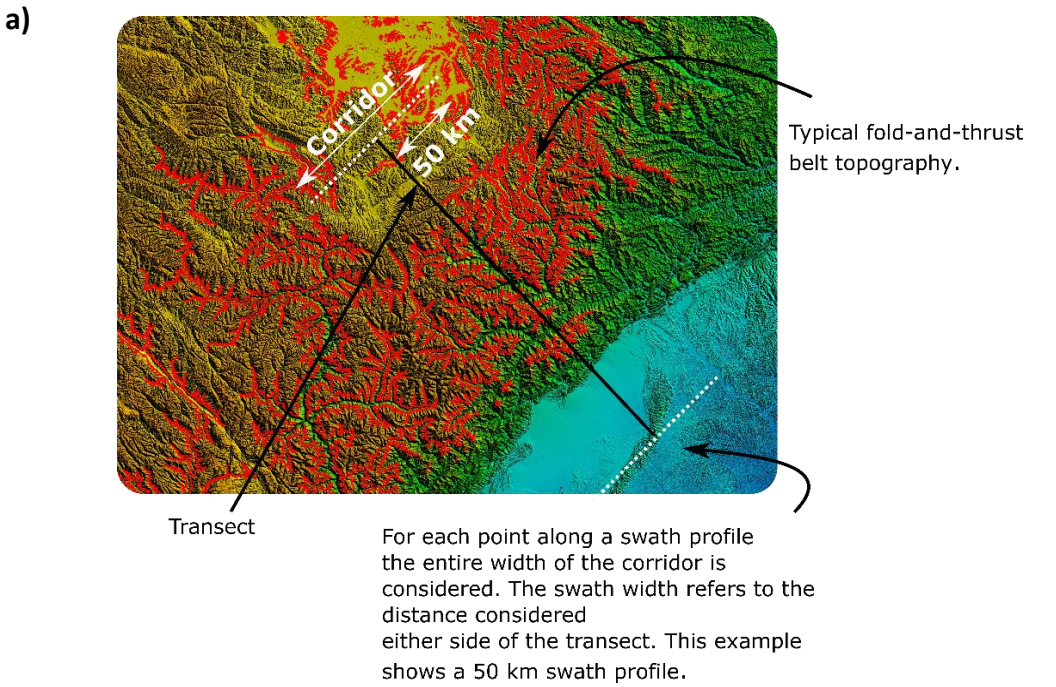

Figure 3.1 a) Diagram explaining nomenclature used in transect analysis. b) Example of a corridor at any given point along the transect. The maximum, minimum and average points, as referred to in the analysis presented herein, are identified for this particular corridor.

3.1 Context

Arguments have been put forward in the literature both for and against the critical Coulomb wedge model. For example; the geometry within the Zagros varies drastically along the deformation front with contrasting profiles in the Lorestan & Fars regions and the Dezful Embayment (McQuarrie 2004). Similarly, analysis comparing the strongly concave steep hinterland of Nepal to the mildly convex profile in Bhutan interpreted the difference as tectonic segmentation along the range (Duncan et al. 2003). On the other hand, modelling work undertaken for both the Longmen Shan (Sun et al. 2016) and the Himalayas (Grandin et al. 2012) was consistent with lateral segmentation in topography and tectonic growth on a single decollement, supportive of the model. Further support in the case of the Longmen Shan comes from the fact that seismic reflection along the deformation front and through the Sichuan Basin shows thrusts flatten and merge into a basal decollement (Hubbard & Shaw 2009).

It was beyond the scope of the present study to assess the existence or otherwise of Coulomb wedge structures in the four regions analysed. Instead, the starting assumption was that such structures do exist and their ability to explain the seismicity cut-off was then evaluated. The extent to which the Coulomb wedge model can offer an explanation for the observed seismicity cut-off does, of course, provide indirect evidence for the existence of the wedge structure.

The original critical Coulomb wedge model predicts that a fold-and-thrust belt should display a constant taper angle (Roe & Brandon 2011) on the assumption that the wedge is homogenous. Changes in topographic slope have previously been attributed to heterogeneities in the strength of the wedge material and/or in the frictional properties along the basal decollement (Dahlen 1990) which alter the ratio of applied basal shear stress to the strength of the material in the base of the wedge. Present day geothermal gradients place the brittle-plastic transition for quartz and feldspar at depths of 12-16 km, rendering the original Coulomb theory not applicable in the interior of high mountain ranges (Davis et al. 1983). Developments to the original model, in particular by Williams et al. (1994) but also Vanderhaeghe et al. (2003)

suggest that a change in deformation mechanism can underlie these changes in strength and friction. Specifically, the Williams et al. (1994) model identified that the transition from steep slopes of the mountain front to a plateau is related to the transition from brittle to ductile behaviour first in the lower wedge and then on the decollement (Figure 3.2).

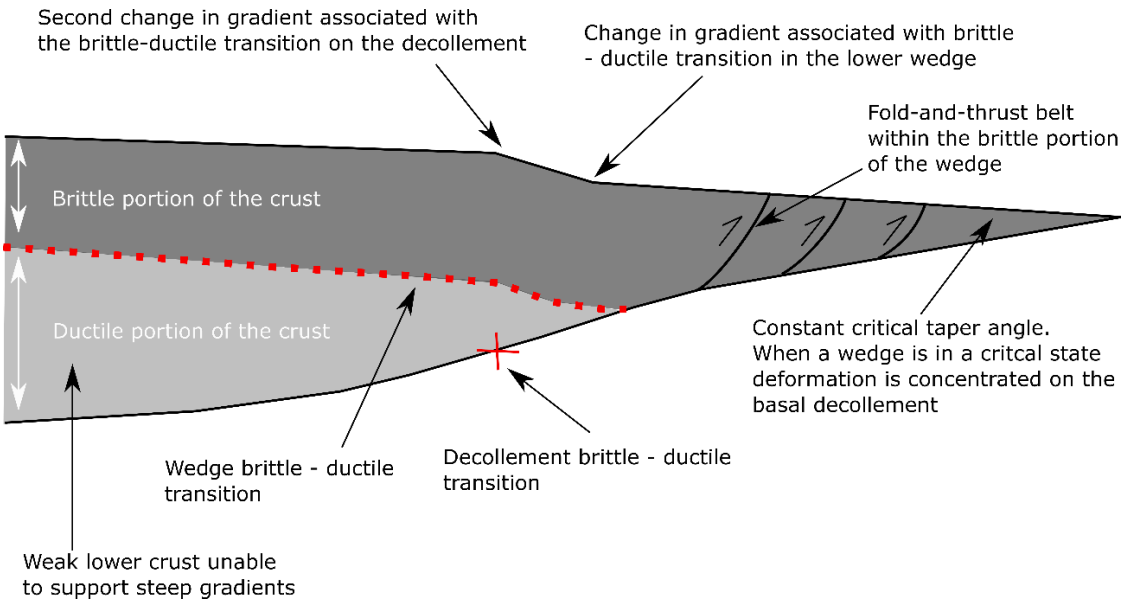

Figure 3.2: Schematic representation of Williams et al's (1994) brittle-ductile critical Coulomb wedge model. The red dotted line represents the brittle-ductile transition within the lower wedge and 'X' the brittle-ductile transition on the basal decollement. For full parameters of the model see original paper.

When a wedge is in a critical state, deformation is localised along the basal decollement (Wang & Hu 2006; Dahlen et al. 1984; Dahlen 1990). If Williams et al.'s (1994) model (Figure 3.2) also applies, then the change in surface gradient will correspond to the onset of incipient ductility on the basal decollement. This in turn will inhibit seismogenesis in the region of the basal plane (which is where all the deformation is occurring). This would result in a seismic cut-off corresponding to the change in gradient. Williams et al. (1994) also include in their model the transition from brittle to ductile behaviour in the lower wedge (Figure 3.2). Large scale thrusts would be unlikely in areas were the lower wedge was ductile and therefore weak. Such areas would be associated with flattened topologies. It can be seen that there is evidence to warrant an investigation into the relationship between plateau geometry and the distribution of large thrust earthquakes.

3.2 Methodology for calculating the plateau edge

Within this study the methodology was varied to take into account the differences in size and curvature of the four study locations. Locality-specific parameters are described within the respective results sections. Swath profiles were taken from the original Shuttle Radar Topography Mission (SRTM) digital elevation data (90 m resolution) prior to any regional topographic smoothing. Initial swath profiles were taken over a range of widths and their elevations were smoothed using a running average in order to obtain the most accurate representation of the regional topography. In addition, smoothing eliminates any local topographic variations (for example; the effects of local fold and thrust structures). Running averages of ± 10, ± 20 and ± 50 readings were compared at all locations: ± 50 was found to provide the most accurate representation of regional trends. Swath profiles were taken approximately parallel to the axis of maximum deformation, assumed here to be perpendicular to the deformation front[2].

Gradient and curvature measurements were obtained from the average swath profiles. In the majority of cases these provided an appropriate representation of the region, but in cases where a notably concave minimum profile cut back into the plateau edge the average swath profile was significantly altered. However, in order to maintain consistency the average profile was used regardless.

[2] As previously defined in Chapter 2, the deformation front is the limit of discernible deformation related to the fold-and-thrust belt, closest to the foreland.

Gradient estimates were taken at each elevation point by calculating the difference in values either side of the point. Thus; if elevation values along the transect were to be labelled *1,2,3,4…n* then the gradient at point *n* was found by the following equation:

$$Gradient\ at\ point\ n = \frac{(n+25)th\ value - (n-25)th\ value\ of\ the\ elevation}{(n+25)th\ value - (n-25)th\ value\ of\ the\ distance} \qquad \text{Eq. 3.1}$$

Where elevation corresponds to the Y axis and distance to the X axis

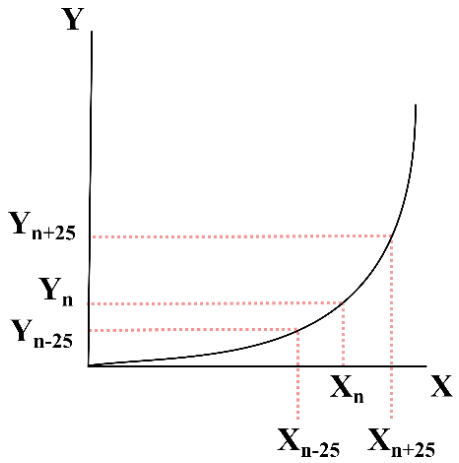

The 25th value either side of *n* was chosen as this represents half the resolution of the smoothing factor (± 50).

The curvature of the topographic profile at any one point is defined as the rate of change of gradient. A value for the curvature was obtained by:

$$Curvature\ at\ point\ n = \frac{(n+25)th\ value - (n-25)th\ value\ of\ the\ gradient}{(n+25)th\ value - (n-25)th\ value\ of\ the\ distance} \qquad \text{Eq. 3.2}$$

Whether the topographic profile was concave or convex at any given point could be ascertained from the curvature. A negative value for curvature indicated a convex topography whereas a positive value indicated a concave topography (Figure 3.3). Figure 3.4 is an example of the process of obtaining a curvature graph from the Himalayas.

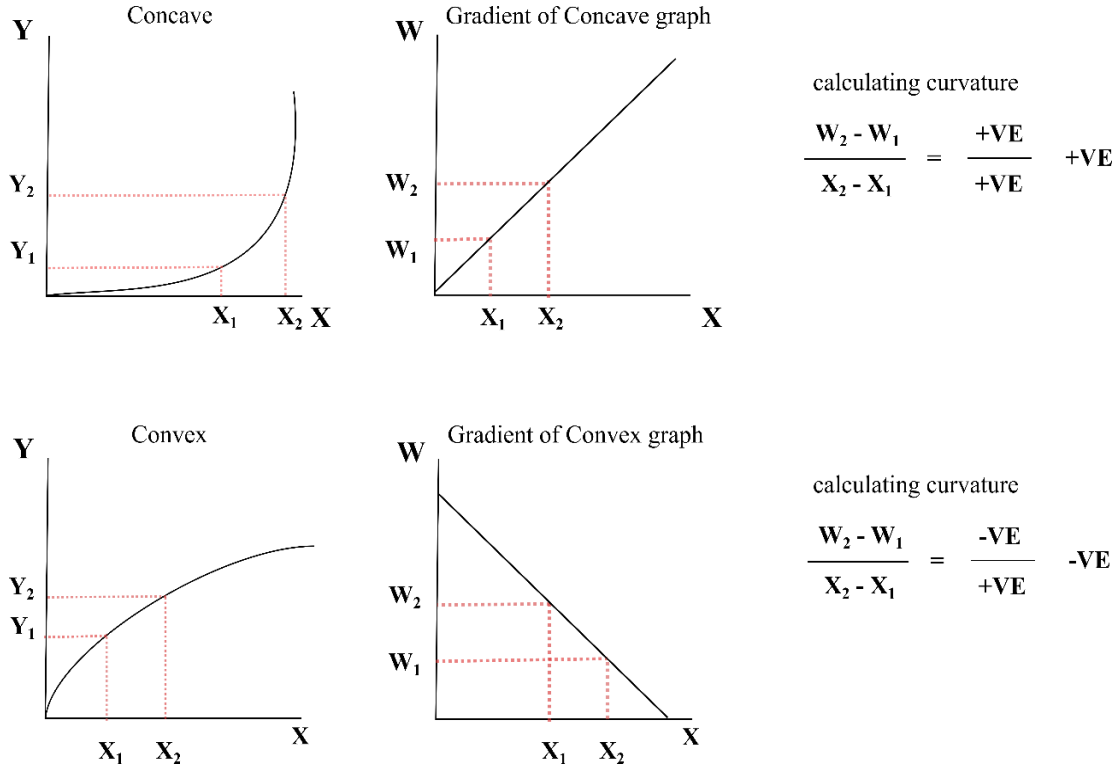

Figure 3.3: Schematic example of how positive and negative gradients within the curvature graphs relate to the convex or concave nature of the original topographic graph.

Calculated curvature values allowed a quantitative identification of the plateau edge which could be validated by additional information from the gradients and average topographic profiles. The exact location of the plateau edge was identified at the most negative value within the broadest convex region (Figure 3.5). Where transects presented multiple sections of negative curvature, the broadest section was taken as the plateau edge irrespective of its negative magnitude. Where this led to any ambiguity, plateau edges could be validated by checking sections of negative curvature with locations where the succeeding gradient trends towards zero (Figure 3.6). Plateau edges extracted from multiple swath widths were compared to ensure consistency of the method.

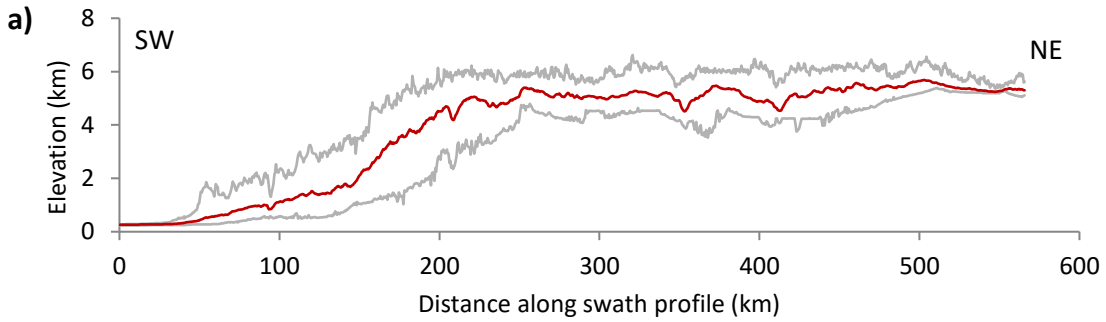

a) Swath profile taken through the Himalayas (Transect 1) prior to any smoothing. Swath profile width is 50 km.

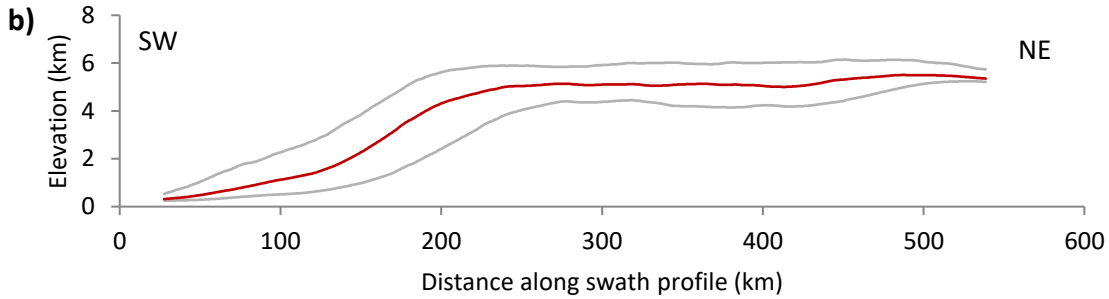

b) Transect 1 from the Himalayas as seen in a) having been smoothed using a running average of ±50. Such smoothing removes noise from graphs so that only the regional topography remains.

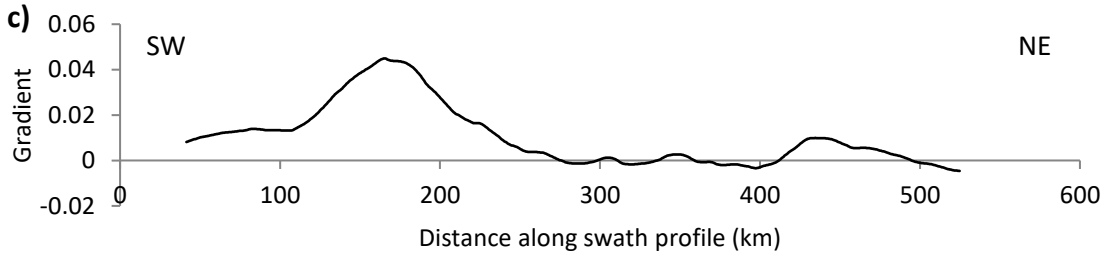

c) Gradient taken from the smoothed topography seen in b) via the method described in this report

d) Curvature graph found by taking the gradient of the gradient graph c). The peak in curvature within the broadest negative trough is then established from this graph as the plateau edge.

Figure 3.4: Step by step example of creating a curvature graph from the original swath profile data. Elevation is relative to mean sea level. The averaged topography can be seen in red. The grey lines above and below represent the maximum and minimum profiles respectively.

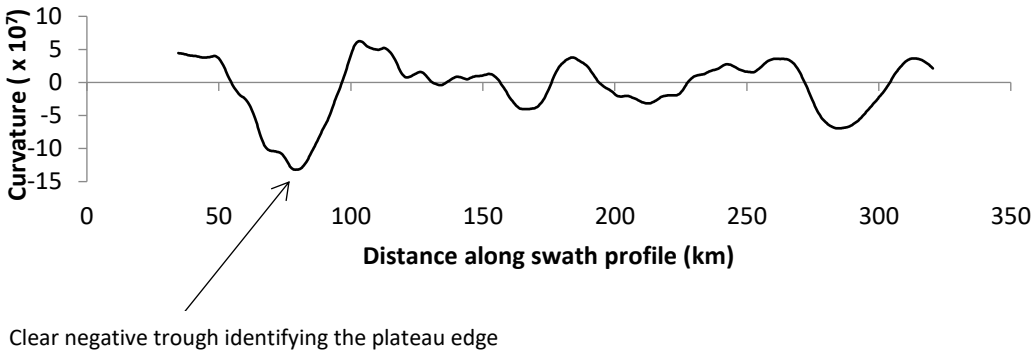

Figure 3.5: Example of an easily identifiable plateau edge. The presence of one clear negative trough within the curvature graph enables an easy identification of the plateau edge. The example is taken from Transect 1 from the Zagros.

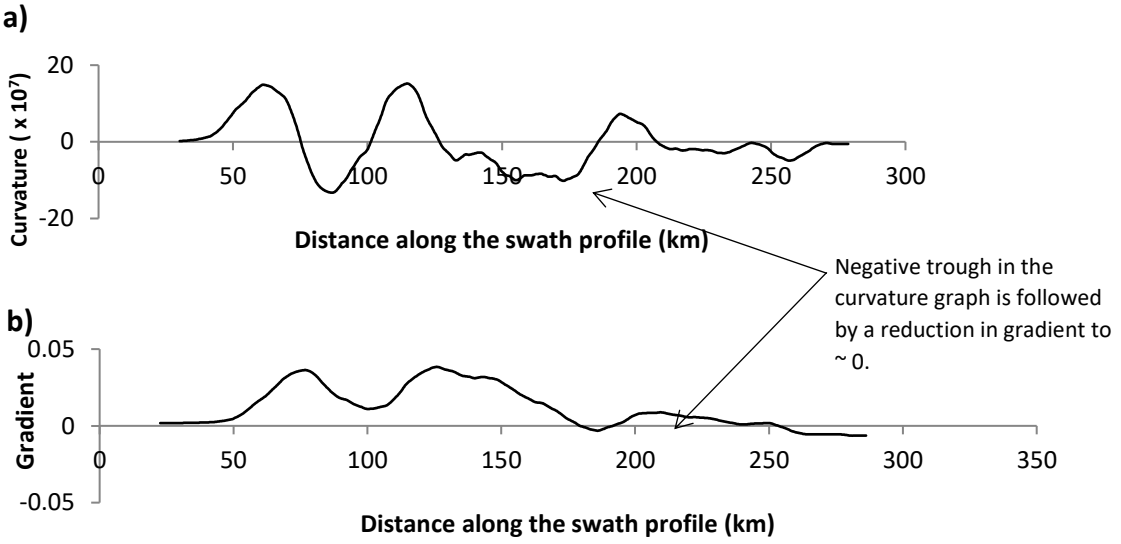

Figure 3.6: a) An example of a curvature graph which contains a lot of noise and b) the corresponding gradient graph along the average swath profile. Two distinctive negative troughs can be seen within the curvature graph. The plateau edge is found via a combination of the gradient and curvature graphs. The broadest negative trough is selected within the curvature graph. The result is then checked by ensuring the gradient drops to zero after this plateau edge. The example here is Transect 3 through the Longmen Shan.

3.3 Swath profile results

3.3.1 The Zagros, Iranian plateau

Initial swath profiles of 5 km, 50 km and 100 km were taken from the deformation front to the northward limit of the 'Main Zagros Reverse Fault'. The northern limit was chosen as it is the proposed suture line between the former Arabian continental margin and central Iran to the northeast (Talebian & Jackson 2004).

Across the swath profiles the deformation axis did not always remain parallel to the transect due to curvature of the plateau front. This is represented schematically in Figure 3.7. Narrower swath profiles helped avoid this issue. The smoothest representation of the regional topography within the Zagros was presented using a 100 km swath profile width. However, as a result of the curvature of the mountain front the extremities of the 100 km swath profiles are no longer parallel to the axis of maximum deformation. A 50 km swath profile width was chosen

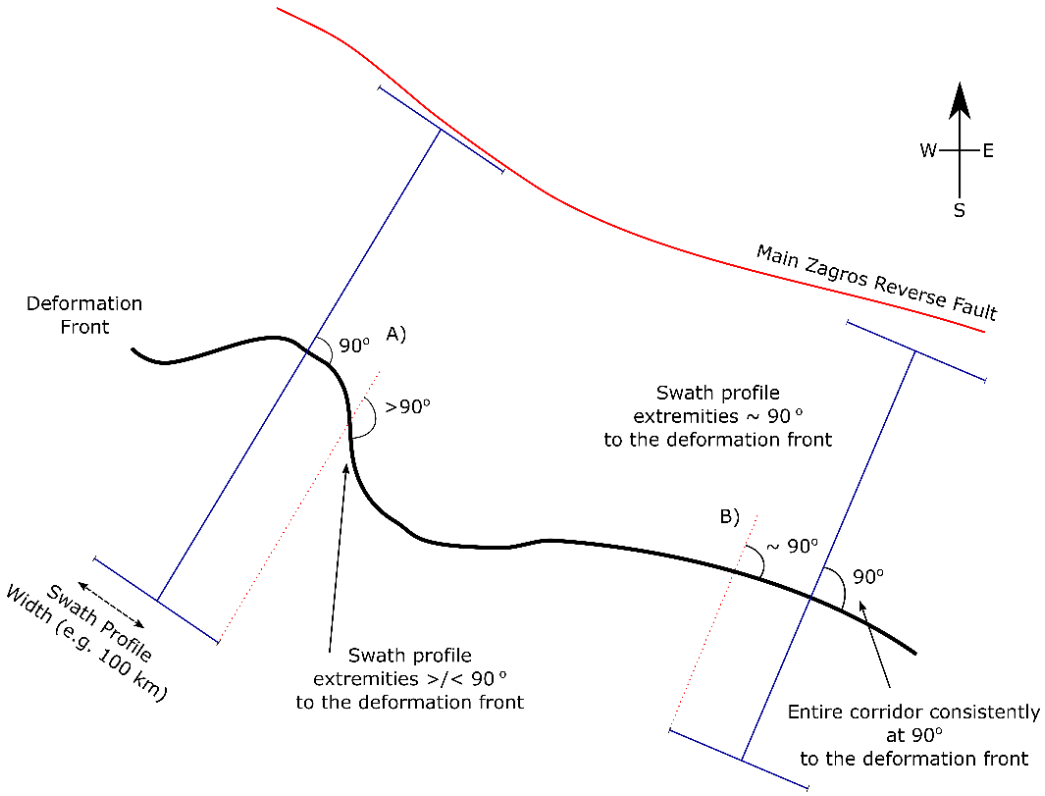

Figure 3.7: Schematic diagram representing effect curvature of the deformation front has on the selection of swath profile width. The Zagros is used as an example. The swath profile A) is an example where the extremities are no longer at 90° to the deformation front whereas B) is an example where curvature of the deformation front is not an issue.

as a compromise which represents the regional topography acceptably whilst the extremities remain close to parallel with the axis of maximum deformation. A 50 km swath profile width is also comparable to previous studies of the Zagros by Allen et al. (2013).

Figure 3.8 presents the plateau edges as defined by the 50 km and 100 km swath profiles. Swath profiles were taken every 70 km (± 10 km) perpendicular to the deformation front. Swath profiles that remained perpendicular to the deformation front were prioritised over maintaining the 70 km uniform distance between each profile. Within the Dezful Embayment, changes in gradient were abrupt and as a result the associated plateau edge was easily identified. In comparison, the Fars region possessed a gradual change in slope, presenting a less abrupt plateau edge and a greater amount of noise within the curvature graph. Examples of these two profile extremes are shown in Figure 3.9.

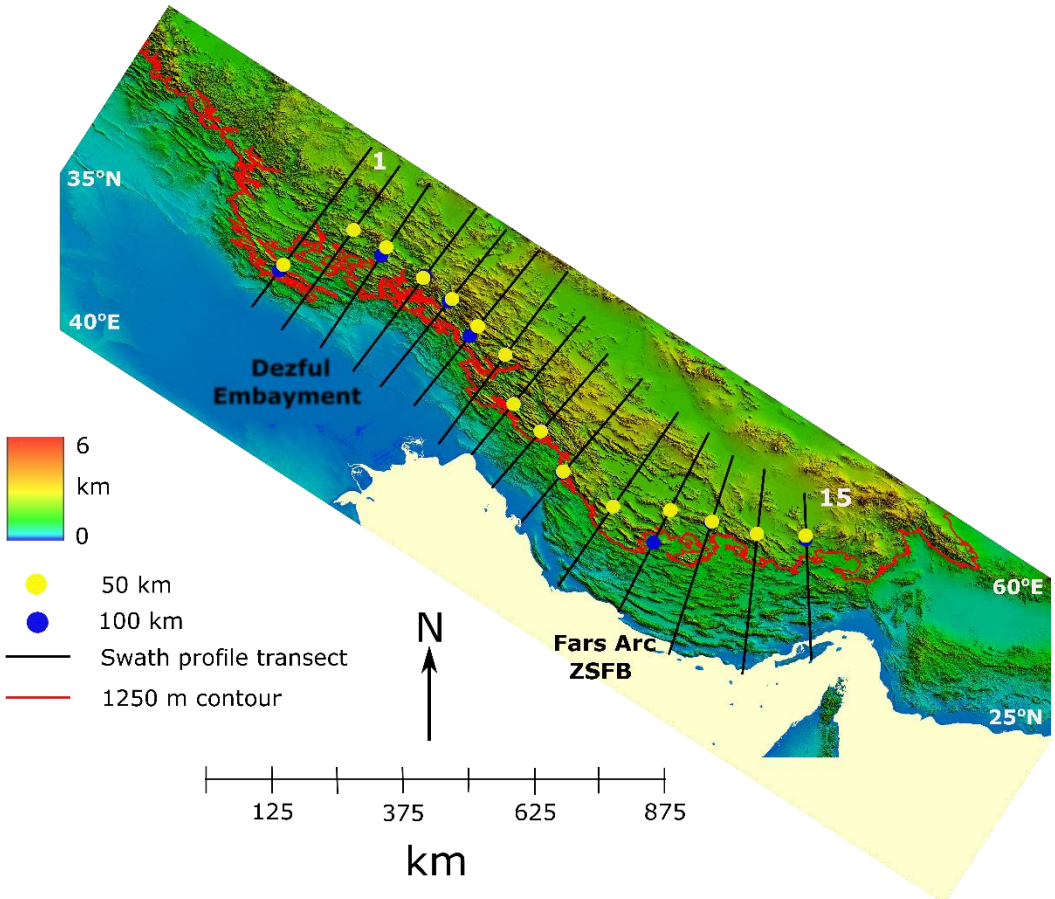

Figure 3.8: Location of the Transects and associated plateau edges within the Zagros. Transects are numbered from 1-15 from west to east. Blue dots present the plateau edge as defined by the 100 km swath profile and yellow dots present the plateau edge as defined by the 50 km swath profile. The previously defined cut-off in M ≥ 5 earthquakes (Nissen et al 2011) is identified by the red 1250 m contour. Where one dot appears to be absent it is a result of the exact locations of the plateau edge in the two different swath profiles overlapping.

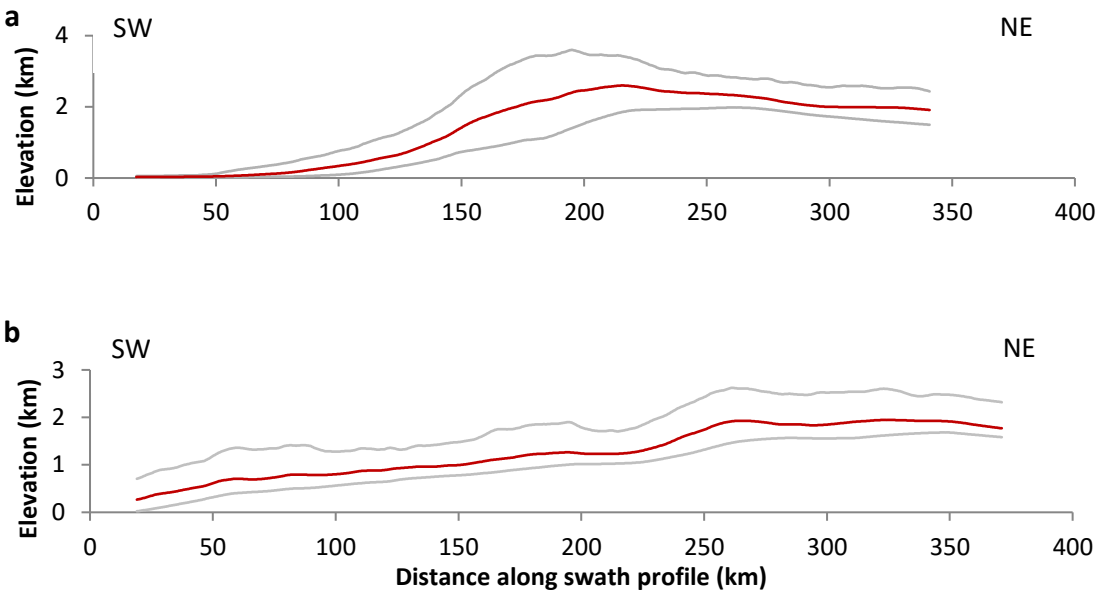

Figure 3.9: a) Transect 5 throught the Dezful Embayment showing steep gradients and a more prominent plateau edge b) Transect 13 through the Fars region presenting a more gentle topography and less well defined change in slope. The averaged topography for the 50 km swath profile can be seen in red. The grey lines above and below represent the maximum and minimum profiles respectively. Elevation is relative to mean sea level.

There is good agreement between the plateau edge defined from both the 50 km and 100 km swath profile widths (Figure 3.8). However, profiles 3, 6 and 12 show 20-70 km offsets between the plateau edges defined from the two different swath profile widths. The three profiles, and their respective curvature graphs, for both the 50 and 100 km profile width, are shown in Figure 3.10. These swath profiles all correspond to locations where the plateau is curving significantly and, therefore, the extremities of the average swath profiles do not remain perpendicular to the axis of maximum deformation. The offset is thought to be caused by the 100 km swath profiles being skewed as a result of the curvature of the mountain front. However, not all inflections in the deformation front are associated with such inconsistences in the plateau edge, indicating other factors potentially contributed to the variation. Regardless, these profiles were subsequently removed from the study so that only profiles with a confidently identified plateau edge were analysed. Figure 3.11 presents a modified basemap displaying all the remaining transects.

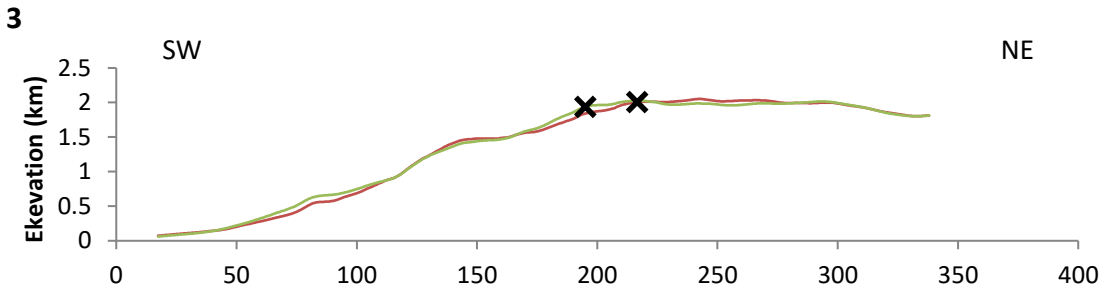
3
SW
NE
Ekevation (km)
2.5
2
1.5
1
0.5
0
0
50
100
150
200
250
300
350
400

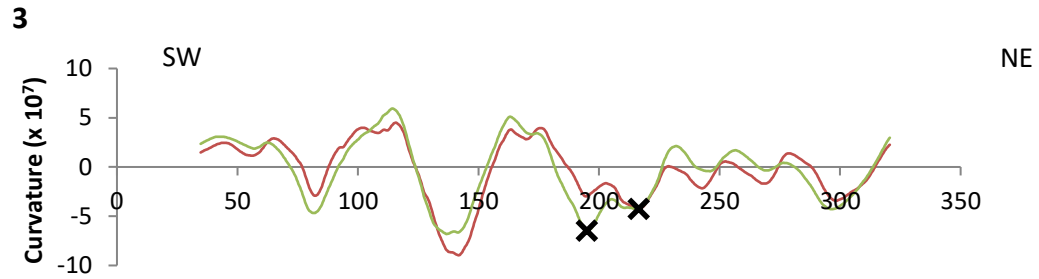
3
SW
NE
Curvature (x 10⁷)
10
5
0
-5
-10
0
50
100
150
200
250
300
350

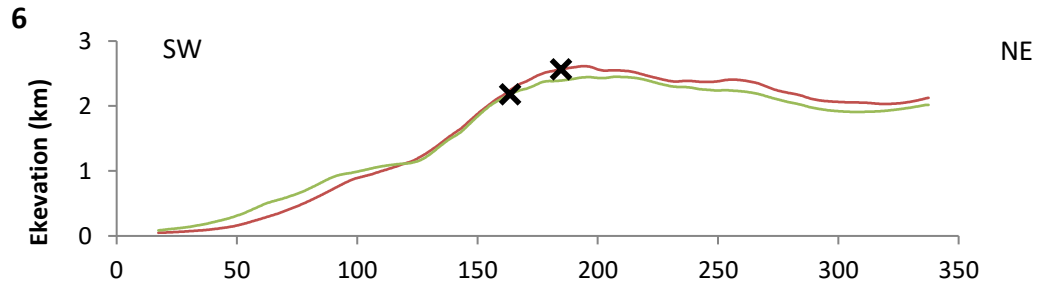
6
SW
NE
Ekevation (km)
3
2
1
0
0
50
100
150
200
250
300
350

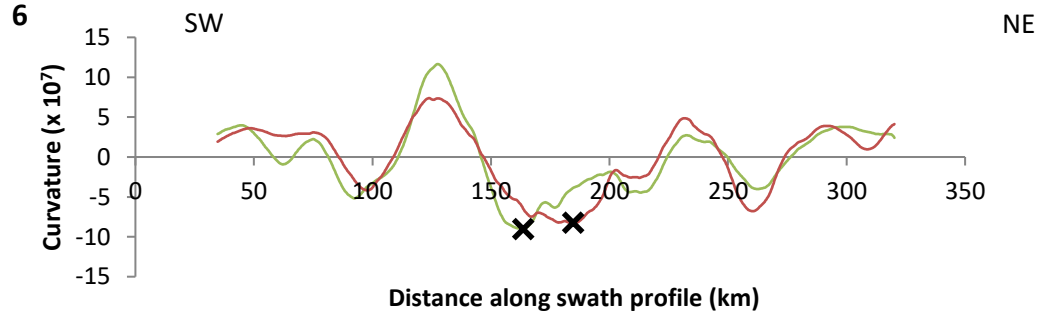
6
SW
NE
Curvature (x 10⁷)
15
10
5
0
-5
-10
-15
0
50
100
150
200
250
300
350
Distance along swath profile (km)

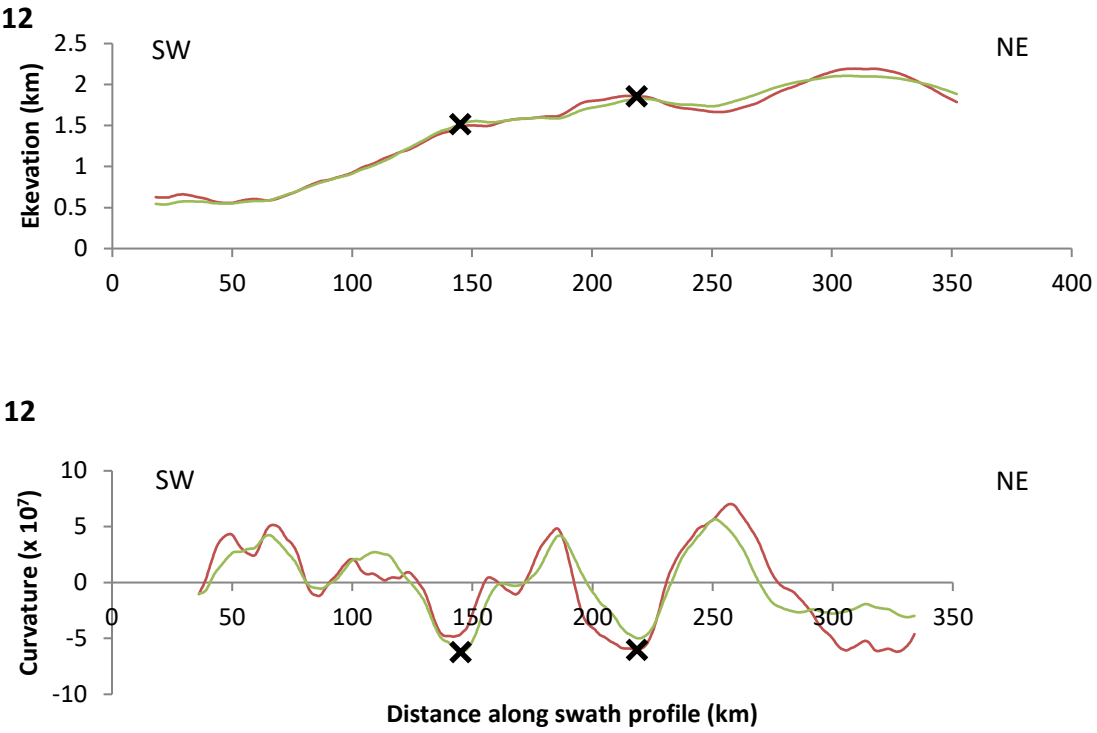

Figure 3.10: Topographic profiles and curvature graphs for Transects 3, 6 and 12. The number associated with each graph represents the Transect to which it relates. These were consequently removed from the dataset due to inconsistencies seen in the plateau edges extracted from the 50 km and 100 km profiles. 50 km profiles can be seen in red and 100 km profiles in green. The data is taken from the average swath profile and smoothing is applied by running averages of ±50 to the original average topographic swath profile. Elevation is relative to mean sea level and in all cases Transects were taken from SE to NW. The black 'X' within each graph represents the plateau edge as defined from the curvature graph.

The modified plateau edge has been found to sit at a higher elevation than the 1250 m contour line associated with the cut-off in M ≥ 5 thrust earthquakes. The distance between the plateau edge and the 1250 m contour varies between 20 km and 70 km in the west and is ~50 km in the east. Broadly, the fit to the 1250 m contour appears to be better in the west. The difference in the plateau edge elevation and the 1250 m contour could be the result of the previously defined (Nissen et al. 2011) 1250 m contour having been taken from a smoothed elevation plot. The contour line presented here is from raw, unsmoothed data.

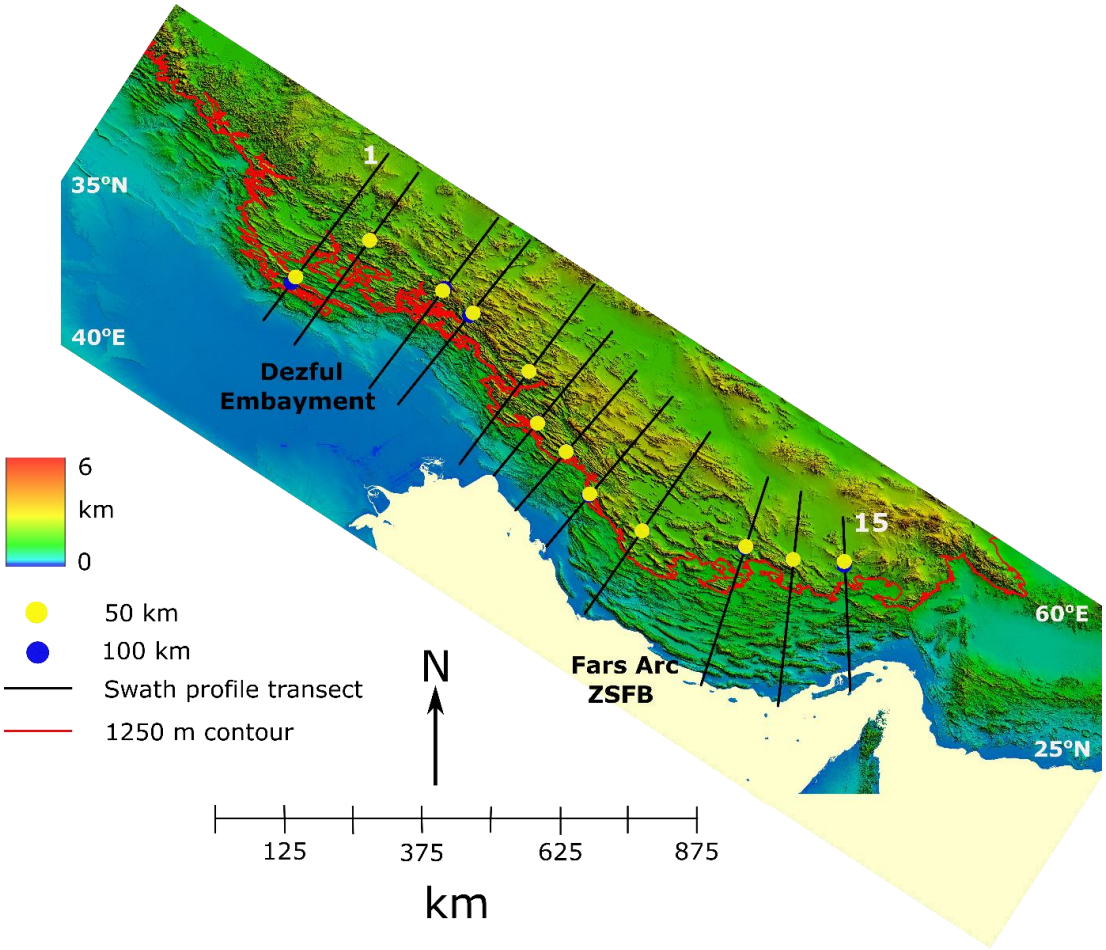

Figure 3.11: Location of the Transects and associated plateau edges within the Zagros with Transects 3, 6 and 12 having been removed. Transects are numbered from 1-15 from west to east. Blue dots present the plateau edge as defined by the 100 km swath profile and yellow dots present the plateau as defined by the 50 km swath profile. The previously defined cut-off in M ≥ 5 earthquakes (Nissen et al 2011) is identified by the red 1250 m contour. Where one dot appears to be absent it is a result of the exact locations of the plateau edge in the two different swath profiles overlapping.

3.3.2 The Himalayas

Swath profiles of 10 km, 50 km and 100 km widths were taken in the Himalayas at 400 km intervals. The locations of these Transects are shown in Figure 3.12 and the average topography profile for each are presented in Figure 3.13. Unlike the Zagros, the curvature of the front was not an issue due to the scale of the Himalayas. The 100 km and 50 km average swath profiles in the Himalayas showed only minor topographic differences except for Transect 3 which showed a small offset of 40 km. Figure 3.15 shows the 50 km and 100 km swath profiles through Transect 3. Uniquely for this swath, the maximum and minimum profiles differ significantly. The strongly concave nature of the minimum profile implies this offset may be the result of a major river, such as a tributary of the Kosi or the Ganga rivers (Petr & Swar 2002), cutting back the plateau edge.

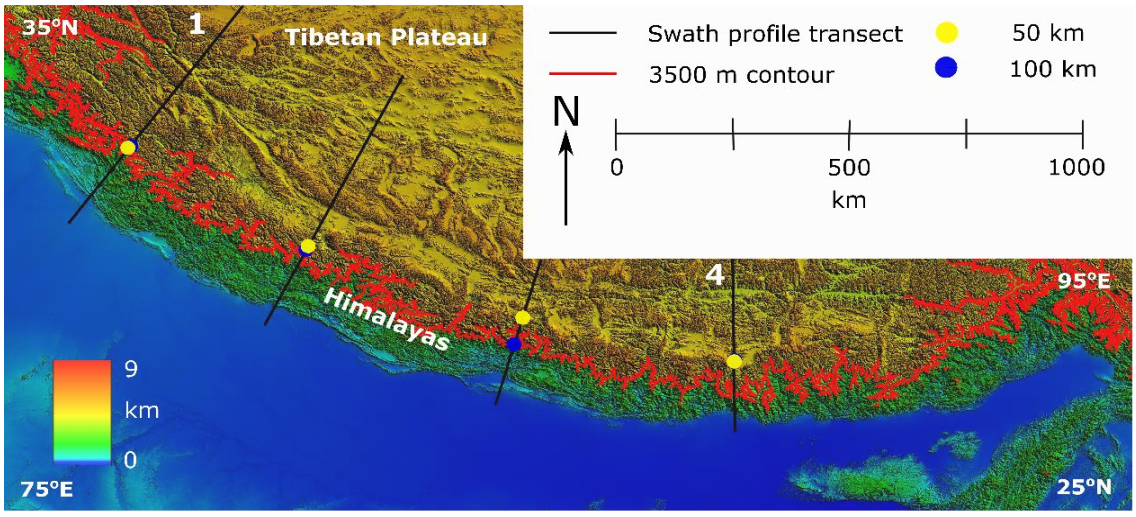

Figure 3.12: Locations of Transects 1-4 and associated plateau edges taken from W to E through the Himalayas. The red line indicates the 3500 m contour at which the M ≥ 5 earthquakes within the CMT catalogue were found to disappear. The yellow dots indicate the plateau edge at 50 km and the blue at 100 km. Where one dot appears to be absent it is a result of the exact locations of the plateau edge in the two different swath profiles overlapping.

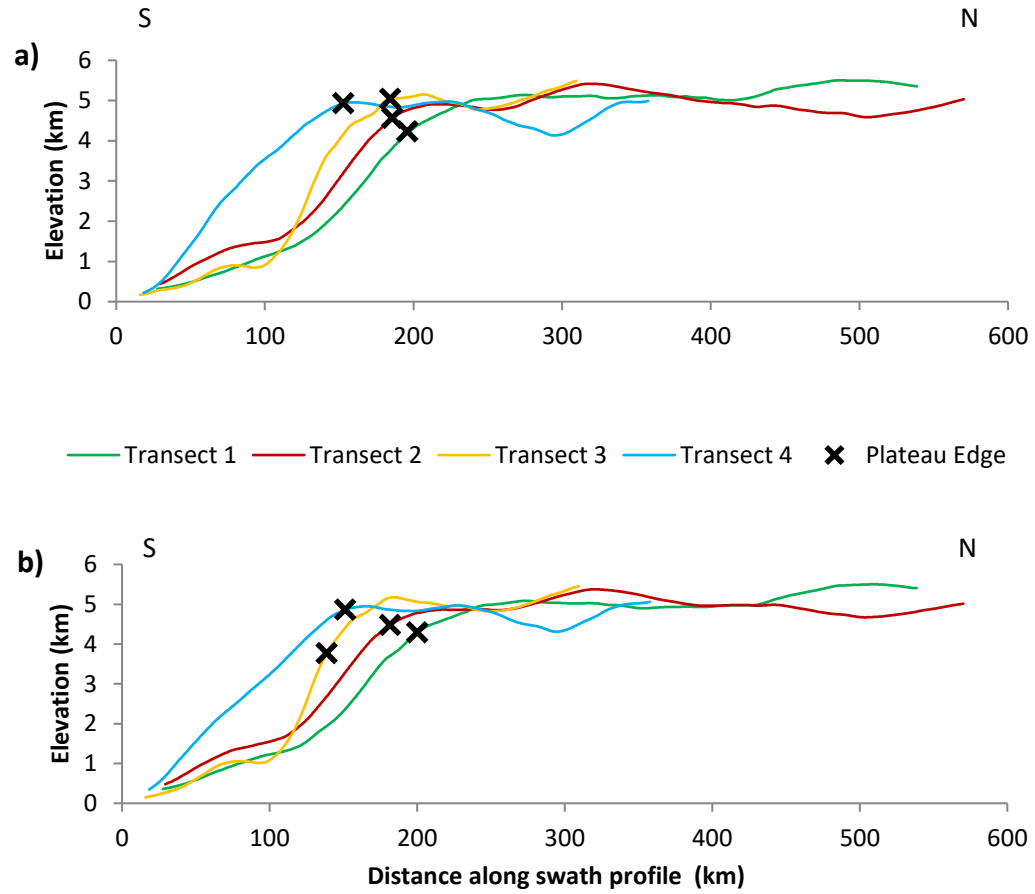

Figure 3.13: Average swath profiles taken along Transects 1-4 through the Himalayas with swath widths of a) 50 km and b) 100 km. Elevation is relative to mean sea level and the black 'X' represents the calculated plateau edge within each profile. Transect 3 shows significant offset between the plateau edge as defined in a) and b).

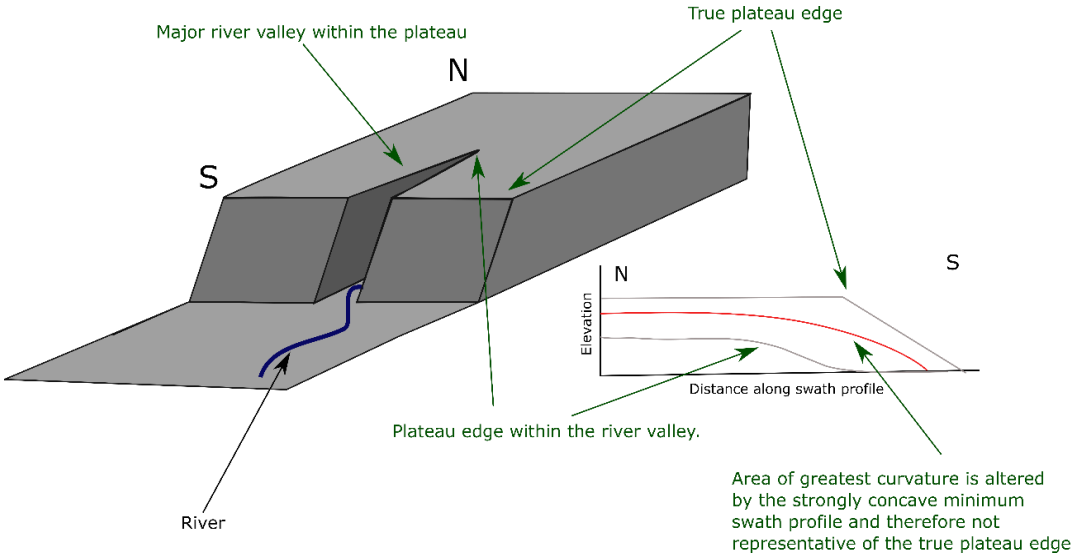

Figure 3.14: Hypothetical plateau and swath profile to demonstrate the effects of a major river on the plateau edge calculation.

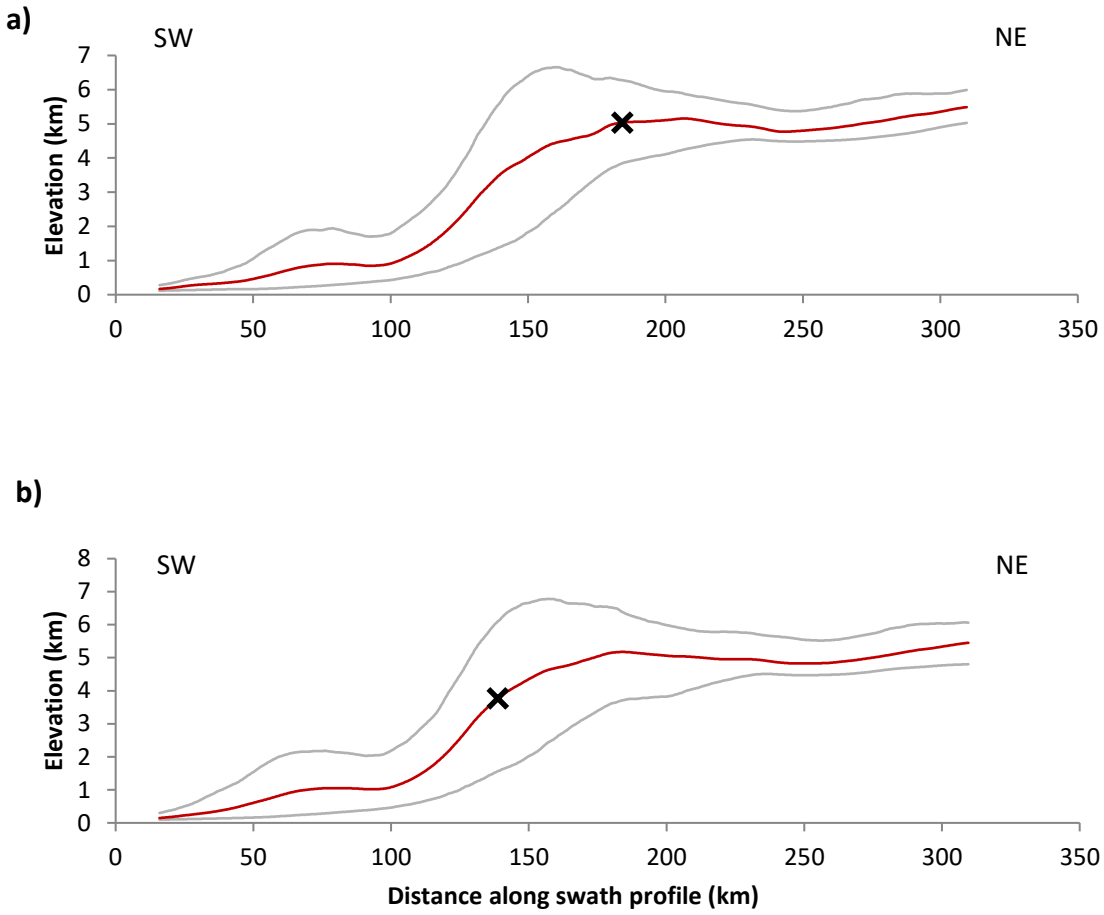

Figure 3.15: Swath profiles of a) 50 km and b) 100 km through Transect 3 in the Himalayas. The calculated plateau edge, indicated by the black 'X', can be seen to vary significantly between the two. The averaged topography is shown in red while the grey lines above and below represent the maximum and minimum profiles respectively. Elevation is given with respect to mean sea level.

It has previously been noted (Allen pers. comm.) that thrust events are rare above 3500 m in the Himalayas and other fold-and-thrust belts surrounding the Tibetan Plateau. Such a relationship was also seen within the thrusts extracted from the CMT catalogue in Chapter 2 (see Section 2.2.2). However, there is a poor relationship between the plateau edge and the 3500 m contour line within the data presented here. The calculated plateau edge instead appears to be at ~ 5000 m elevation. This suggests a poor relationship between the plateau edge and M $\geq$ 5 thrust earthquakes for this locality.

3.3.3 The Qilian Shan, Northern Tibetan Plateau

Swath profile widths of 100 km and 50 km were taken along the Qilian Shan deformation front. Profiles were taken at 50 km intervals in the west and 70 km intervals in the east, extending from the Qaidam basin to the northern deformation front. The location of each transect is shown in Figure 3.16. For all profiles, both the southern and northern plateau edges were analysed. Figure 3.17 presents the plateau edges of all profiles defined for both the north and the south of the range. In general, swath profile widths of 100 km showed more consistency in the location of the plateau edge, especially within the north. However, Transects 1, 2 and 7 were situated at the lateral extremities of the plateau and, therefore, their 100 km average swath profiles were skewed by the lower surrounding topography.

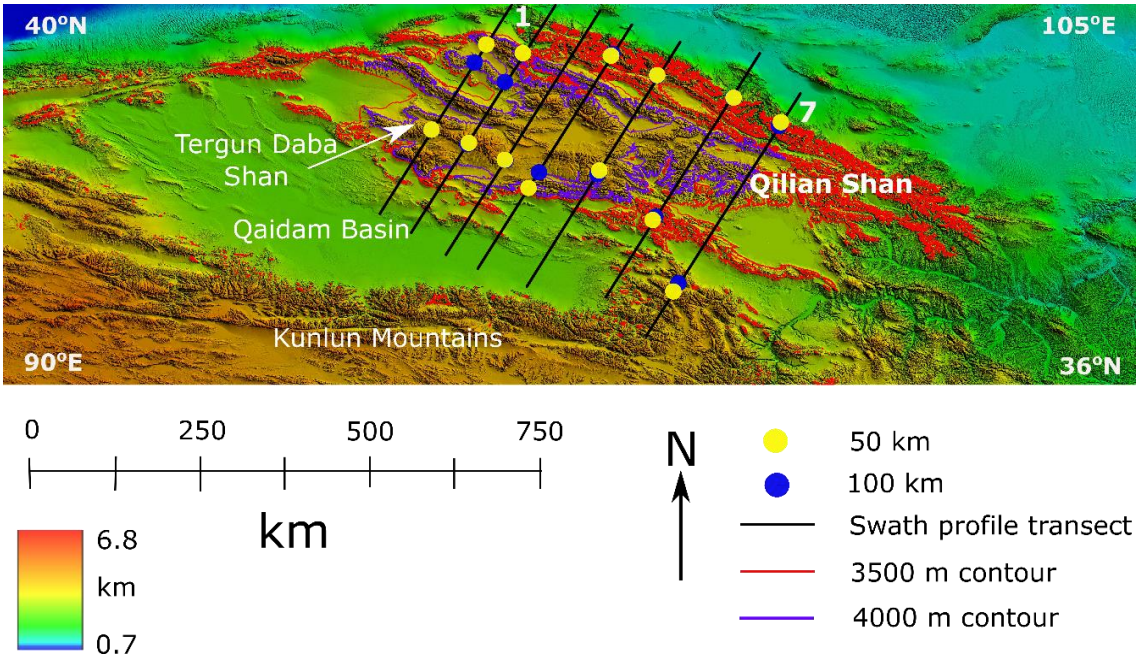

Figure 3.16: Location of the Transects and associated plateau edges within the Qilian Shan. Transects are numbered 1-7 from west to east. For all Transects both the north and the south plateau edge were calculated. Blue dots present the plateau edge as defined by the 100 km swath profile and yellow dots as defined by the 50 km swath profile. Where one dot appears to be absent it is a result of the exact locations of the plateau edge in the two different swath profiles overlapping. The 3500 m contour is shown in red and the 4000 m contour in purple. These two elevations were selected based on data presented in Chapter 2.

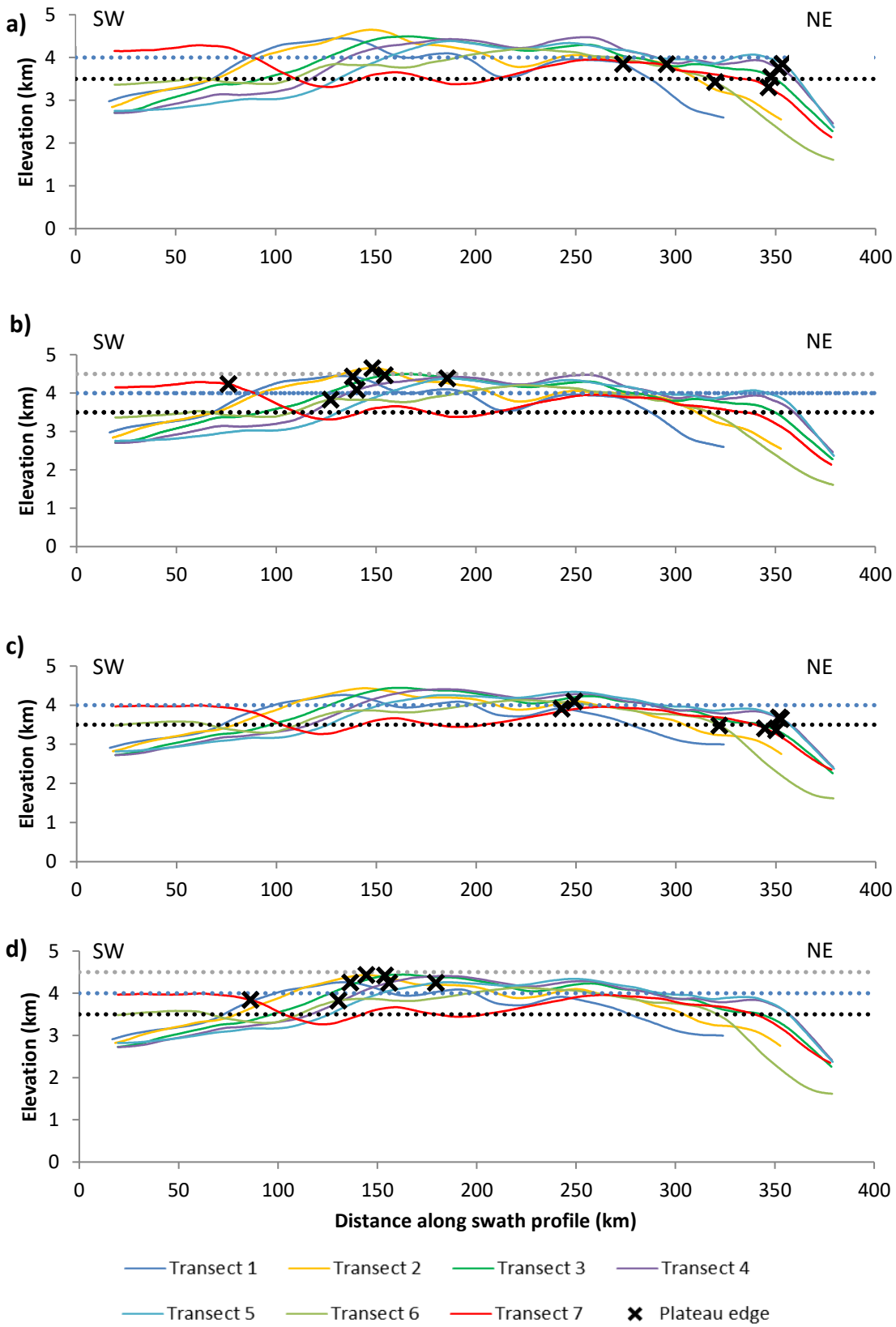

Figure 3.17: Topographic profiles for all Transects through the Qilian Shan. a) and b) show the northern and southern plateau edges taken from the 50 km swath profile while c) and d) show the northern and southern plateau edges taken from the 100 km profile. The data are taken from the average swath profiles smoothed to ± 50. The black 'X' within each graph represents the plateau edge as defined from the curvature graph. Elevation is given relative to mean sea level. The 3500 m contour (black dotted line) and the 4000 m contour (blue dotted line) are identified for reference. When examining the southern Qilian Shan the 4500 m contour (grey dotted line) is also shown.

Data from the small selected area in the Qilian Shan analysed in Chapter 2 (Section 2.2.3) showed a drastic cut-off in seismicity at ~ 4000 m elevation. The equivalent analysis of the nearby Himalayas presented a sharp cut-off in thrust earthquakes recorded in the CMT catalogue at ~3500 m (Section 2.2.2). The results presented here are discussed in relation to both these elevations. Initial analysis showed a poor correlation between the plateau edge and the 3500 m contour for both the 100 km and 50 km swath profiles in the south but a moderately strong correlation in the north. All the plateau edges within the north occur at elevations between 3500 m and 4000 m. Only Transects 1 and 2 presented significant plateau edge displacement. These profiles were subject to significant amounts of noise[3] within the curvature graph, making it difficult to identify a plateau edge with confidence. In addition, Transects 1 and 2 are situated at the edge of the plateau and as a result are subject to large variation at the extremities of each profile. Overall, there appears to be a strong link between the plateau edge in the north and the cut-off in $M \geq 5$ earthquakes.

The southern plateau edge, at 4500 m elevation, sat slightly higher than the previously observed cut-off in $M \geq 5$ thrust earthquakes (Section 2.2.3). In the west the peak in curvature correlates with a known thrust fault ridge, the Tergun Daba Shan (Chen et al. 2002). In addition, any relationship present appears to break down to the south-east, with the plateau sitting again on individual folds. In particular, the southern 'plateau edge' found via the curvature analysis on Transect 7 is in fact part of the Kunlun mountain range.

Within the inferred context of Williams et al.'s (1994) critical Coulomb wedge model, the plateau in the north should be associated with a reduction in large magnitude thrust earthquakes, but this is not seen. It is possible that the re-emergence of $M \geq 5$ earthquakes in the south of the Qilian Shan is explained by a second northward dipping detachment and associated critical wedge. However, it is more likely that the southern 'plateau edge' is instead a local anomaly associated with local faults rather than a regional correlation to the brittle-ductile transition within a critical Coulomb wedge.

[3] Noise refers to the appearance of peaks and troughs in the curvature graphs from local, rather than regional, trends.

3.3.4 The Longmen Shan, Eastern Tibetan Plateau

The Longmen Shan was not considered in Chapter 2. This was due to the area being too intersected by strike-slip and normal faults for the assumption of a purely thrust based dataset to hold true. However, it is possible to perform swath profile analysis of the Longmen Shan.

Four swath profiles taken along the plateau front (Figure 3.18), from SE to NW at 50 km intervals, were subject to curvature analysis in the same manner as described above. Due to a smaller geographical area, smaller profile widths of 20 km where chosen to replace the

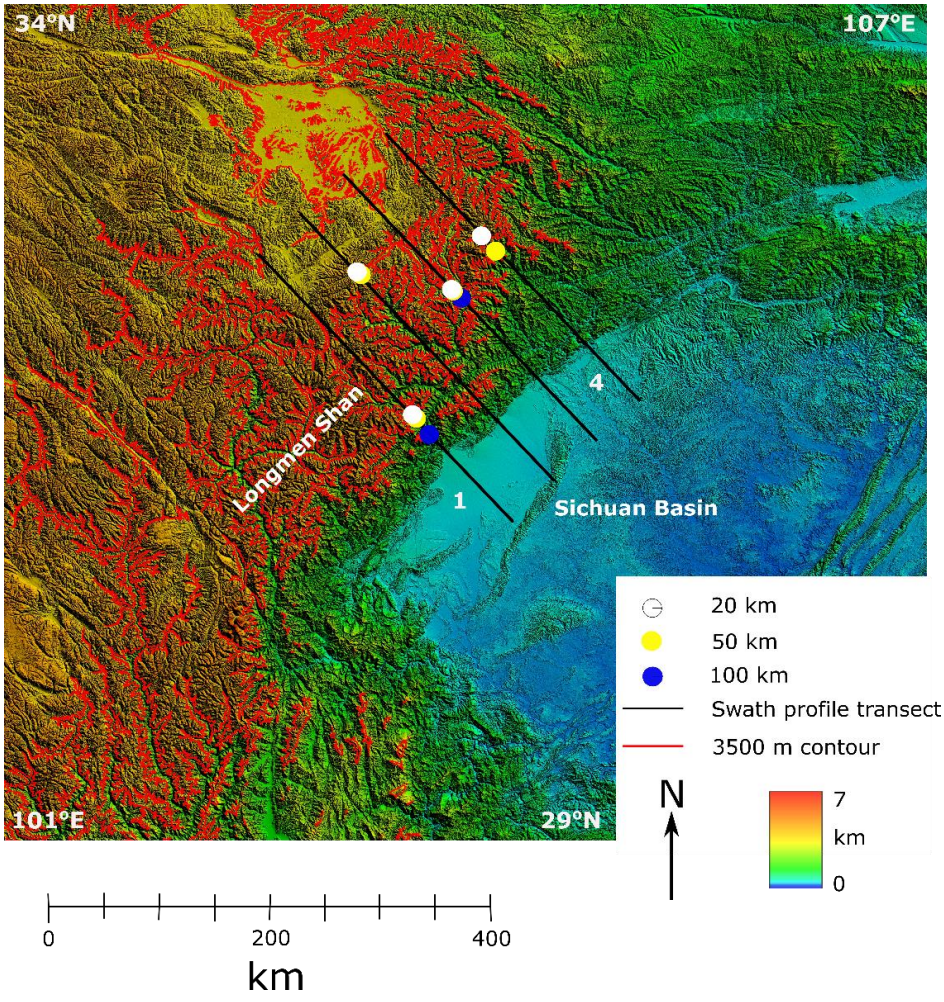

Figure 3.18: Location of the Transects and associated plateau edges within the Longmen Shan. Transects are numbered 1-4 from SW to NE. Blue dots present the plateau edge as defined by the 100 km swath profile, yellow dots as defined by the 50 km swath profile and white dotes as defined by the 10 km swath profile. Where dots appear to be absent this is because the exact locations of the plateau edge as defined by different swath profiles overlap. The red line represents the 3500 m contour found to be significant in other regions of the Tibetan Plateau.

100 km used for previous localities. For comparison purposes, 100 km swath widths were undertaken on Transects 1 and 3. Disparity in the location of the plateau edge occurred between the 20 km and 50 km swath profiles for Transect 4 and a slight offsets (7-20 km) for the three swath widths were seen for Transects 1 and 3.

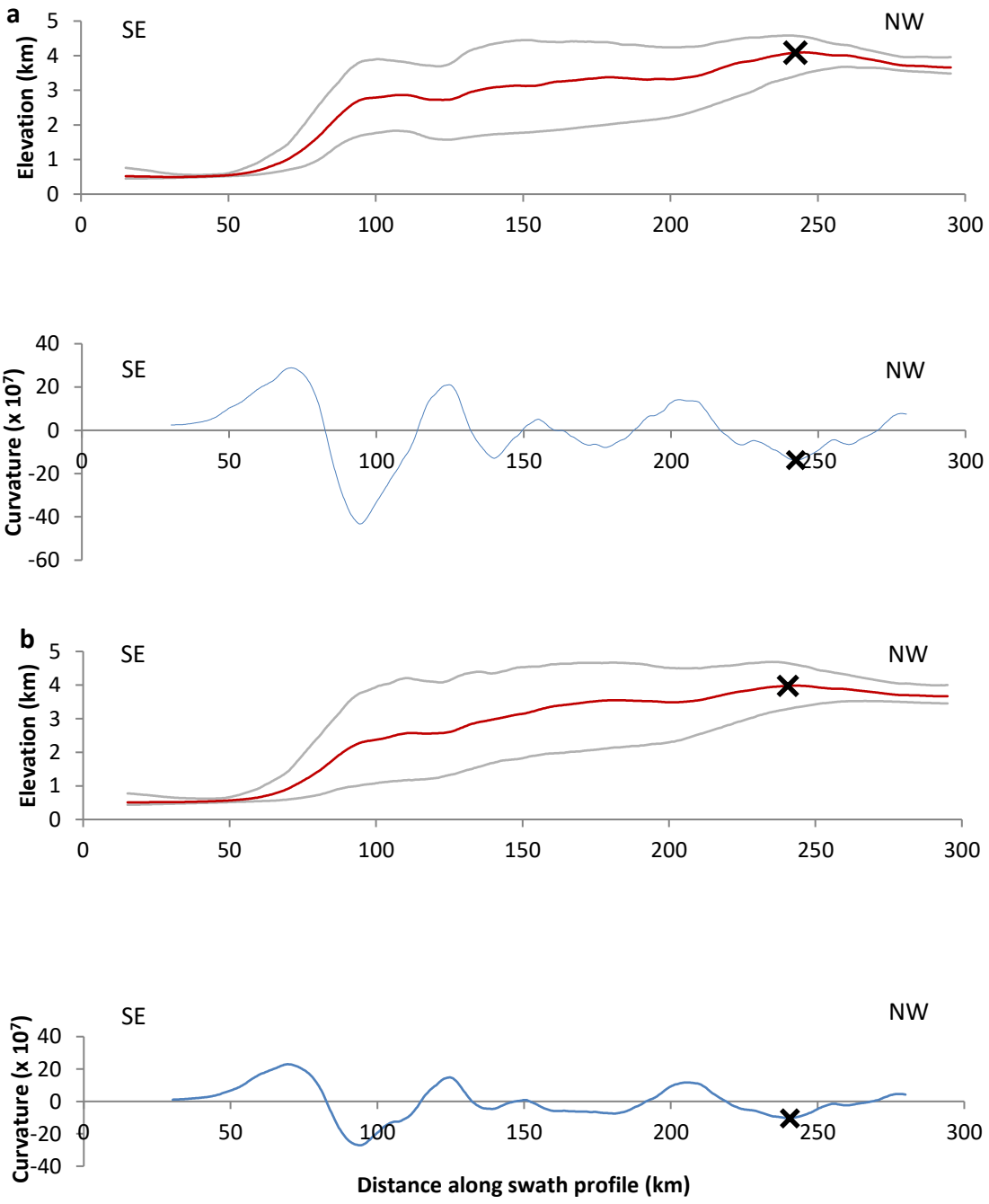

Figure 3.19: Swath profiles and curvature graphs of a) 50 km and b) 100 km through Transect 2 in the Longmen Shan. The calculated plateau edge, indicated by the black 'X', can be seen to vary significantly between the two. The averaged swath profile can be seen in red while the grey lines above and below represent the maximum and minimum profiles. Elevation is relative to mean sea level.

The plateau edge on Transect 2 appeared significantly out of kilter with the other three transects. The presence of an outcrop of strong crystalline basement in the SE, causing an irregularity within the original topographic profile, might have caused this discrepancy. However, this would be more likely to displace the plateau edge towards the SE rather than NW as is seen. An alternative explanation for the divergence would be Transect 2's proximity to two major rivers; the Mingjiang and Tuojiang (Lin et al. 2014). Indeed, most of the transect runs along either one of these two river profiles. Transect 2 is therefore removed due to these influences. The 20 km swath profile width associated with Transect 3 is small enough not to be significantly affected by the crystalline basement and is retained. However, the presence of this crystalline basement may explain the mismatch in the plateau edge between the different swath widths of Transect 3. The offset in Transect 4 can be explained by the curvature of the front.

After eliminating Transect 2 a moderately strong relationship is seen in Figure 3.20 between the plateau edge and the 3500 m contour line, found in other areas of the Tibetan Plateau to be the cut-off in $M \geq 5$ thrust earthquakes.

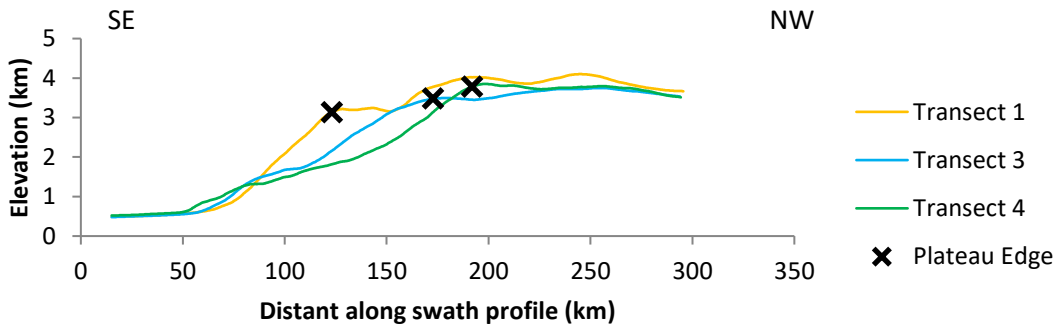

Figure 3.20: Plateau edges for the average 20 km swath profiles in the Longmen Shan. A running average of ±50 was used on the original topographic profiles and elevation is relative to mean sea level.

3.4 Discussion

3.4.1 Critical analysis of the method

The effectiveness of the method for identifying the plateau edge varied depending on the amount of noise within the curvature graphs. Some profiles presented a clear negative trough aligning with the edge of the plateau and as a result the exact location of the plateau edge could be identified with a high level of confidence. Other graphs contained large amounts of noise meaning it required additional information from the gradient graphs and topographic profiles before the plateau edge could be confidently located. Where gradients were shallow the plateau edge was harder to identify.

Noise may be the consequence of either too small a profile width or too low a smoothing value. Using larger profile widths risks analysis that no longer remains perpendicular to the deformation front (as illustrated in Figure 3.7). Using too narrow a profile width can introduce distortions due to local topographical features such as individual folds and river profiles. Higher smoothing values can affect the results by reducing the size of the dataset available for analysis. For example, in the Qilian Shan, editing the data to produce the curvature graph removed 10 % of the dataset. An element of compromise between dataset size and curvature noise is needed when implementing this method.

3.4.2 The relationship between plateau and seismicity

The relationship between the defined plateau edge and the limit of $M \geq 5$ thrust earthquakes varies between ranges. The Longmen Shan shows a strong correlation between the plateau edge contour and the cut-off altitude seen in other areas of the Tibetan plateau. A brittle-ductile critical Coulomb wedge could therefore be a good explanation in this locality. However, without analysis of the thrust earthquake vs elevation relationship within this specific region this cannot be confirmed.

A strong correlation is found in the north of the Qilian Shan but is absent in the south, supporting previous suggestions of a southward dipping decollement (Meyer et al. 1998;

Yin et al. 2008a). However, if this is the case, then the observed M ≥ 5 earthquakes in the south would not be predicted. This re-emergence of the M ≥ 5 earthquakes at the lower elevation appears more consistent with an earthquake system controlled by minimum work processes. If the area is underlain by two oppositely verging decollements, as has previously been suggested (Yin et al. 2008a; Yin et al. 2008b), then this could offer an alternative explanation for the re-emergence of large magnitude thrusts. The analysis of the curvature is, however, inconsistent with an additional decollement on the southern side.

In light of the evidence drawn from swath profiles it could be argued that the analysis presented in Chapter 2 on the Qilian Shan, which focused on a small area in the south, could have been on the 'wrong' side of the plateau to observe the cut-off in M ≥ 5 earthquakes associated with the wedge. The greater density of earthquakes in the south made it seem initially the more appropriate location for an in-depth study. Within the time constraints of this study returning to the data to analyse the northern side in the same manner was not possible.

From work presented in Chapter 2, the cut-offs in M ≥ 5 earthquakes in the Zagros and the Himalayas were found to be at 1250 m and 3500 m respectably. Within both localities the plateau edge sits at a higher elevation than this. From the analysis presented in this chapter, it is not clear what causes the fold-and-thrust belts within the Zagros and the Himalayas to rise without the aid of large magnitude thrust earthquakes. One possibility is that this disparity arises from some sensitivity in the method. In nearly all the profiles two changes in gradient were seen before a zero gradient plateau became established. Within the Himalayas, the maximum curvature occurred immediately prior to the onset of a zero gradient. In contrast, within the Longmen Shan and the Qilian Shan the maximum curvature is associated with an initial change in gradient after which the topography continues to rise. This suggests a period of deformation where the plateau continues to rise aseismically as represented schematically in Figure 3.21.

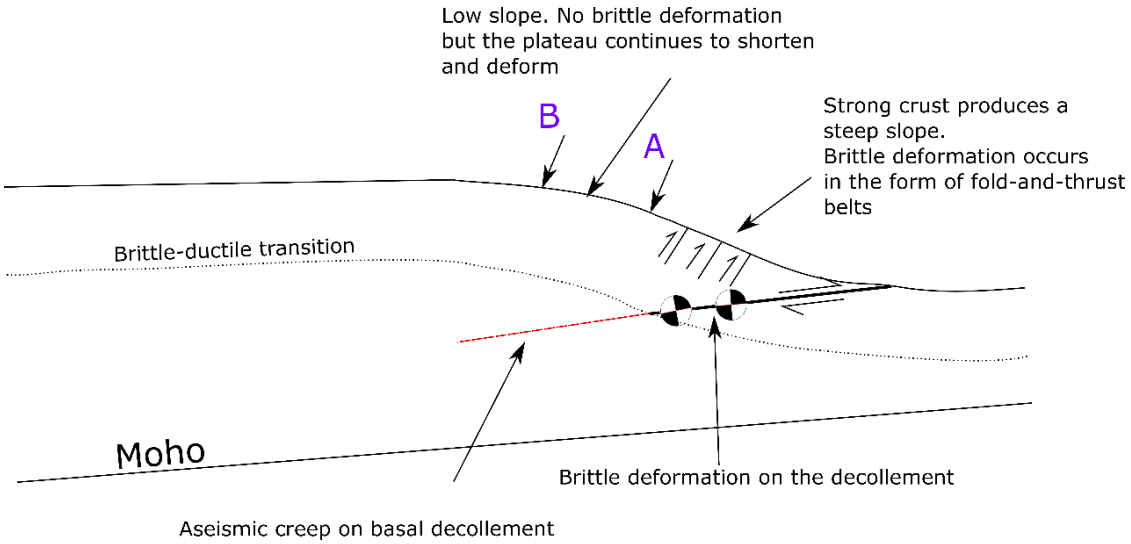

Figure 3.21: Schematic diagram representing the modified brittle-ductile critical Coulomb wedge developed in the present report. The diagram has been exaggerated vertically. 'A' refers to an initial change in gradient which has been found to be associated with the cut-off in M ≥ 5 earthquakes. 'B' refers to the true plateau edge where convergence ceases and a limiting elevation is reached.

The Zagros supports this theory. Within the Zagros the plateau edge varied between being located at, or above, the cut-off in M ≥ 5 thrust earthquakes. Where the plateau edge matched the seismicity cut-off the maximum curvature occurred at the initial change in gradient and the topography continued to rise after the plateau edge. Where the plateau edge sat above the seismicity cut-off the gradient dropped to zero beyond the plateau edge. Therefore, the inconsistency between the plateau edge and seismicity cut-off may simply be a result of the methodology. It is presently unclear why the curvature is greatest in some locations at the plateau edge and in others coincides with the onset of aseismicity. Further research and re-examination of the method is therefore required.

The fold-and-thrust belt geometries at the four localities presented in this study in all cases differ from that predicted by the Williams et al. (1994) model. In particular, Williams et al. (1994) predict a steepening gradient after the initial change in deformation mechanism whereas the opposite is seen. The assumption by Williams et al. (1994) of a two-step brittle-ductile transition driven entirely by temperature could explain their model's inconsistency with real localities. Retaining the basic premise that ductile deformation changes the geometry of the wedge, and based on the analysis presented here, a modified brittle-ductile coulomb wedge model has been developed (Figure 3.21). This model differs from that presented by

Williams et al. (1994) in that there is now a single brittle-ductile transition event after which energetic limitations become the dominant mechanism controlling the geometry. This contrasts with Williams et al's (1994) assumption of two distinct transitions, first in the lower wedge and then the decollement.

3.5 Conclusions

Plateau edges were quantitatively extracted from swath profiles. In the Longmen Shan and the Qilian Shan they provide evidence in support of a relationship between the plateau edge and the reduction in $M \geq 5$ earthquakes. However, in the Himalayas and the Zagros the plateau edge was found to sit consistently above the $M \geq 5$ earthquakes cut-off. It is proposed that this could be the result of a delimited zone, prior to the onset of a truly zero gradient, where the topography rises without large scale thrust earthquakes. The variation between the different localities is likely to result from variation of where the maximum curvature occurred.

Overall two conclusions can be drawn from the research presented within this chapter:

1. This study has developed a new method for defining the edge of a plateau. This quantitative approach agrees well with previous qualitative work, such as that of Duncan et al. (2003) in Nepal and Bhutan.
2. The relationship between the derived plateau edge and the limit of seismogenic thrusting varies between ranges, but is consistent with a region of high elevation aseismic crustal shortening before the final limit of crustal thickening and elevation is reached (Figure 3.21).

3.6 Future work

Many areas for further research have been identified in the course of the swath analysis. Those of particular interest are:

1. To carry out further analysis on the relationship between earthquakes and elevation for the northern sector of the Qilian Shan.
2. To examine whether the relationship presented in this data between $M \geq 5$ earthquakes and the plateau edge is observed within other fold-and-thrust belts.
3. To examine the relationship between climate and topographic gradient to ensure that variations in gradients are not merely a result of climate related geomorphological processes.
4. To explore how the strain rate varies in relation to the topographic profile, particularly how it relates to the formation of a zero gradient plateau.

Chapter 4

Rock mechanics experiments: the role of brittle vs ductile failure in controlling fault propagation

4. Rock mechanics experiments: the role of brittle vs ductile failure in controlling fault propagation

The following chapter explores the possible influence of a ductile sedimentary layer on the reduction in earthquake magnitude with elevation. Broadly speaking, two end-member formations are found layered within fold-and-thrust belts. Stronger, metamorphic or plutonic rocks of the crystalline basement are overlain by weaker sedimentary covers. A simplified version of this is seen in Figure 4.1, with the two end-members layered roughly horizontal in a simple succession.

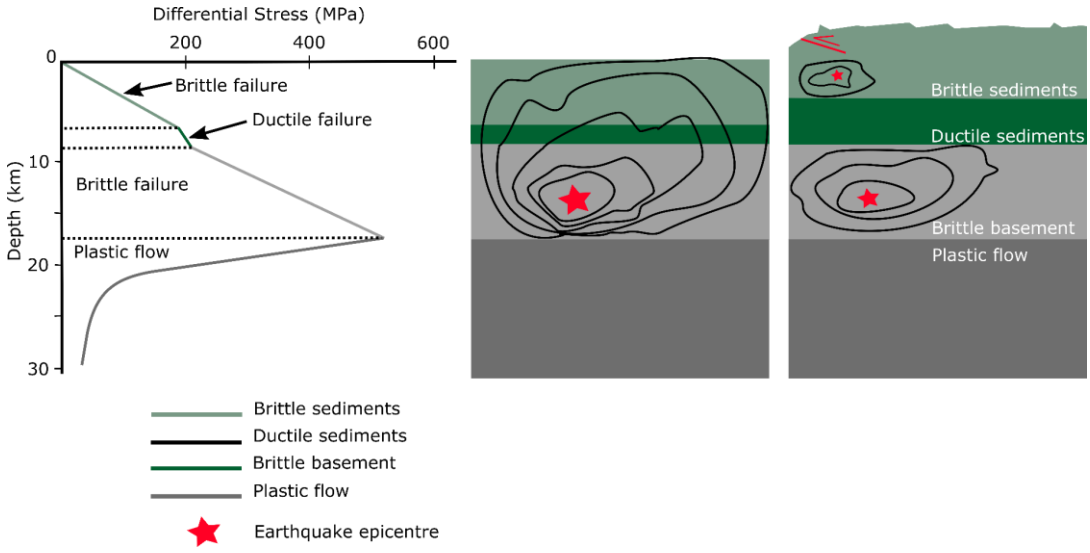

Figure 4.1: Schematic showing the effects of a thickened ductile layer within the sediments in a fold-and-thrust belt. Image on the left shows a depth vs. differential stress graph for the crust (Paola pers. comm.)

Such a crustal structure is applicable to the locations used within this study. For example, the Zagros consists of a crystalline basement overlain by a 10-15 km thick sedimentary cover of Phanerozoic carbonates and evaporites (Nissen et al. 2011). These two end-member rock types present significantly different rheologies under similar crustal conditions, with sediments being prone to ductile deformation at a lower pressure-temperature regime than metamorphic or plutonic rocks (Paterson & Wong 2005).

The aim, therefore, is to explore the third hypothesis put forward for the lack of high elevation thrust earthquakes. Such hypothesis is illustrated in Figure 4.1 and states that an

increase in plateau height creates a thicker zone of distributed deformation within a sedimentary layer which is able to suppress the propagation of large earthquakes originating in the brittle basement. The experimental investigation of this hypothesis is achieved through rock mechanics experiments performed in a triaxial loading apparatus. Subsequent microstructural observation showed how a propagating brittle fault reacts when it reaches a ductile medium. More specifically, the following questions are addressed:

1. Does the deformation become distributed within the ductile medium and if so how does it mature (is it gradual or abrupt)?
2. What can be learnt from the microstructural analysis of fault propagation into a ductile material?

Two lithologies were chosen to represent the end-member compositions for the deep upper crust and the overlaying sedimentary cover. In a first series of experiments, intact core samples of each lithology were loaded to failure for a range of pressure conditions (representing different depths) to characterise their brittle and ductile failure. Composite samples combining both lithologies were then deformed for the range of conditions that would favour brittle failure in the basement analogue and ductile failure in the sediment analogue.

4.1 Previous studies

In order to analyse the inhibiting effect of the propagation of a brittle fault into a ductile deforming medium, two lithologies were chosen which undergo the transition from brittle to ductile behaviour at different pressure-temperature (P-T) conditions. Here, ductile behaviour refers to a rock which is capable of undergoing substantial amounts of inelastic strain without macroscopic, localised fracture (Paterson & Wong 2005). Westerly Granite was chosen as an analogue for basement (brittle) rocks and an isotropic carbonate marble, similar to Carrara Marble, as an analogue for sedimentary (ductile) rocks. The origin of the marble sample is unknown and so descriptions were taken from a literature analysis of Carrara Marble and used as a guide. A description of the expected deformation mechanisms for the two studied lithologies follows. This allows any difference between the results of this study and previous studies to be identified. To facilitate comparisons, this literature review focuses on previous studies which deformed rocks under similar conditions to those available at Durham University.

4.1.1 Westerly Granite

4.1.1.1 Lithological description

Westerly Granite is a fine to medium grained, nearly isotropic rock, known to have low (~1 %) porosity (Mitchell & Faulkner 2008) and high strength (Haimson & Chang 2000). It is particularly favoured in experiments due to the high level of repeatability within its results (Lockner 1998). Young's modulus (E) and Poisson's ratio for the bulk behaviour of Westerly Granite vary within the literature but suggested values are 70 GPa and 0.2 respectively (Wong 1982). An approximation for the mineral composition is taken from Tullis & Yund (1977) and is as follows: 5-10 % biotite, 30 % quartz, 30 % oligoclase and 30 % microcline. Oligoclase shows patchy replacement by, for example, calcite and muscovite due to late stage igneous and hydrothermal alteration processes. Many healed and sealed fractures are present especially within quartz (Moore & Lockner 1995). Grain size is found to vary between 0.05-2.20 mm, with an average of 0.75 mm (Tullis & Yund 1977; Moore & Lockner 1995).

Microcracks tend to be smaller than this average grain size (Moore & Lockner 1995). Many grains contain distinctive undulose extinction (Tullis & Yund 1977).

4.1.1.2 Modes of failure

Lockner's 1998 paper, which describes an experimental set up similar to that used in Durham University's laboratory, provides a good comparison for the work described here. He conducted experiments at room temperature on a 25.4 mm wide and 63.5 mm long sample encased in a polyurethane jacket. Samples were deformed under dry conditions at confining pressures of 50, 100, 150 and 200 MPa. Two shortening rates were applied: 1 μms^{-1} (strain rate 1.57 $x10^{-5}$ s^{-1}) and 0.01 μms^{-1} (strain rate 1.57 $x10^{-7}$ s^{-1}). The results from Lockner (1998) are presented in Figure 4.2 and indicate, via an abrupt stress-drop, that brittle behaviour within granite is persistent at confining pressures of up to 200 MPa.

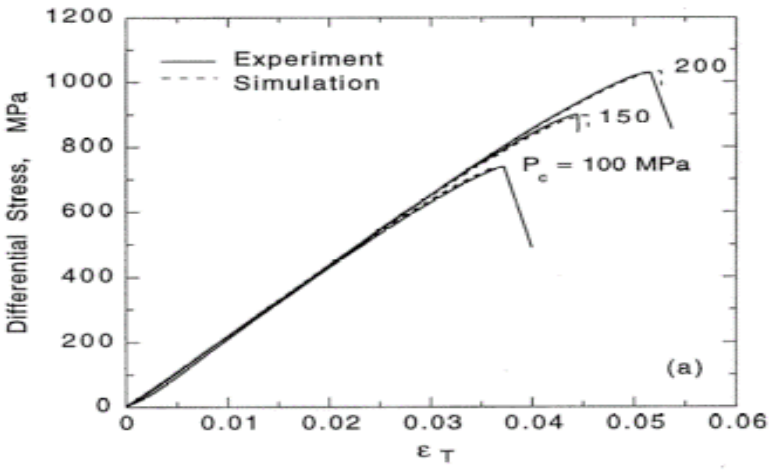

Figure 4.2: Differential stress (MPa) plotted against total strain for Westerly Granite under a variety of confining pressures. Experiments were conducted at a strain rate of 1.57 x 10^{-5} s^{-1}. The dotted line represents modelled stimulations which are not relevant to the analysis within this report. Samples underwent a small amount of stable unloading following peak stress; this then progressed into dynamic unloading and an abrupt stress drop (Lockner 1998).

4.1.1.3 Microstructural description of Westerly Granite at failure

Microstructural analysis was undertaken by Tullis & Yund (1977) using experiments which deformed Westerly Granite in dry conditions at a constant strain rate of 10^{-6} s^{-1}. Confining pressures of 150 – 1500 MPa were reached for temperatures between 25 ^{o}C and

1000 ºC. Samples were taken to between 9 % and 58 % shortening. Deformation at lower confining pressures (< 500 MPa) consisted of microcracks in the rock that linked up forming one main through-going fault after very low strains. A few minor parallel and conjugate fracture zones did develop but contained negligible offsets. Fault gouge was observed to be common on the main fault (Tullis & Yund 1977).

The density of microcracks doubles when compared to undeformed sections in the far-field area of the sample and increases exponentially towards the fault, with greatest densities found within the process zone (Moore & Lockner 1995). The process zone refers to the weakened area directly in front of the tip of a propagating localised fault. The increase in crack density is uniform across different minerals.

4.1.2 Carrara Marble

4.1.2.1 Lithological description

Carrara Marble is favoured among experimentalists due to its isotropic nature and extreme purity, with samples typically containing ~ 98 % calcite (Pieri et al. 2001). Grain size varies in the range 0.5-2.0 mm (Wong & Einstein 2009) with an average size of 1.6 mm (Zhang et al. 1994). Representative values of the Young's modulus (E) and Poisson's ratio for the bulk behaviour of marble are 50-70 MPa and 0.06-0.25 respectively (Fossen 2010). The marble used for this study is isotropic, has a composition of ~ 100 % calcite and an average grain size of 0.5-5.5 mm (see Section 4.4.1). It is considered, therefore, that it will behave in a similar manner to Carrara Marble.

A calcite-rich rock is particularly relevant for the experiments reported here due to its behaviour at room temperature being comparable to ductile materials such as quartz and feldspar at 300 ºC (Schubnel et al. 2006). The marble used for this study is thus a good analogue for the behaviour of ductile materials at the base of the seismogenic zone where it has been previously suggested that large earthquakes tend to nucleate (Das & Scholz 1983).

4.1.2.2 Modes of failure

This literature review considered reports of triaxial experiments conducted at room temperature. Schubnel et al. (2006) deformed samples measuring 80 mm in length and 40 mm in diameter using a strain rate of ~ 0.33 x $10^{-6}s^{-1}$. They concluded that below 50 MPa confining pressure, the deformation of the rock is brittle. At confining pressures greater than 50 MPa the sample experiences homogenous strain deformation in the form of cataclastic flow and strain hardening occurs.

Fredrich et al (1989) deformed a 38.10 mm by 15.88 mm sample at a strain rate of $10^{-5}\,s^{-1}$ to a maximum axial strain of less than 6 %. Figure 4.3 displays the stress-strain data from this study and identifies that at low confining pressures of 5-10 MPa samples would localise strain, whereas confining pressures of 30-450 MPa presented evidence for work hardening. This implies a lower confining pressure for the brittle-ductile transition compared with that of Schubnel et al. (2006).

Lower strain rates are associated with a lower confining pressure for the brittle-ductile transition (Serdengecti & Boozer 1961). This is contradictory to what has just been described, with the slower strain rate connected to Schubnel et al.'s (2006) study maintaining brittle behaviour to a higher confining pressure (50 MPa) than Fredrich et al (1989). Other factors within the experimental set up must account for the difference in confining pressure associated with the brittle-ductile transition.

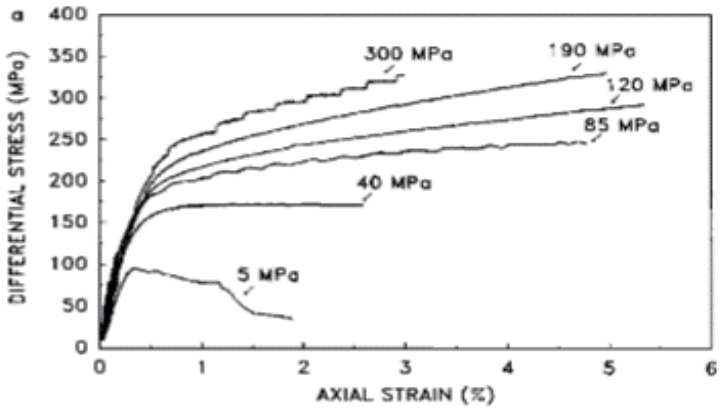

Figure 4.3: Axial strain (%) plotted against differential stress (MPa) for Carrara Marble under a variety of different confining pressures (Fredrich et al. 1989).

4.1.2.3 Microstructural description of Carrara Marble at failure

This review assessed two cases regarding the Carrara Marble; 1) an experimental study by Fredrich et al. (1989), for which the conditions have been described in Section 4.1.2.2, and 2) work by Zhang et al. (1994) who deformed a 21 mm long and 10 mm wide sample at a constant strain rate of $1.2 \times 10^{-4}\ s^{-1}$ at room temperature under various confining pressures.

At 5 MPa confining pressure and low strains of 1.0-1.5 % the marble showed brittle failure as macroscopic localised deformation associated with a large stress-drop was observed. Cracks occur intragranularly, transgranularly (typically across three or four grains), and intergranularly along grain boundaries. A large number of the cracks align parallel to σ_1. Mechanical twinning was occasionally present but had no association with the microcracks (Fredrich et al. 1989). With increased strain, strain localisation occurred along shear bands inclined at 30^o to the maximum shortening direction. These bands consist of fragmented anastomosing networks of grain boundary and transgranular cracking.

At confining pressures as low as 50 MPa the marble behaves in a semi-brittle manner, with microstructural plasticity occurring while a degree of heterogeneity is maintained to even an intragranular scale. As observed in the brittle field, microcracking occurs predominantly in the direction subparallel to σ_1. Differently from the brittle field, intergranular fractures are absent. At the microscale, there is evidence of dislocation glide (Fredrich et al. 1989) in the form of a small number of bent twins (Zhang et al. 1994). Other deformation mechanisms include simultaneous microcracking and deformation twinning. Mechanisms of deformation twinning and lattice bending are well developed, especially at higher strains (Zhang et al. 1994).

4.1.3 Summary of modes of failure in Westerly Granite and Carrara Marble

Based on previous studies (Tullis & Yund 1977; Fredrich et al. 1989; Moore & Lockner 1995; Schubnel et al. 2006), brittle deformation is expected to be observed within the Carrara Marble at confining pressures of 5-10 MPa and ductile deformation at 40-50 MPa. At intermediate confining pressures mixed brittle/ductile behaviour was reported with a variable amount of ductile deformation preceding the onset of localised, brittle failure. For both these confining pressure ranges, the granite remains within the brittle regime. Single lithology experiments were conducted within the marble over the confining pressure range of 5 -35 MPa to identify the brittle-ductile transition.

4.2 Experimental methodology and set-up

4.2.1 Sample preparation

For each lithology, samples were cored from a single block in the same direction and then flat ground using a cylindrical grinder to ensure perfectly square ends. The Westerly Granite sample is sourced from Rhode Island (USA). The marble sample was obtained from a local source, but the exact location of the original rock is unknown.

Data inaccuracies can occur due to edge effects. This arises from the mismatch in the elastic properties of the rock and the steel end plates of the triaxial machine. Such a mismatch of elastic properties causes a complex zone of triaxial compression at the end of the sample, which in shorter specimens can dominate the stress field and thereby alter the mechanical behaviour of the entire sample. As a general rule, samples with an aspect ratio[4] of greater than 2.5 are considered to be appropriate (Hudson & Harrison 2000).

For these reasons, the ratio of sample length (L) to diameter (D) was kept at 5:2 for all the single lithology experiments. Within the composite experiments, individual sections of granite and marble had a lower L:D ratio than the recommended 5:2, but the overall length of the two lithologies combined exceeded it. This is comparable to the L:D ratios used within experimental studies reported in the literature (Section 4.1) and is large enough to obviate stress perturbations at the edge of the samples. Samples were encased in a 2.5 mm thick PVC jacket. The softness of the PVC meant the data did not need to be corrected for the jacket's strength.

4.2.2 Experimental apparatus

Experiments were undertaken in a high-pressure, triaxial compression apparatus ($\sigma_2 = \sigma_3$) using low viscosity silicone oil as a confining medium (Figure 4.4). The oil pressure was increased using an air driven intensifier, thus increasing the confining pressure on the sample. The axial force was applied by a 250 kN servo-controlled loading system at a constant load point displacement rate of 1 μms^{-1}, corresponding to about $2 \times 10^{-5} s^{-1}$ strain rate. A high

[4]Aspect ratio refers to the length divided by the width of the sample.

sensitivity internal force gauge (± 0.5 kN) recorded the axial force on the sample. Experiments were corrected for machine stiffness. The stiffness value of the machine has been measured as 180 $kNmm^{-1}$. The experiments were not corrected for the stiffness of the steel spacers due to the modulus of steel being much greater than that of the sample rocks (~200 GPa compared to~50 GPa).

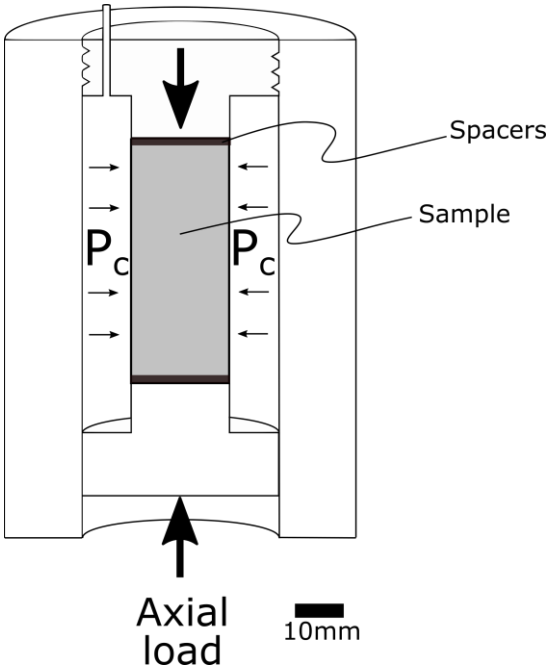

Figure 4.4: Schematic diagram presenting the arrangement of the sample assembly in the deformation apparatus. Image is taken from an analysis of a comparable experiment (Harbord pers. comm.).

4.2.3 Experimental conditions and settings

All experiments were conducted at a constant strain rate of 2 x 10^{-5} s^{-1}, well above the lower limit strain rate of 10^{-10} s^{-1} suggested by Lockner (1995). Due to the lack of servo-control in the confining pressure system, a constant confining pressure could not be maintained and, as a result, the confining pressure tends to increase marginally (by ≤ 5 MPa) as the experiment progresses.

Figure 4.5: Marble within the experimental apparatus prior to running Experiment 1. The coin is present for scale.

Preliminary experiments using a single lithology sample were conducted on cores of Westerly Granite and marble in order to investigate the brittle-ductile transition within each. Table 4.1 indicates the parameters used for each experiment.

The marble experiments (Experiments 1-3 – Table 4.1) were confined to pressures of 5 MPa, 10 MPa and 35 MPa based on the brittle-ductile transition reported in the literature (Fredrich et al. 1989; Schubnel et al. 2006 - Section 4.1.2). Figure 4.5 shows an image of the experimental sample assembly containing a marble core prior to deformation. Once the confining pressure at which marble will deform in a ductile manner was established (Experiments 1-3), the granite was deformed under similar conditions (Experiments 4 & 5) to ensure that the samples behaved in a brittle manner. Experiment 5 was continued post failure to ascertain if stick-slip behaviour would be generated on the fault.

Table 4.1: Parameters for Experiments 1-5

Experiment No.	Experiment 1	Experiment 2	Experiment 3	Experiment 4	Experiment 5
Sample Lithology	Marble	Marble	Marble	Granite	Granite
Confining Pressure (MPa)	5	10	35	10	35
L:D ratio (mm)	50:21	51:21	51:21	51:21	48:21

4.3 Results of single lithology experiments

The results of the single lithology experiments were a necessary prerequisite of the composite experiments. As such, the results from these experiments are now presented.

4.3.1 Marble experiments

The results of the experiments preformed on marble have been plotted on a stress vs strain diagram (Figure 4.6) and are discussed for each experiment below together with observations taken from the deformed samples recovered after the experiments (Figure 4.7).

Experiment 1: 5 MPa

Deformation at 5 MPa confining pressure presented purely brittle behaviour, with a phase of weakening preceding a sudden stress-drop after ~ 0.5 % of axial strain (Figure 4.6). The variation in the post-peak failure - alternating between steeply dipping sections of the graph and flatter 'ledges' - has, in previous studies, been correlated to different stages within the failure and localisation process (Paterson & Wong 2005). The sample showed macroscopic localisation in the form of a conjugate set of faults (Figure 4.7) dipping at 32^{o} with respect to the principal stress (σ_1).

Experiment 2: 10 MPa

Failure at 10 MPa confining pressure occurred over a long period of slow weakening, initiating at ~ 0.7 % axial strain, followed by a slow stress drop after ~ 2.4 % axial strain. This is shown as the orange line on Figure 4.6. Inflections associated with failure within a purely brittle axial stress vs axial strain graph are known to become less sharp as the brittle-ductile transition is approached. Therefore, the long period of slow weakening could represent an approach to the brittle-ductile transition (Paterson & Wong 2005). Alternatively, this slow weakening could be the result of ductile behaviour, followed by a stress drop associated with brittle localisation, representing a hybrid semi-brittle behaviour within the marble. Slow failure has previously been associated with silent earthquakes (Brantut et al. 2011) and, therefore, the

localisation within the marble at 10 MPa could be aseismic. The macroscopic manifestation of faulting occurred along a localised set of conjugate faults (Figure 4.7) dipping at ~ 33° to σ_1.

Experiment 3: 35 MPa

At 35 MPa confining pressure no stress drop was observed. This is shown by the blue line in Figure 4.6 which presents a positive gradient indicating strain hardening behaviour. The sample failed in a ductile manner after ~ 0.8 % of axial strain. Shear bands developed at ~ 45 ° to σ_1 (Figure 4.7).

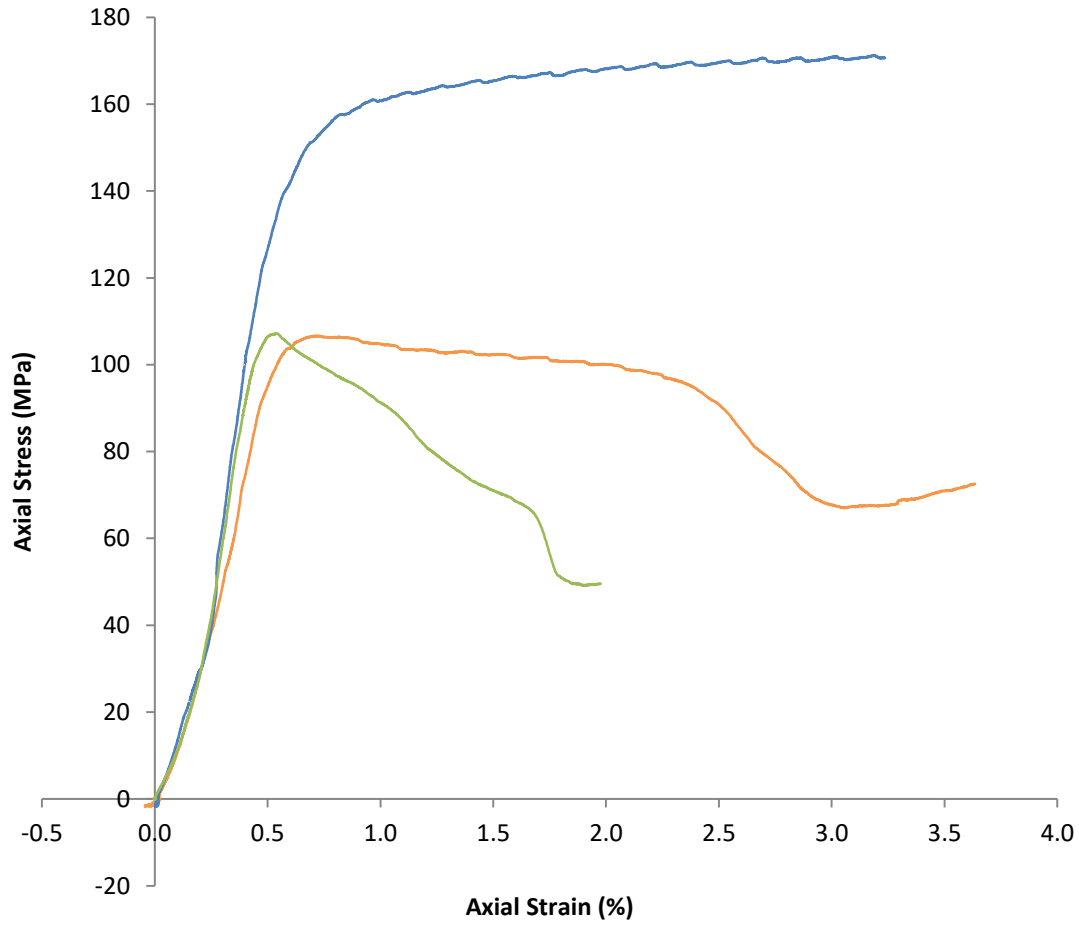

Figure 4.6: Axial stress (MPa) vs axial strain (%) graph for Experiments 1-3. The experiments are colour coded as follows: Experiment 1 - green; Experiment 2 - orange and Experiment 3 - blue. The starting point of each experiment was taken as the point axial strain became positive. The data is corrected for machine stiffness.

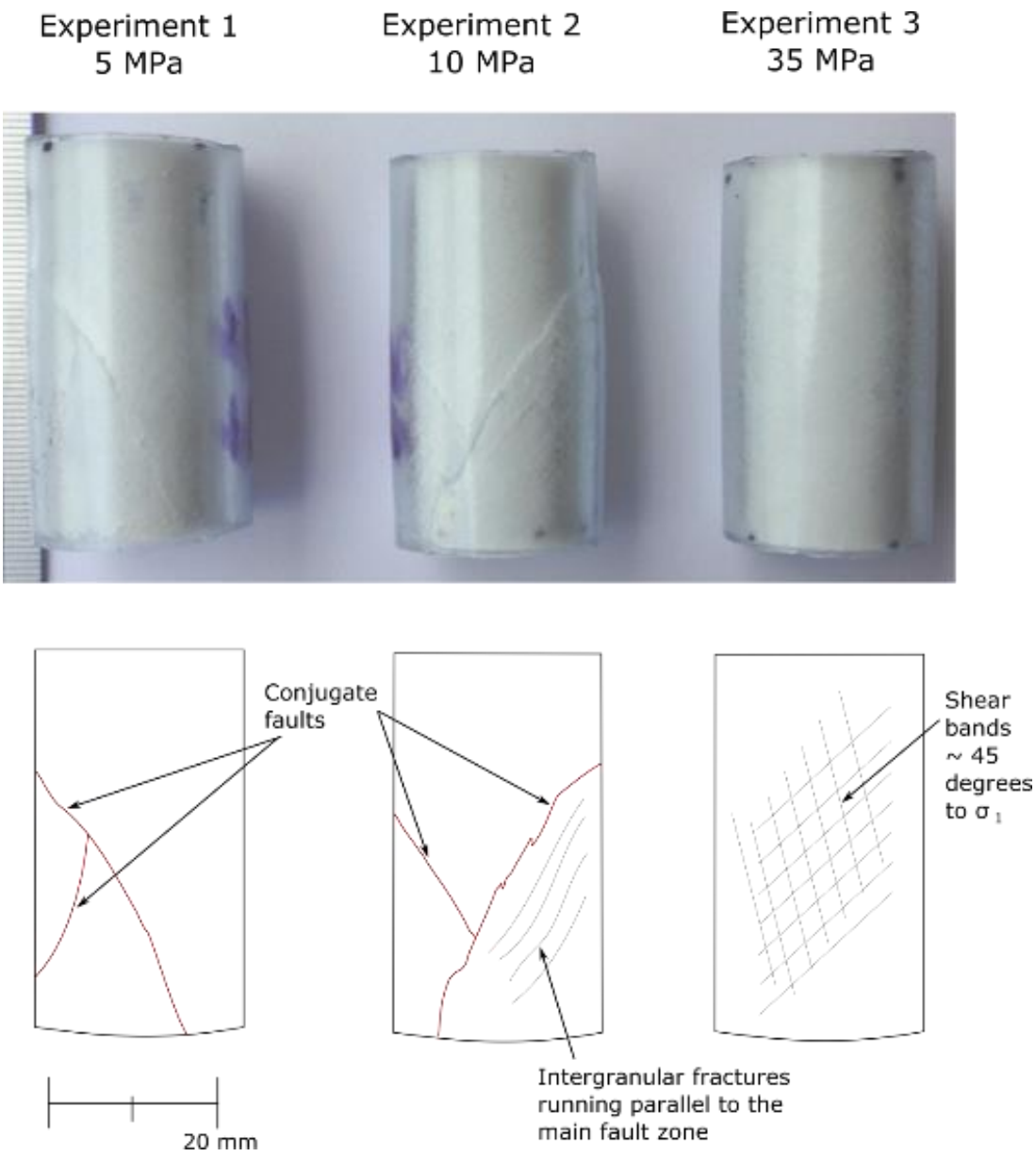

Figure 4.7: Experiments 1-3 after deformation. From left to right the change of deformation is seen as the confining pressure increases from 5 MPa to 10 MPa and then 35 MPa. Schematics are seen below the corresponding cores.

Summary of preliminary marble experiments (Experiments 1-3)

The results of Experiments 1 – 3 indicated a brittle-ductile transition for the marble at soon after 10 MPa confining pressure, similar to the results of the Fredrich et al. (1989) study. As expected, brittle deformation took the form of a set of conjugate faults which in both Experiments 1 & 2 occurred at an angle of ~ 32° to σ_1, again comparable to that found from the literature study of Carrara Marble (Section 4.1.2). Higher confining pressures required greater strains to be achieved before failure. This implies, as is expected, that the sample strengthened

with increasing confining pressure. The Young's moduli from Experiments 1 – 3 were: 26, 32 and 37 GPa respectively. These values are slightly lower than that predicted for marble by Fossen (2010) but are broadly similar to that approximated from the data presented in Fredrich et al.'s (1989) work (Figure 4.3) which suggests a Young's modulus of ~ 40 GPa.

4.3.2 Westerly Granite experiments

The experiments performed on Westerly Granite samples indicated purely brittle behaviour at confining pressures of both 10 MPa and 35 MPa, with sudden stress drops occurring at 1.0 % and 1.2 % axial strain, respectively, soon after yielding of the samples (Figure 4.8). Young's moduli for Experiments 4 & 5 were 51 and 60 GPa respectively. In both samples a pair of conjugate faults formed (Figure 4.9) which accords with observations from previous studies (Tullis & Yund 1977).

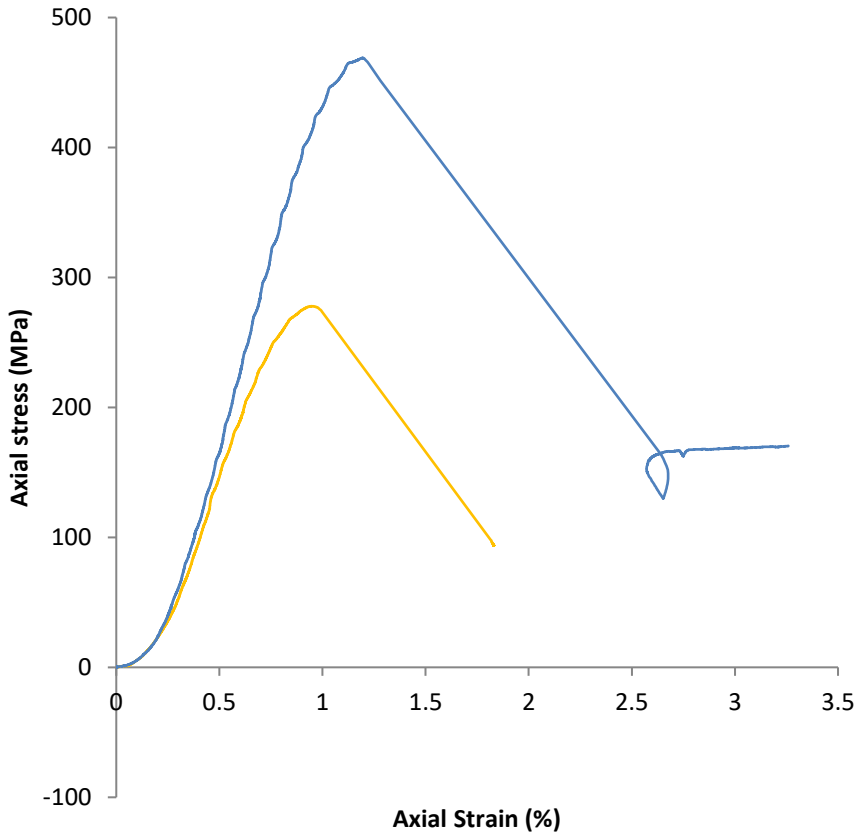

Figure 4.8: Axial stress (MPa) vs axial strain (%) graphs for Experiments 4 and 5. The experiments are colour coded to match those deformed at the same confining pressure in Figure 4.6, with Experiment 4 in orange (10 MPa confining pressure) and Experiment 5 in blue (35 MPa confining pressure). The graph has been corrected for machine stiffness.

Experiment 4: 10 MPa

The experiment conducted on a Westerly Granite sample at 10 MPa confining pressure was carried out with the intention of forming the through going fault required for the second composite experiment (Experiment 7). In order to preserve the fracture the experiment was stopped as soon as the sample failed and was not tested for subsequent stick-slip behaviour on the newly created fault.

Experiment 5: 35 MPa

The 35 MPa confining pressure granite experiment was stopped soon after failure and then restarted to see if any healing or stick-slip behaviour occurred on the fault surface. No stick-slip behaviour was generated once the experiment was restarted but stable sliding occurred. An increase in the axial force was necessary to load and shear the sample after the experiment, indicating that a small amount of healing occurred on the fault surface.

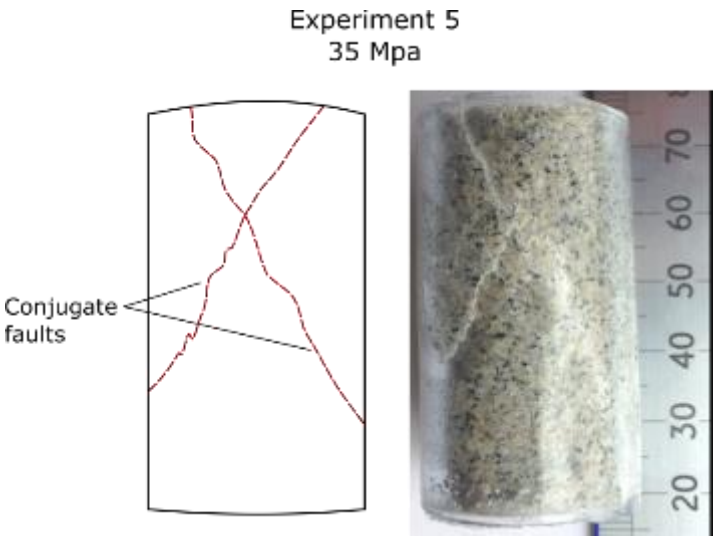

Figure 4.9: Brittle deformation localised on a set of conjugate faults within Experiment 5 (35 MPa confining pressure)

4.4 Composite experiments – dual lithology

4.4.1 Specific experimental set up

Based on the preliminary results for the pure marble and Westerly Granite lithologies, a set of composite experiments was designed applying confining pressures at which the granite was observed to deform in a brittle manner and the marble in a ductile one during the preliminary experiments (Figures 4.6 and 4.8). The hybrid brittle-ductile behaviour in the marble at 10 MPa suggests that anywhere between 10 - 35 MPa it would be deforming in the ductile regime. Figure 4.10 shows the sample assembly set-up used within the composite experiments. Cores were produced in the same manner as those for the single lithology experiments.

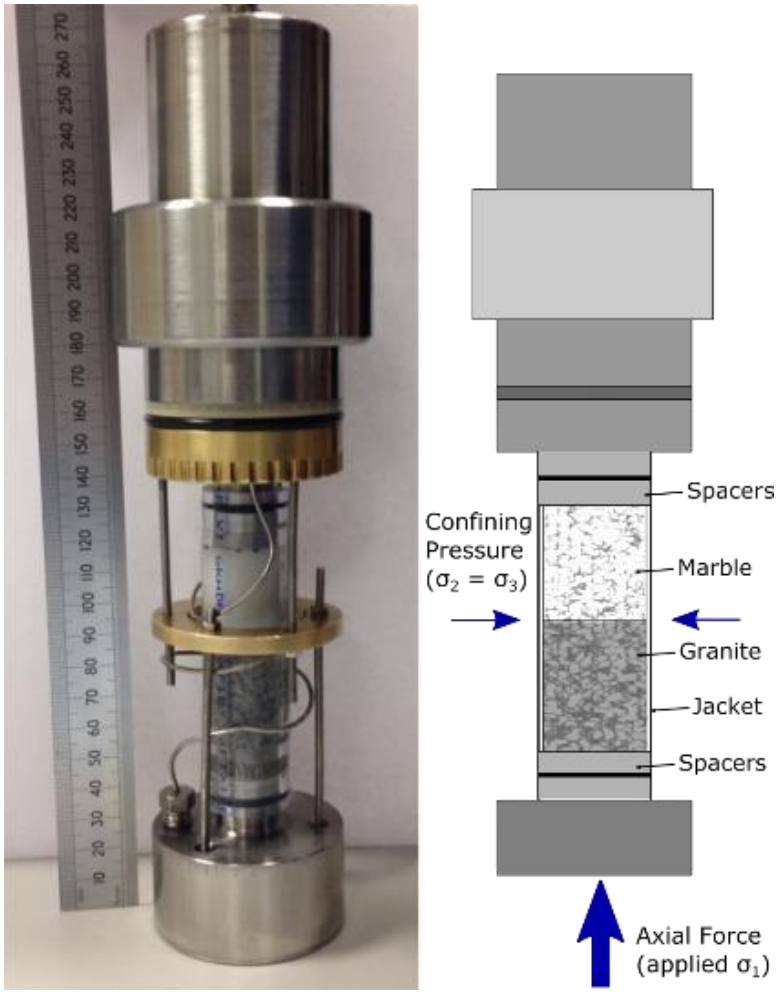

Figure 4.10: Marble and granite within the experimental apparatus prior to running Experiment 6. The ruler, present for scale, shows cms.

Two composite experiments were undertaken with the parameters outlined in Table 4.2. Different experiments were run to assess the effect of an un-deformed sample (Experiment 6) and a pre-deformed sample (Experiment 7).

Table 4.2: Parameters for Experiments 6 and 7

Experiment No.	Experiment 6	Experiment 7
Lithology	Composite	Composite
Confining pressure (MPa)	30	35
Marble L:D ratio	30:21	26:21
Granite L:D ratio	31:21	31:21
Overall sample L:D ratio	61:21	57:21

Experiment 6

Experiment 6 used un-deformed marble and un-deformed granite which were jacketed with a combined length of 61.14 mm. The confining pressure of the experiment was 30 MPa, chosen on the basis of Experiments 1-5 to ensure the marble would be deforming in a purely ductile manner and the granite in a brittle one.

Experiment 7

Experiment 7 used a faulted sample of granite (deformed in Experiment 4, Pc = 10 MPa) and an undeformed section of marble of total length 57.16 mm. A combined experiment involving a pre faulted granite core was investigated for two reasons. Firstly, it was believed that should the experiment consist of two undeformed cores, the weaker marble would fail before the peak stress required for failure in the granite was reached, hence concentrating deformation in the marble. This was seen to occur in Experiment 6. The overarching aim of this chapter is to investigate the propagation of a brittle fault into a ductile medium, thus, in order to enable brittle failure in the granite it must first be weakened with a pre-existing fracture. Secondly, large faults occur on pre-existing structures and examining the behaviour of a reactivated fault is a better analogue for real geological situations.

The fractured granite sample was cut to centre the fault surface at the interface between the marble and the granite. Half the sample remained within the jacket during the cutting

processes in order to keep the fault together (Figure 4.11). After this, the granite was transferred into a new jacket and an un-deformed piece of marble was added (Figure 4.12).

Fragments of the fault gouge from the fractured section of granite were lost during sample preparation due to the use of water when cutting the sample. Further loss was encountered during the transfer of the sample from one jacket to another. The exact implication of the loss of gouge is difficult to ascertain due to the effects of gouge on a rock's ability to stick-slip being unknown (Paterson & Wong 2005). Scholz et al. (1972) observed an inhibiting influence of gouge on stick-slip behaviour. However, in the absence of gouge, the rough fault surfaces remain. It has been suggested (Paterson & Wong 2005) that these are less favourable to stick-slip behaviour than a smooth surface. What can be known is that the frictional properties of the fault within Experiment 7 will be different from Experiment 4 in which the fault was initially generated.

Figure 4.11: Sample preparation of the deformed core from Experiment 4 for Experiment 7. Part of the jacket has been removed to aid cutting of the sample.

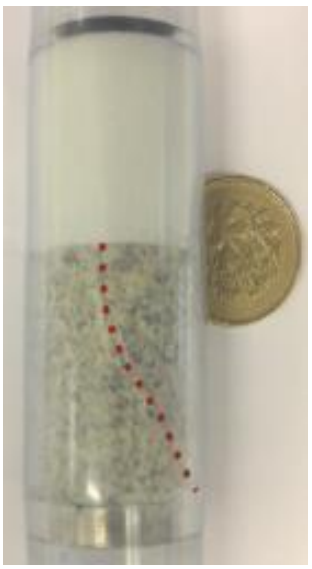

Figure 4 12: Experiment 7 set up prior to deformation. The red line traces the fault from Experiment 4 which has been cut so as to centre the base of the marble sample

Based on the results of Experiments 1-5 a confining pressure of 35 MPa was chosen for the second composite experiment. This confining pressure was chosen because at 35 MPa the

post-fractured granite in Experiment 5 was stably sliding at the same axial load at which the marble in Experiment 3, again at 35 MPa, underwent ductile deformation (Figure 4.13).

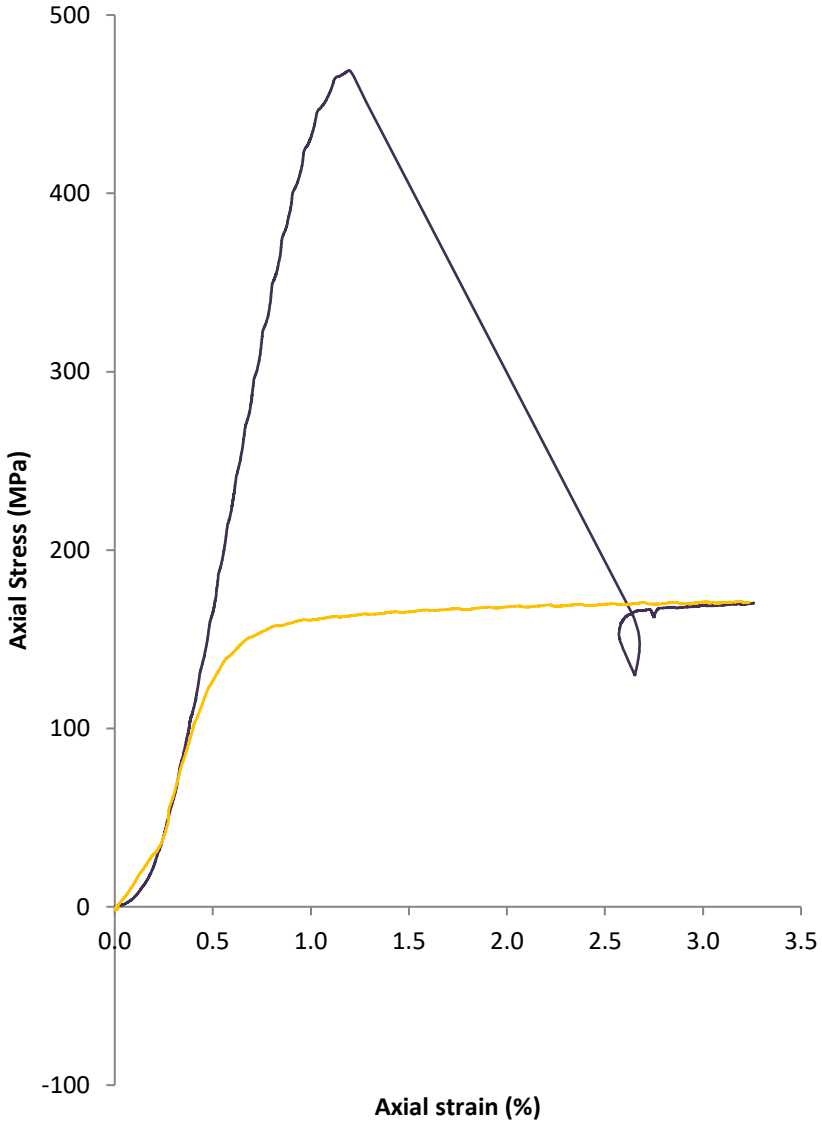

Figure 4.13: Axial stress (MPa) vs axial strain (%) for marble (orange) and granite (dark purple) from Experiments 3 and 5 respectively. The graph compares the deformation of marble and Westerly Granite at 35 MPa confining pressure. It can be seen that marble undergoes ductile deformation at the same axial stress that granite will stablely slide. The results have been corrected for machine stiffness and the start of the experiment was assumed as soon as the axial strain became positive.

4.4.2 Results of dual lithology experiments

Experiment 6: Composite experiment on initially undeformed samples

The first composite experiment showed purely ductile deformation after ~ 0.6 % axial strain. This can be seen in Figure 4.14 where the gradient begins to flatten after 0.6 % axial strain. Examination of the sample post deformation showed that the marble had buckled while the granite remained largely un-deformed. This suggests all the inelastic deformation was concentrated within the marble.

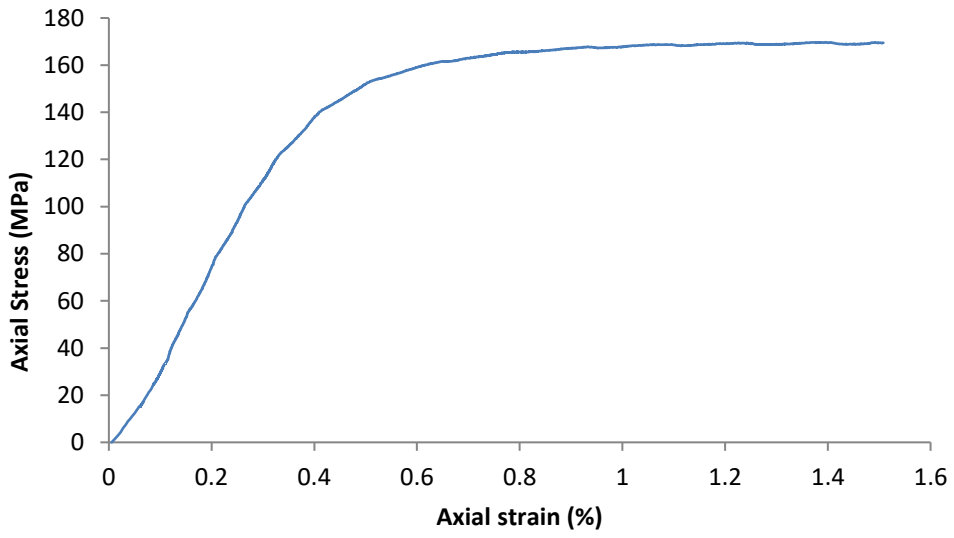

Figure 4.14: Axial stress (MPa) vs axial strain (%) for the first combined experiment (Experiment 6) conducted at 30 MPa confining pressure. The axial strain takes the entire length of sample into account. The graph has been corrected for machine stiffness.

Experiment 7: Second composite experiment on an initially faulted granite sample

The second composite experiment showed an overall prolonged phase of gradual strain weakening (Figure 4.16). A small stick-slip event seems to have occurred at 40 MPa (circled on Figure 4.16) but this could simply be an artefact caused by the machine adjusting during the experiment.

Post experiment analysis of the sample showed that a localised fracture had now developed within the marble (Figure 4.15). Additionally, a slight offset could be seen on the original fracture indicating a degree of movement had occurred. This is supported by the fact that deformation in the marble appears to have localised at the exact intersection with the fault in the granite. Slip on the granite sample therefore may have occurred, possibly during the strain weakening phase, loading the marble sample and inducing to failure. This would show that strain is still accommodated within the granite.

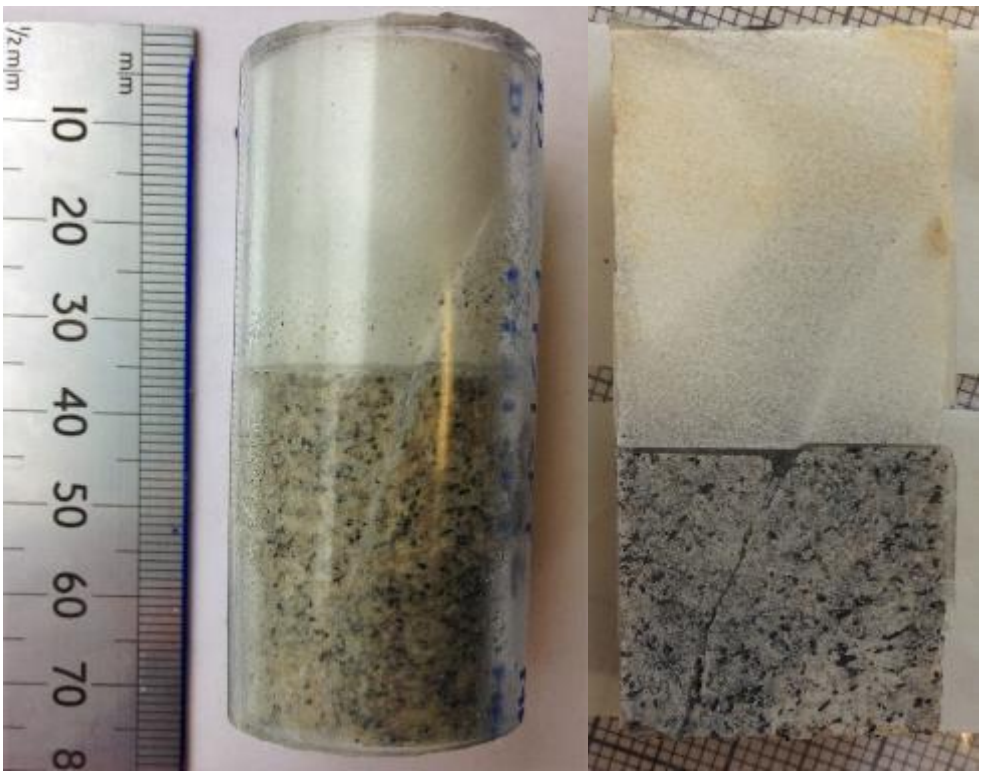

Figure 4.15: Experiment 7 post failure. Macroscopic localisation can be seen within the marble. The ruler, present for scale, shows cms.

A definitive stress drop is absent within the stress vs strain graph. Brittle and therefore seismic behaviour has previously been associated with stress drops in experiments within the literature (Das & Scholz 1983; Vallée 2013). It could be speculated that because of the presence of the marble strain manifestation in the granite has been rendered slow and aseismic

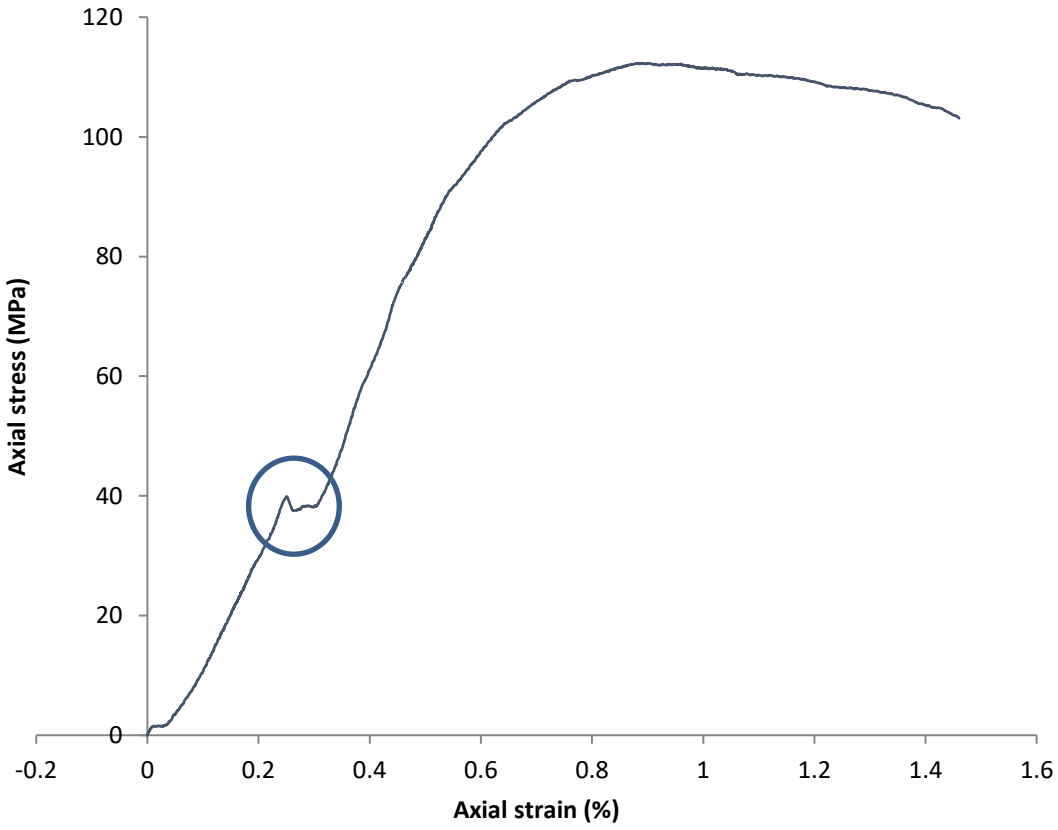

Figure 4.16: Axial stress (MPa) vs axial strain (%) for Experiment 7 conducted at 35 MPa confining pressure. The circle shows the potential stick-slip event at the beginning of the experiment. As both the marble and granite were deforming the axial strain is calculated by taking into account the whole length of the sample. The data have been corrected for machine stiffness.

.

4.5 Mohr circle analysis

Mohr circles were created for all preliminary experiments (Figures 4.17 and 4.18). They were not created from the composite experiments as the sample L:D ratio is smaller and would, therefore, affect the strength of the sample, rendering them non-comparable to Experiments 1-5. The point of failure was taken as the peak axial stress found within each sample. In Figure 4.18, the faults from Experiments 4 and 5 make slightly different angles with respect to the principal stress (σ_1). It is common for this 'beta angle' to vary by a few degrees between experiments (Lockner 1998). Envelopes of failure were fitted for both of the measured fault angles.

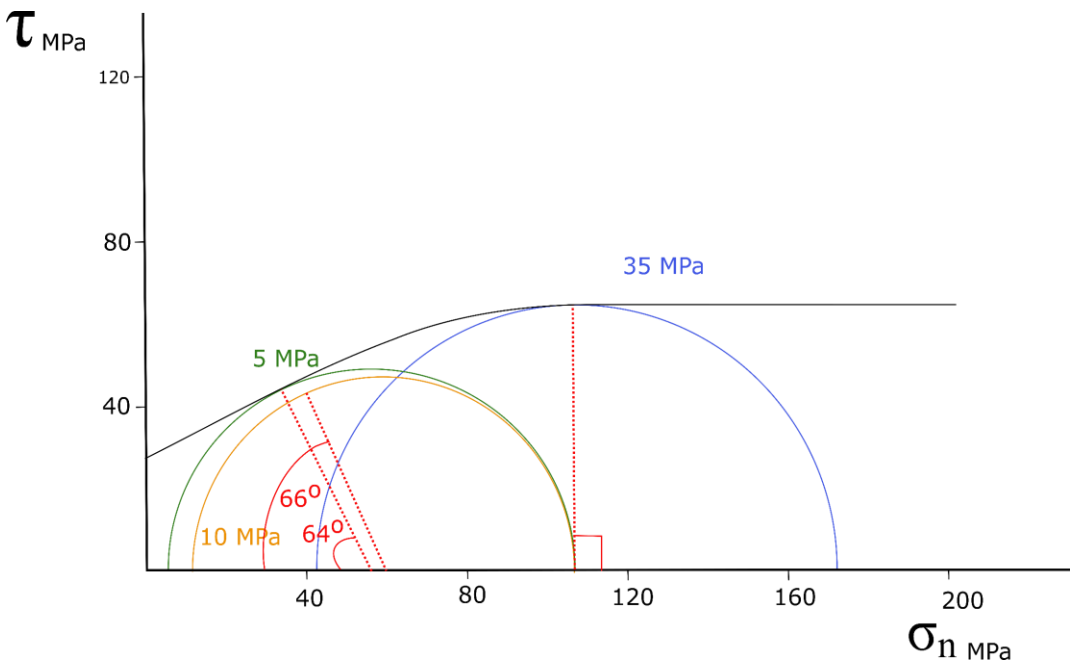

Figure 4.17: Mohr circle for marble created with data from Experiments 1-3.

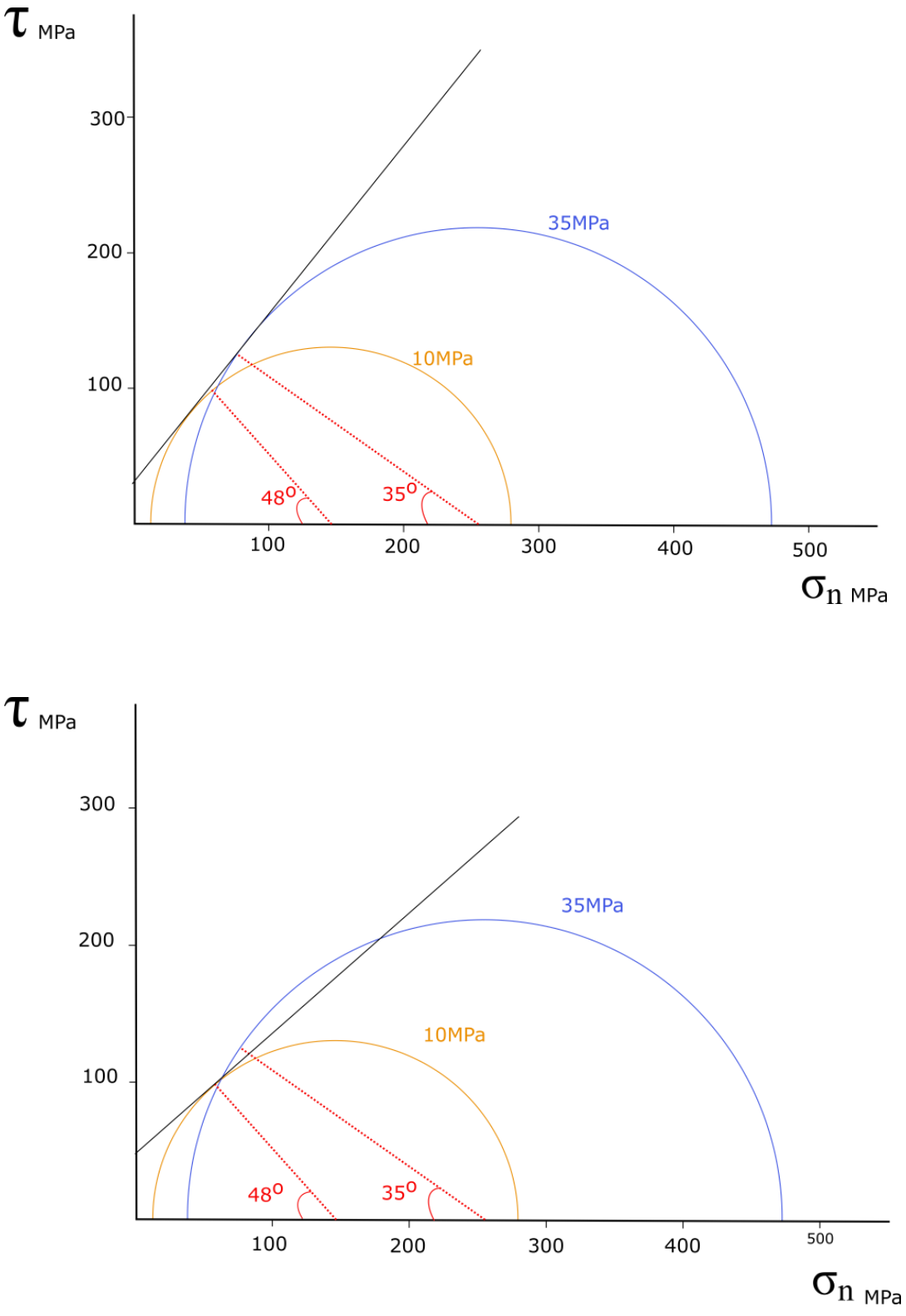

Figure 4.18: Mohr circle for Westerly Granite created with data from Experiments 4 and 5. The top images shows the failure envelope plotted in respect to the fault found in Experiment 5 and the bottom image shows the failure envelope plotted in respect to the fault formed in Experiment 4.

The coefficient of frictional sliding (μ_f) was used to predict at which point the fault in Experiment 7 was reactivated. Byerlee's law predicts a μ_f value, for low confining pressures (< 200 MPa), of 0.85 (Fossen 2010). Comparing the implied μ_f values at different points in Experiment 7 may give more of an idea of when the fault moved. Estimates for μ_f were calculated from the fault angle and σ_1 and σ_3 values at different points of the experiments (Figure 4.19). It was assumed that the fracture is cohesionless.

The small stress drop at 40 MPa correlates with a μ_f value of 0.121 which is too small for slip on the pre-faulted granite and is therefore likely to represent instead an adjustment of the machinery. Within the axial stress vs axial strain graph the best match between the calculated μ_f value and that predicted by Brylee's formula is at the onset of strain weakening at 0.9 % (μ_f value of 0.723). The inelastic behaviour presented in Figure 4.19 before the suspected movement on the fault suggests the marble is deforming in a ductile manner prior to the localisation associated with fault movement. This can be used in support of the idea that aseismic slip could have occurred due to ductile deformation in the marble suppressing seismic deformation in the granite.

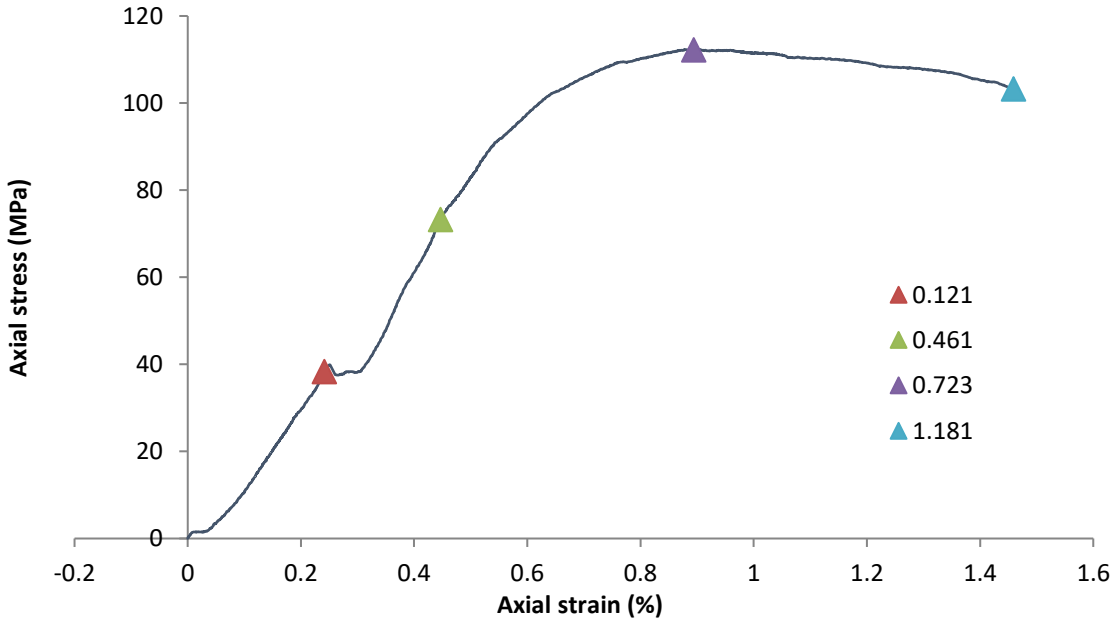

Figure 4.19: Graph displaying how the frictional coefficient varies throughout Experiment 7. Axial stress (MPa) is plotted against Axial strain (%). As both the marble and granite were deforming the axial strain is calculated by taking into account the whole length of the sample. The data has been corrected for machine stiffness. The triangles refer to locations where the frictional coefficient (μ_f) was calculated and the values of such coefficients are given in the legend.

4.6. Deformation microstructures

Thin section analysis was undertaken in order to compare the microstructures within the composite experiments to those in the single lithology experiments. Thin sections were cut on a plane parallel to the compressional axis in order to see the vertical persistence of the fault zone. Analysis of the microstructures prior to deformation was undertaken for both the marble and granite samples. This allowed a pre-deformation base level to be determined so variations caused by deformation could be identified. Thin section analysis is not described for the deformed sample from Experiment 6 as the microstructures are similar to those found in Experiment 3, where marble deformed in a ductile manner at 35 MPa confining pressure.

4.6.1 Preliminary experiments – Marble

Marble – pre-failure

The original composition of the marble consisted of 100 % anhedral calcite grains with an overall inequigranular- interlobate grain structure as can be seen in Figure 4.20. Such inter-granular relationships are suggestive of BLG-recrystallisation and potentially GBM-recrystallisation.

Grain size was inequigranular, ranging from 0.5 mm to 5.5 mm, slightly bigger and less uniform than that of the Carrara Marble found within the literature (see Section 4.1.2 for further information). Type II twinning (twin thickness > 1 μm) was observed in 30 % of the calcite grains (Figure 4.21), indicating previous deformation reached temperatures of at least 200 ^{o}C. This is consistent with the evidence of dynamic recrystallisation which requires temperatures of above 250 ^{o}C (Passchier & Trouw 2005). No intragranular fractures were observed and undulose extinction was also absent.

.

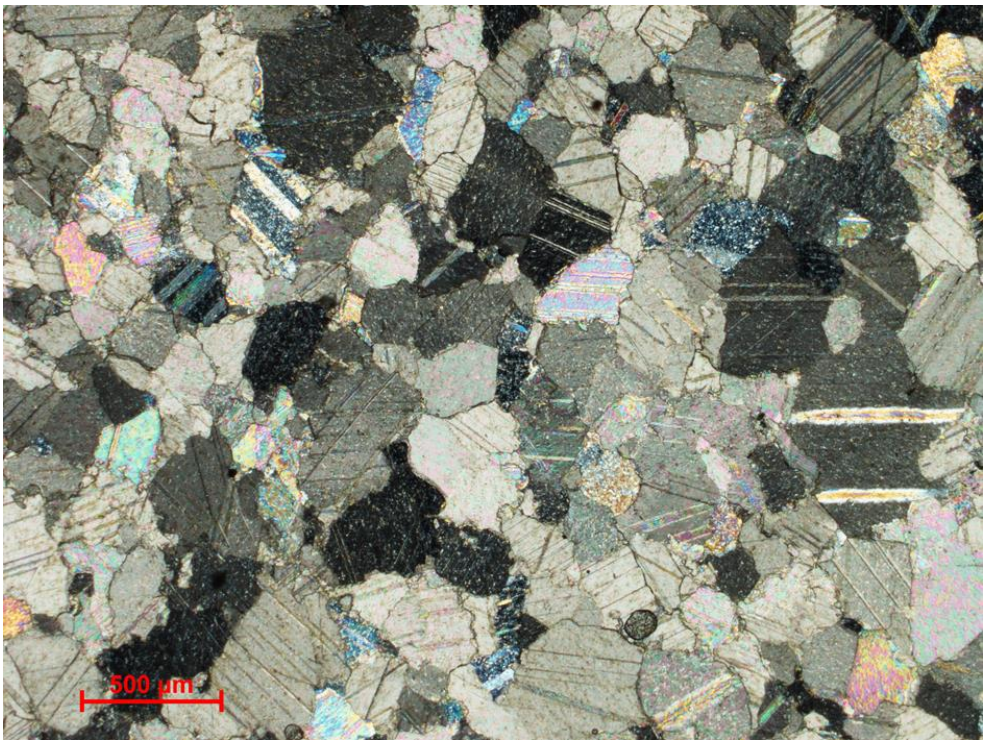

Figure 4.20: Thin section of marble prior to deformation. Thin section is presented in cross polarised light at 2.5x magnification. The thin section presents an overall inequigranular-interlobate grain structure as well as the low density of twins prior to deformation.

Figure 4.21: Thin section of marble prior to deformation. Thin section is presented in cross polarised light at 10x magnification. Within the centre of the thin section, Type II twinning can be seen in calcite.

Marble post-failure - Experiment 1: (5 MPa)

The grain structure observed for the post deformation sample in Experiment 1 ranged from polygonal to interlobate with individual grains presenting a subhedral form. Grain size was inequigranular, ranging between 0.5 mm to 5.5 mm. Deformation was seen to be strongly heterogeneous, localised on a set of conjugate faults. Surrounding the fault 70 % of grains possessed deformation twinning (Figure 4.22). In comparison, away from the fault planes the base level percentage of twinning (30 % of grains, established from pre-deformation analysis) is observed. As can be seen in Figure 4.22, twinning appeared to be predominantly Type I (twin thickness < 1 μm) around the fault zone compared to predominantly Type II further away from the central zone of deformation. At low temperatures (< 170 ^{o}C) an increase in strain is known to cause the growth of Type I deformation twins (Passchier & Trouw 2005) and represents the concentration of strain along the fault zone.

Intergranular fractures, where present, extended over up to four grains and tended to be located around the fault. However, their occurrence within Experiment 1 was rare. Overall, the section presented clear localised brittle deformation assisted by twinning.

Figure 4.22: Experiment 1 in plane polarised light at 2.5x magnification. The increase in Type I twinning can be seen adjacent to the fault plane in addition to the overall localised deformation.

Marble post-failure - Experiment 2 (10 MPa)

Grain size within Experiment 2 was inequigranular ranging from 0.8 mm to 7.5 mm. Grains in general were subhedral with aggregates presenting a range of structures from polygonal to interlobate. One grain of quartz was identified and presented strongly undulose and sweeping extinction. This quartz grain appeared to be stretched along the fault zone. However, its deformation is considered to have occurred in a previous event due to the higher temperature normally associated with the sweeping extinction (300-400 ^{o}C) seen within quartz (Passchier & Trouw 2005).

Deformation was localised along two conjugate faults (Figure 4.24). The fault core consisted of purely gouge within the centre of the section but the extremities of the sample displayed both fault gouge and a surrounding cataclastic zone. The fault was not through going, but instead consisted of side-stepping structures (Figures 4.23 & 4.25). In one section, the fault consisted of an en-echelon array of smaller fractures. Intergranular fractures were present and propagated across up to four grains. Both intra- and inter- granular fractures trended in the same direction as the main fault zone, approximately 33^{o} to σ_1.

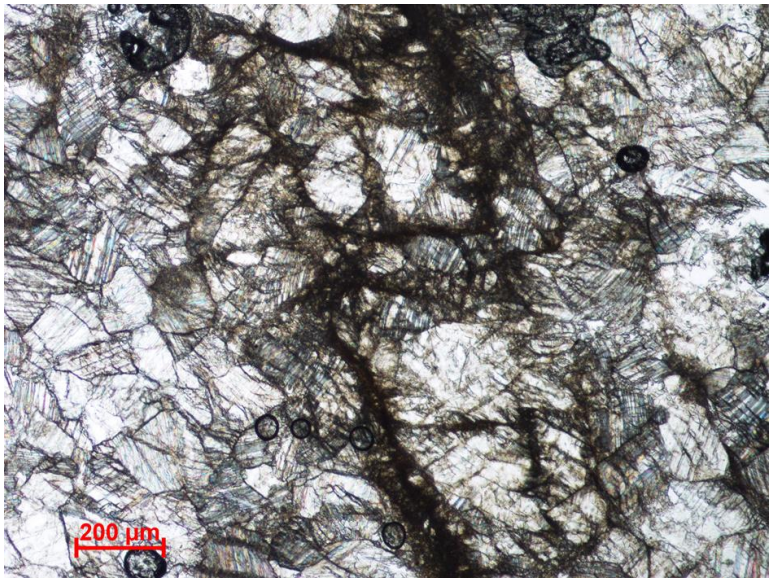

Figure 4.23: Side-stepping structures on the fault plane within Experiment 2, shown in plane polarised light at 5x magnification.

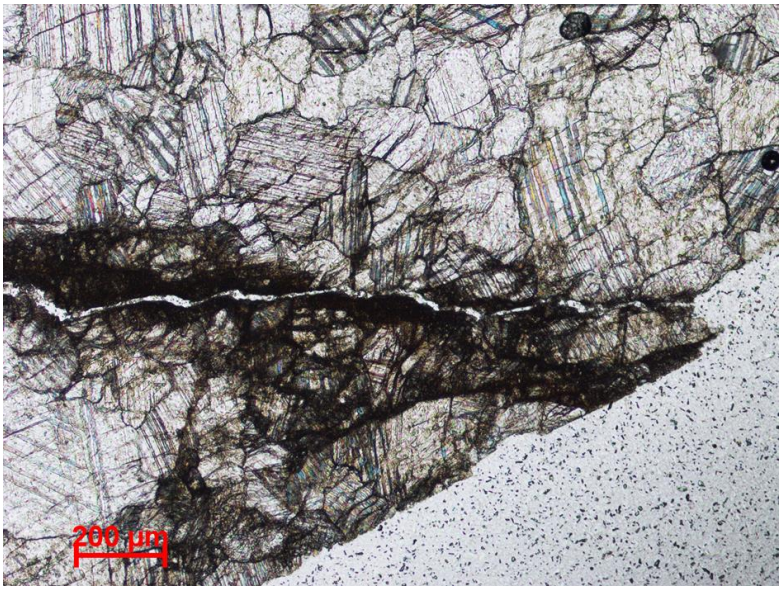

Figure 4.24: Fault zone from Experiment 2 seen in plane polarised light at 5x magnification. Dilation can be seen at the fault core near the edges of the sample. The thin section also highlights the high concentration of Type I twinning around the fault zone.

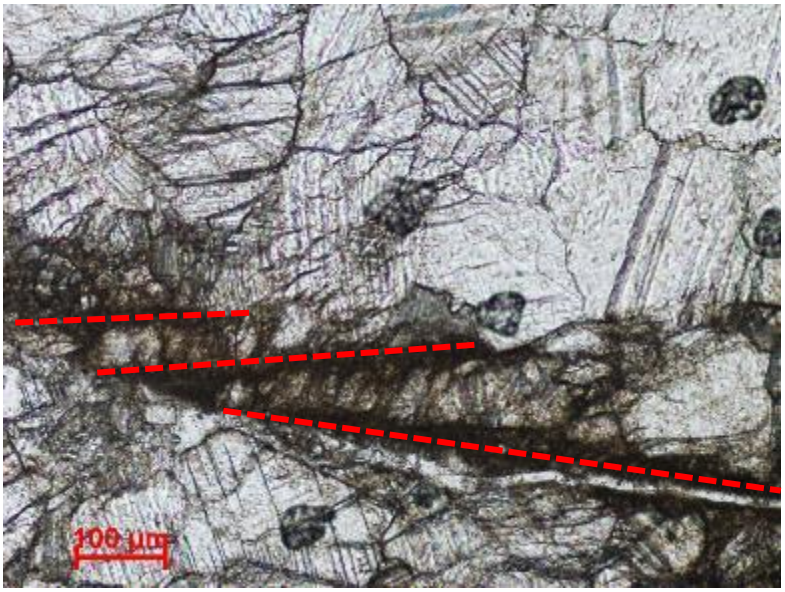

Figure 4.25: Side-stepping structures on the main fault zone within Experiment 2. Image is shown in plane polarised light at 2.5x magnification. Fracture cores are identified by the red dashed line.

Deformation twinning became less common progressively further from the main fault zone. Of the grains surrounding the fault zone, 100 % contained Type I deformation twins and intragranular fractures. In comparison, away from the fault zone no grains contained intragranular fractures and a base level of 30 % contained twins. Therefore, the twinning at 10 MPa confining pressure is more persistent than that at 5 MPa. An explanation for this could lie in Experiment 2 being taken to a greater amount of strain than Experiment 1 (3.6 % cf 1.9 %) as calcite twin density is known to increase with the extent of strain (Passchier & Trouw 2005).

Sweeping and undulose extinction was seen in some grains adjacent to the fault. Kinking of twins was also witnessed, and in various places the twins appeared to be breaking down. This may be an artefact of previous deformation or alternatively be suggestive of semi-brittle (semi-ductile) deformation (Fredrich et al. 1989).

Marble post-failure Experiment 3 (35 MPa)

At the higher confining pressure (35 MPa) of Experiment 3, there was no localised deformation. Grain sizes ranged from 0.5 mm to 6.0 mm. Within the sample, 90 % of the grains contained deformation twinning (Type I) and the overall deformation was homogenous. Figure 4.26 shows evidence of kinking of twins within some grains, indicative of dislocation glide. Bent and kinked twins have been found to occur at room temperature within Fredrich et al.'s (1989) experiments, and are associated with distributed deformation and microcracking. In some places evidence for twin boundary migration recrystallisation (Figure 4.27) is seen. Such recrystallisation is normally associated with high strains under

Figure 4.26: Experiment 3 shown in cross polarised light at 20x magnification. Deformation twinning within the thin section can be seen to be bent suggestive of dislocation glide.

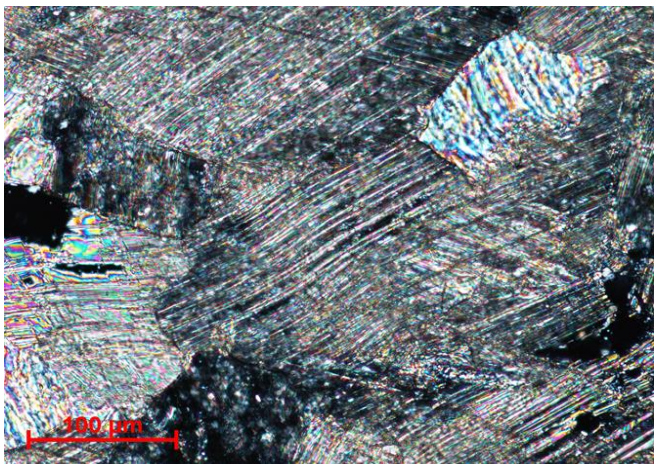

Figure 4.27: Experiment 3 shown in cross polarised light at 20x magnification. Two grains within the thin section show potential twin boundary migration recrystallisation within calcite.

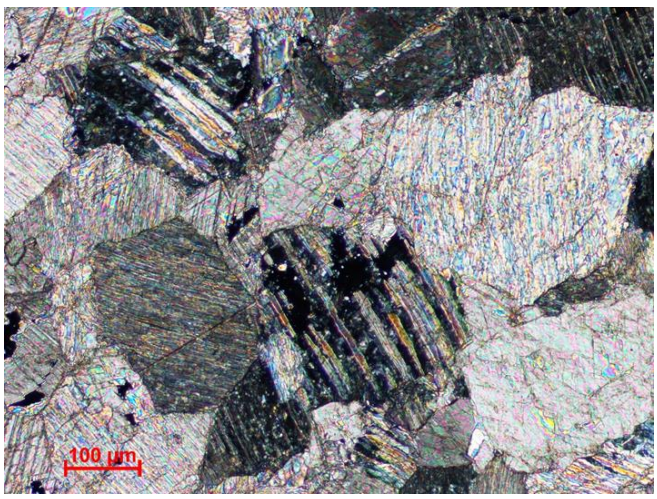

digenetic conditions (Passchier & Trouw 2005) and, therefore, is likely to have been associated with a previous deformation event which occurred at greater temperature.

Undulose, but not sweeping, extinction was seen within the sample. Some grains still had intragranular fractures. Intergranular fractures were also present within some grains. At such temperatures and pressures it appears that the sample does not reach conditions at which large amounts of dynamic recrystallisation can occur. Therefore, ductile deformation appears to be accommodated by deformation twining.

4.6.2 Preliminary experiments – Westerly Granite

Westerly Granite – pre-failure

An approximation for the mineral composition within the Westerly Granite sample used in Experiments 4-7 is as follows: 40 % quartz, 30 % plagioclaise, 20 % microcline, 10 % biotite, 1% muscovite and < 1 % myrmekite (Figure 4.28). This mineral composition is comparable to that quoted in the literature (Section 4.1.1) but the undulose extinction and both intra- and intergranular fractures reported elsewhere were not observed. Many of the feldspar minerals throughout the sample had begun to breakdown into muscovite which again is consistent with the literature.

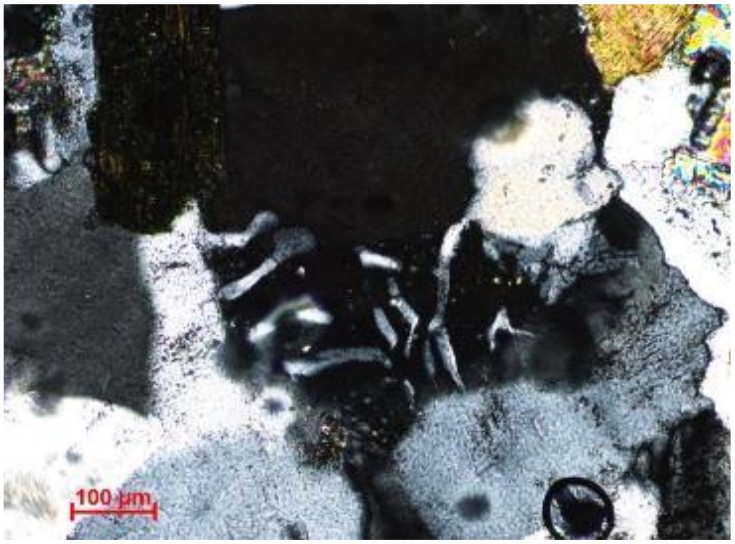

Figure 4.28: Thin section of the original granite sample in cross polarised light at 10x magnification. The centre grain is thought to be Myrmekite.

Granite post failure Experiment 5 (35 MPa)

Deformation was concentrated on one main fault that splayed branches of thinner localised fractures. The fault core consisted of a narrow, calcite-rich gouge zone surrounded by a cataclastic zone. The thickness of the cataclastic zone compared to the gouge varied along the fault as did the overall thickness of the fault zone. Grains adjacent to the main fracture were heavily deformed, with both intra- and intergranular fractures running parallel to the main fault zone which was formed at an angle of 17.5° to σ_1. The proportion of grains within the damage zone of the fault that contained intragranular fractures varied from 80-100 % along the fault zone. Grains were deformed irrespective of their mineralogy. Intergranular fractures were also identified, running through up to 6 grains. Away from the main fault plane only 1 % of grains contained any form of fracture.

4.6.3 Composite experiments

Experiment 7 - Within the Westerly Granite

A small offset, seen in Figure 4.29, at the boundary between the granite and the marble suggested the fault was reactivated. Within the Westerly Granite section the fault remained localised, with a small damage zone consisting of heavily fractured adjacent grains while deformation away from the fault zone was minimal.

Experiment 7 - Within the marble

Examining the sample post-failure showed a localised fault within the marble, despite the lack of a significant stress drop within the axial stress vs axial strain graph (Figure 4.16). The microstructures within this sample differed from those observed in Experiments 1-3, principally in the geometry of the main fault. The fault zone was non-continuous, consisting of sidestepping fractures similar to those seen within Experiment 2. However, the fault was not a linear discrete fault plane but instead consisted of small semi-ductile shear zones. Nearing the extremities of the sample the fault zone became more distributed as can be seen in Figure 4.34.

There thus appears to be a transition from a semi-ductile shear zone to a more purely ductile deformation.

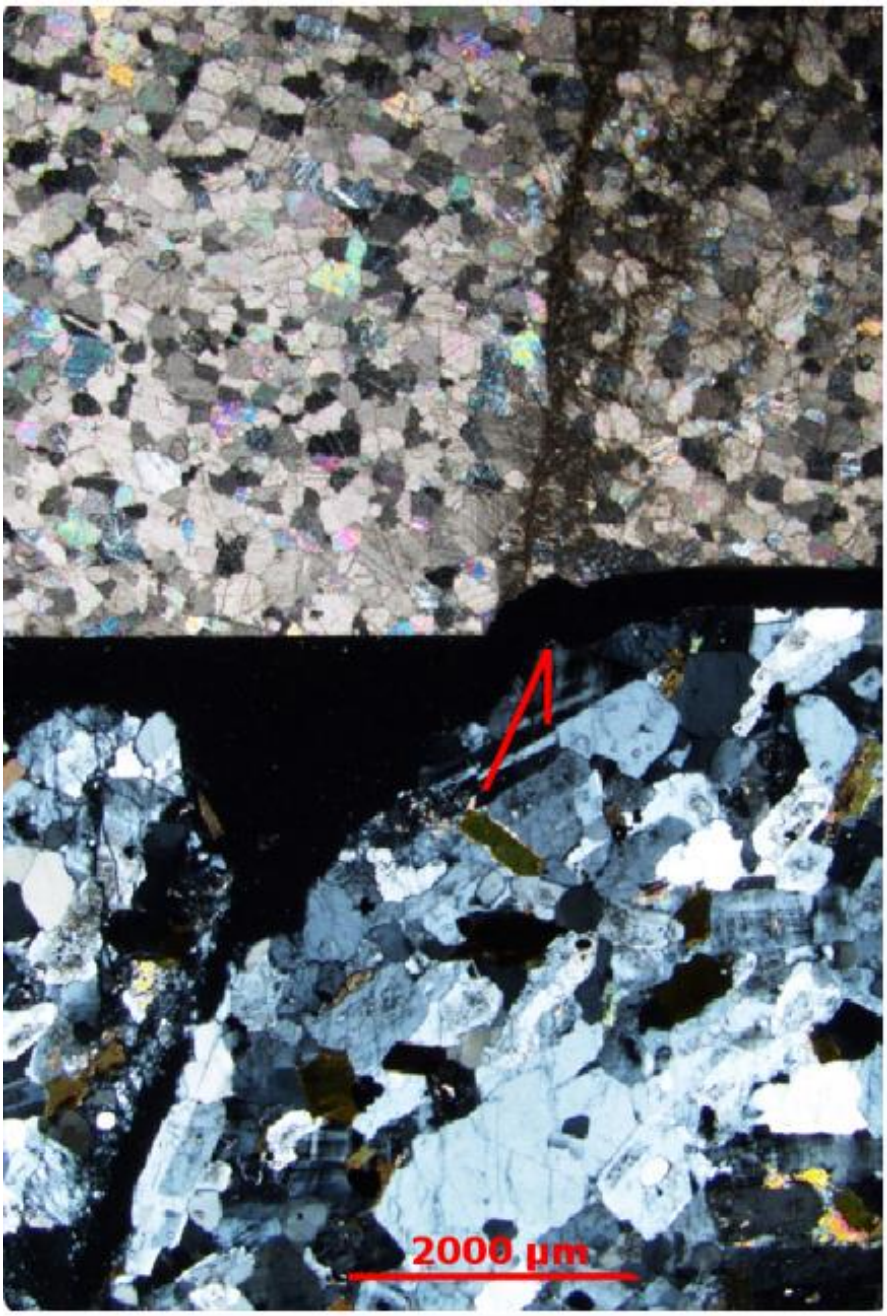

Figure 4.29: Experiment 7 shown in cross polarised light at 1x magnification. The interface between the granite and marble is seen at the centre of the image. The brittle fracture appears to propagate into the marble. The red arrow indicts movement on the fault.

Around the fault the sample is heavily fractured with 100 % of the grains containing intragranular fractures. Intergranular fractures, where present, extend up to 4 grains. Fracturing becomes less frequent with distance from the fault zone. Compared to brittle failure in Experiments 1 and 2 (where fractures surrounding the main fault ran parallel to it) fractures were perpendicular to the fault zone taking the form of an en-echelon array (Figures 4.32 & 4.33) and indicated non-coaxial deformation.

An increase in the amount of twinning is seen in association with the fault, with 100 % of grains surrounding or within the fault zone containing Type I twins. Away from the localised fault there was less twinning present (41 % of grains), but the level was still higher than in the undeformed material. The increase in twinning at the extremities of the sample further supports the theory that deformation within the marble occurred prior to movement on the fault. Twinning is known to be more prevalent at higher temperatures due to the thermal weakening of calcite thus increasing the effectiveness of crystal-plastic mechanisms (Ferrill et al. 2004). Likewise, the weakening of the rock from brittle deformation could also increase the prevalence of twinning.

Some twins were found to be bent (Figure 4.31), similar to those seen in Experiment 3. Kinking can also be identified in calcite adjacent to the fault plane which is suggestive of dislocation glide. Evidence can be seen in Figure 4.30 for grain boundary migration, with the twins ending before the grain boundary is reached. This implies the twins are left behind by the migrating grain boundary (Passchier & Trouw 2005). Dynamic recrystallisation is, however, thought to be absent below 250 ^{o}C in calcite (Ferrill et al. 2004). In large grains, and at high strain rates, dynamic recrystallisation within calcite may be activated instead by high dislocation densities rather than elevated temperatures (Ferrill et al. 2004). This is even more common in monomineralic calcite, suggesting the grain boundary migration witnessed in the thin section could result from the particular conditions of Experiment 7.

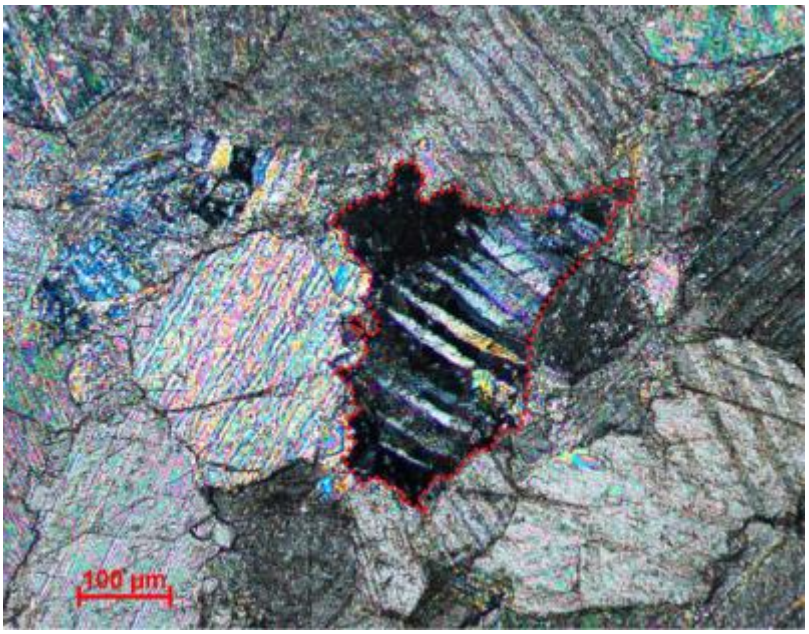

Figure 4.30: Thin section in cross polarised light at 10x magnification within the marble in Experiment 7. The central grain (outlined in red) presents evidence of grain boundary migration away from the twin structures within the grain.

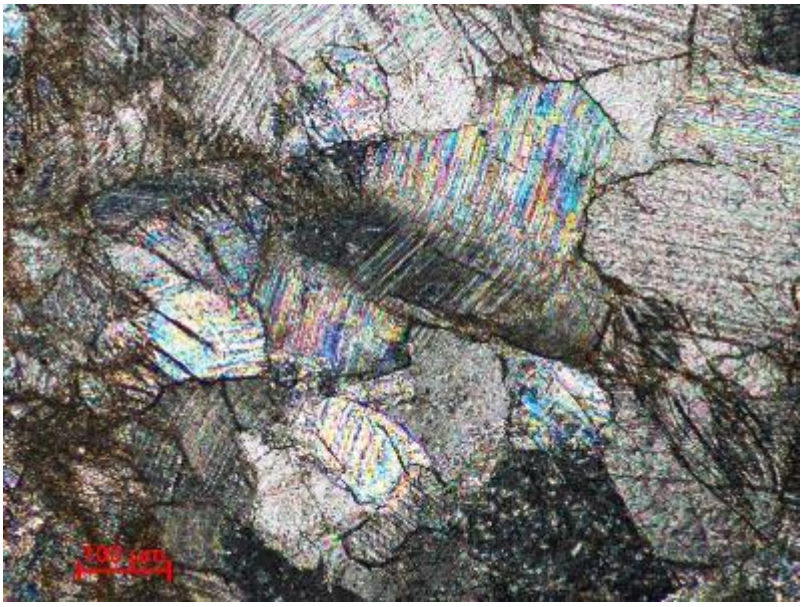

Figure. 4.31: Thin section in cross polarised light at 10x magnification within the calcite in Experiment 7. Kinking of the Type I twins can be identified in the centred grain.

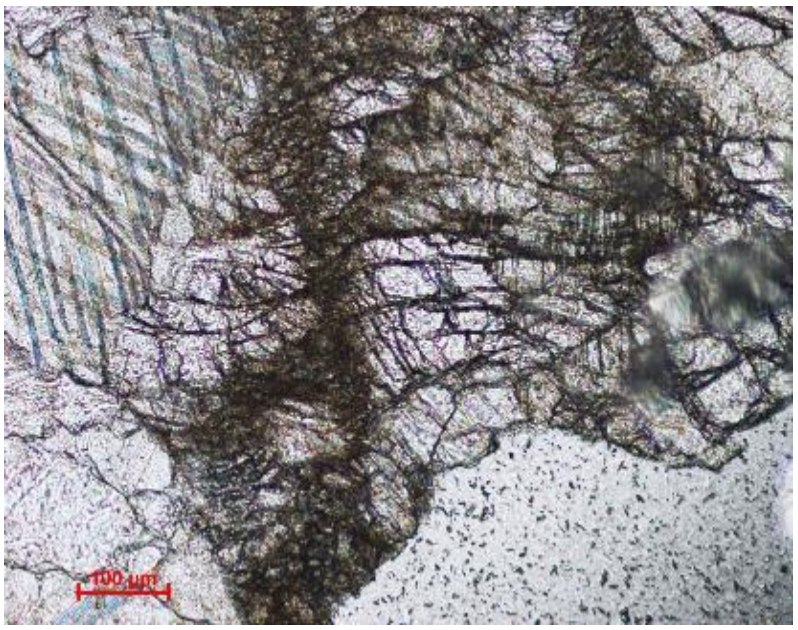

Figure 4.32: Thin section of the marble within Experiment 7 in plane polarised light at 10x magnification. The fault zone can be seen to be made up of an en-echelon fracture array which presents non-coaxial shear. This thin section shows the fault portion that is adjacent to the granite.

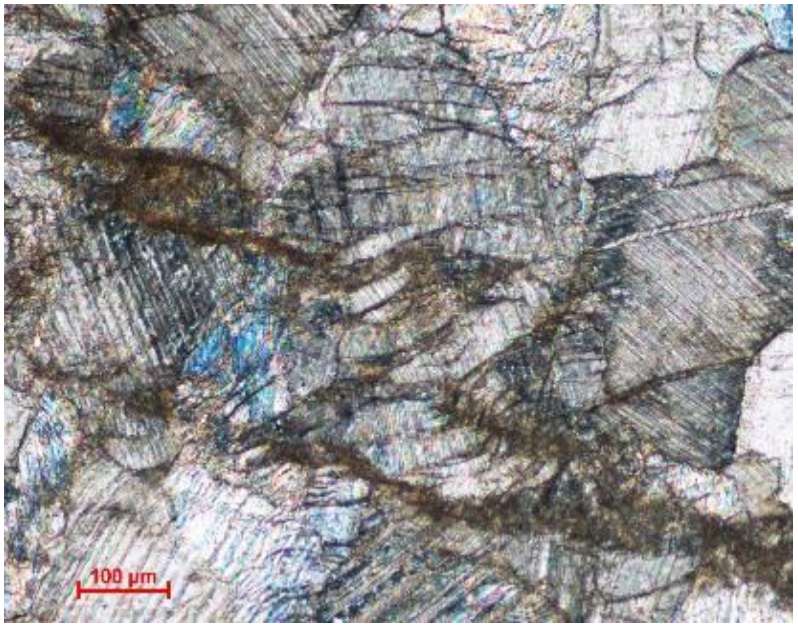

Figure: 4.33: Thin section of the marble within Experiment 7 in cross polarised light at 10x magnification.
En-echelon and side-stepping structures can be identified further away from the granite-marble interface.

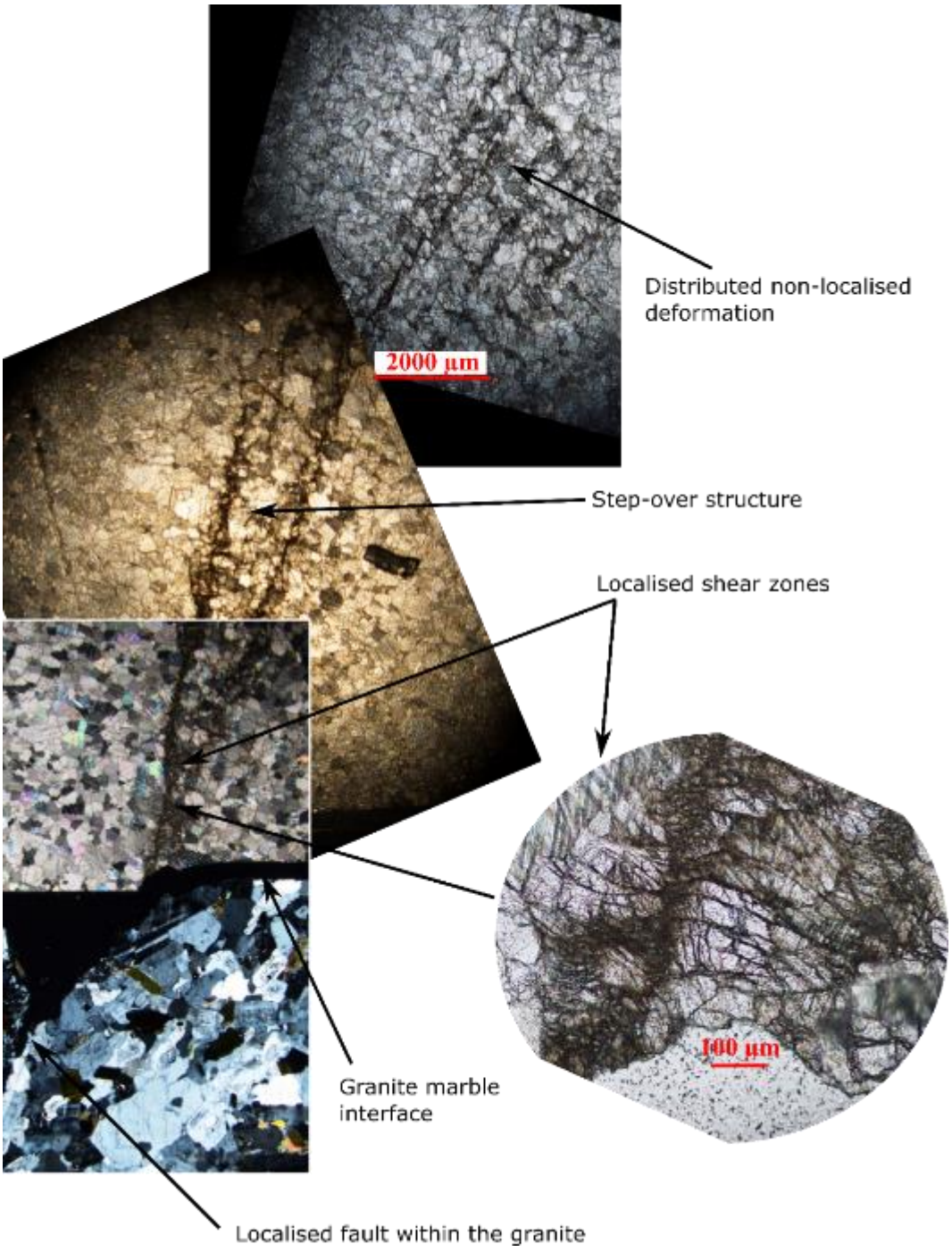

Figure 4.34 Overall geometry of the fault as it propagates into the marble. The bottom image is in cross polarised light and the top two images are in plane polarised light. Evidence can be seen that the fault becomes gradually more distributed as it propogates.

4.7 Discussion

4.7.1 Seismic implications of experimental results

The brittle-ductile transition has previously been correlated to the seismic-aseismic transition (Brantut et al. 2011). Therefore, examining the nature of a brittle fault's propagation into a ductile regime is of significant interest in the broader context of this study. The main focus of this discussion is, as such, on the composite experiments.

The stress vs strain graphs for both Experiment 2 and Experiment 7 (Figures 4.6 & Figure 4.16) showed a localised fault with a long period of slow strain weakening and no immediate stress drop after the peak stress/yield stress. Such a long period of slow weakening has been associated with vergence on the brittle-ductile transition (Paterson & Wong 2005) or alternatively on the formation of shear bands (Fossen 2010), either of which would suggest an interplay of brittle and ductile deformation mechanisms. Such slow and silent failure could be thought to be aseismic (Brantut et al. 2011), consequently implying that a hybrid of brittle and ductile behaviour has an effect on seismicity.

Within Experiment 7, deformation in the calcite sample was clearly localised, but the structure of the fault zone differed from that of the localised fault zones found in the preliminary experiments (Experiments 1-3). Instead, the sample was seen to form multiple small semi-ductile shear zones, in a side-stepping formation, which contained both ductile and brittle structures (Fossen 2010). Experiment 7 differed significantly from the preliminary experiments in that it contained an en-echelon array of fractures (Figure 4.32) denoting expansion perpendicular to the fault zone. It has been suggested that the marble was deforming in a ductile manner prior to the forced localisation associated with movement on the faulted granite. As such, this formation could be unique to the situation where a localised structure forms within a ductile material. The en-echelon array also showed evidence for non-coaxial deformation, with simple shear (Fossen 2010). This is consistent with the idea that the shear zone is associated with reverse movement on the fault within the granite.

It is known that cracks occurring at high angles (> 45°) to σ_1 are potentially the result of residual stress and are formed when unloading the sample rather than during the experiment (Tullis & Yund 1977; Zhang et al. 2004). As the en-echelon array presented in Experiment 7 lies broadly perpendicular to σ_1, residual stresses must be considered. Such residual stresses scale with the confining pressure and differential stress, meaning experiments that are deformed at higher confining pressures are more likely to be affected (Zhang et al. 2004). The low pressures of Experiment 7, and the care taken in reducing the confining pressure post the experiment, mean that the en-echelon array can be confidently associated with the experiment.

Brantut et al.'s (2011) experiments, conducted at a range of temperatures and pressures on natural gypsum alabaster from Volterra (Italy), showed that rapid localisation could occur in a ductile medium via shear banding. No dehydration occurred within the temperature range of these experiments and so all observations are a result of thermomechanical processes. Such dynamic behaviour results from plasticity at elevated temperatures increasing the speed at which the shear zone propagates. In stress vs strain graphs, this is represented by an overall ductile strain hardening behaviour that is superimposed with small stress drops, each of which is associated with the formation of a shear band. Shear band propagation speed has been linked to an increase in stress drop. The propagation speed itself is dependent on temperature, with higher temperatures leading to faster propagation and, therefore, a more dynamic rupture with greater stress drops (Brantut et al. 2011). At lower temperatures, such as the experiments conducted within this study, slow aseismic behaviour of the shear bands is predicted. Therefore, should Experiment 7 have been conducted at a higher temperature, a stress drop could have been associated with the development of the shear bands that are present (Figures 4.33 & 4.34).

Despite being different from experiments conducted within this study, specifically in terms of the high temperatures, plastic deformation and overall strain hardening rather than softening, research such as Brantut et al.'s (2011) is nonetheless an example of semi-brittle behaviour in a ductile medium. Most importantly, the slow and silent shear banding is

supportive of aseismic localisation within the ductile regime at room temperature and high pressure.

Thin section analysis of Experiment 7 showed that the localised fault structure becomes distributed, dissipating at the extremities of the sample core (Figure 4.34). This distribution potentially indicates that the propagating fault gets inhibited by the surrounding ductile medium, and could be used to support the concept that seismicity in fold-and-thrust belts is dissipated/inhibited by a ductile layer.

4.7.2 Extrapolating the results of this study to continental plateaux

Experiment 6 showed that when the granite sample did not contain a pre-fractured fault the marble deformed in a ductile manner, accommodating all the strain and leaving the granite undeformed. Therefore, the aseismic fault propagation witnessed in Experiment 7 can only be analogous to natural earthquakes on existing faults. As most, if not all, earthquakes occur on pre-existing fault structures the results presented here are likely to be widely applicable.

Laboratory experiments are always liable to scaling issues when being applied as analogues for real world scenarios. The strain rates that are available within the laboratory are many orders of magnitude faster than those found in nature. In addition, the experiments reported here have not considered the effects of temperature and pore pressure. Elevated temperatures and, therefore, the initiation of plastic deformation, could influence the results seen in the shear zone within Experiment 7. Plastic deformation may result in a more prominent shear zone, which is able to accommodate a greater amount of en-echelon structures. An increase in temperature has also been associated with a decrease in the strength of the host material (Paterson & Wong 2005) which will affect the speed and nature of shear zone propagation.

4.8 Conclusion and future work

Within all the preliminary experiments the overall behaviour and microstructures were as expected from the literature reviewed in Section 4.1. However, the variation in microstructures resulting from Experiment 7 indicates that the localisation processes are different where a fault propagates into a medium which is deforming in a ductile way.

To the best of our knowledge, composite experiments involving two different lithologies which are deforming via different mechanisms have not been previously undertaken. The results of this study are the first of their kind and are, therefore, not comparable to any previous work. The lack of a stress drop within Experiment 7 implies an aseismic localisation process and that the presences of a ductile deforming layer can inhibit the propagation of a fault. Therefore, this work supports Hypothesis 3 for the seismicity cut-off (illustrated in Figure 4.1).

However, multiple experiments under the same conditions will be required to validate these preliminarily dual composite experimental results. In addition, the experiments do not take into account temperature which, as seen from Brantut et al's (2011) work, can have an effect on the speed that shear bands are able to propagate.

In order to examine the nature of shear zone propagation, re-runs of the experiment are required, stopping at various points including; immediately after the yield point and throughout the period of strain weakening. This would provide a greater insight into the propagation of the shear bands and would also make it possible to identify if the structures become more distributed. Additionally, repeating the experiment with the focus on determining the effects of temperature would be a good test of whether the aseismic propagation of the fault persists under a wide range of conditions.

The aim of the experiments was to generate an example of a brittle fault propagating into a ductile medium in an attempt to understand the associated seismic signature and microstructures, and in that sense the results presented here are both successful and of interest. However, the reported experiments are very specific and to draw a general conclusion about

whole mountain ranges from their results would be presumptuous. Therefore, this experimental data can be used to support Hypothesis 3 for the cut-off in seismicity with elevation, but alone it is incapable of providing a conclusive explanation for the lack of $M \geq 5$ earthquakes at high elevations.

Chapter 5

Discussion, future work and conclusions

5. Discussion, future work and conclusions

This work has addressed broad questions associated with continental plateaux, fold-and-thrust belts, and seismic activity - at a range of scales and using various techniques. Previous work (Nissen et al. 2011; Allen priv. comm.) has noted that M ≥ 5 earthquakes are rare at high elevations within continental plateaux. Possible mechanisms for this empirical seismicity phenomenon have been investigated here in association with the three previously defined hypotheses; 1 - The critical Coulomb wedge hypothesis, 2 - The gravitational potential energy/minimum work hypothesis and 3 – The thickening ductile interlayer hypothesis. The data collected within this project are discussed in the context of these three hypotheses in order to assess the applicability of each in explaining the observed seismicity phenomenon.

5.1 Evaluating the critical Coulomb wedge hypothesis

From swath profiles analysis it can be asserted that the four fold-and-thrust belts within this study fit a modified brittle-ductile critical Coulomb wedge (Williams et al. 1994). Two changes in gradient were identified within the convergence margin. In all cases the lower elevation change in gradient coincided with the cut-off in M ≥ 5 earthquakes extracted from the elevation vs magnitude plots (Chapter 2). Above this elevation, the orogenies continued to deform and rise until a second change in gradient occurred, in association with the formation of a plateau. A schematic of the proposed plateau structure is shown in Figure 5.1.

However, the data from Chapter 2 were subject to limitations. The Himalayan graph of elevation plotted against earthquake magnitude could be misleading due to the inability within this location to area-normalise the earthquake data. In addition, the data from the Zagros and the Qilian Shan were taken from small sub-sectors of the deformation front making the analysis more susceptible to outliers. Within the Qilian Shan in particular, the calculated plateau edge was found to represent movement on only a few individual faults. Therefore, care must be taken when analysing the swath profiles (Chapter 3) with respect to the data presented in Chapter 2.

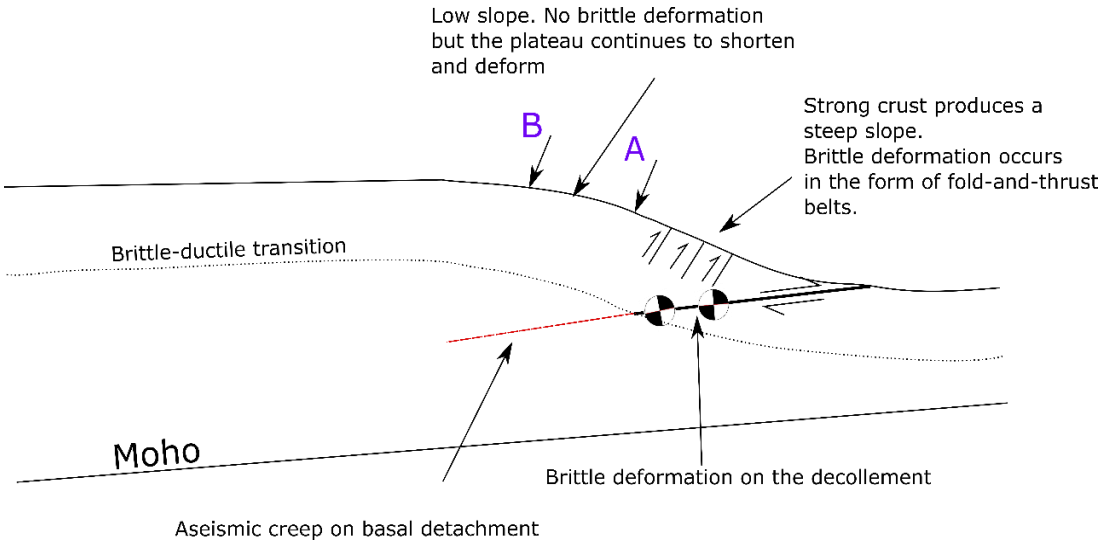

Figure 5.1: Schematic diagram indicating the two changes in slope found within a plateau. 'A' refers to the initial change in gradient which coincides with the cut-off in M ≥ 5 earthquakes extracted from the elevation vs. magnitude plots constructed in Chapter 2 and 'B' refers to the second change in gradient associated with the formation of a plateau. This suggests a link between the critical Coulomb wedge and M ≥ 5 earthquakes. This model is based originally on Williams et al's. (1994) brittle-ductile critical coulomb wedge model and has been vertically exaggerated.

5.2 Evaluating the gravitational potential energy (G.P.E) hypothesis

Minimum work processes were found to have a controlling influence on thrust faulting. Evidence in support of this assertion comes primarily from; 1) the uniformity in the reduction in earthquake concentration with elevation and 2) the greater proportion of larger earthquakes at high elevation.

With regard to the reduction in earthquake concentration with elevation; both the Qilian Shan and the CMT catalogue within the Himalayas present a uniform cut-off of $M \geq 5$ thrusts. Specifically, the $M \geq 5$ earthquake cut-offs occur at heights of 3500 m and 4000 m in the Himalayas (Figure 2.10) and the Qilian Shan (Figure 2.12) respectively. Such a relationship implies a consistent cut-off in seismicity at a certain elevation throughout a fold-and-thrust belt. The area-normalised number of earthquakes occurring in the Zagros also cuts-off abruptly (at 1250 m elevation), confirming previous qualitative relationships described by Nissen et al. (2011). Such patterns appear more consistent with the G.P.E. hypothesis than the critical Coulomb wedge hypothesis. Again, it is necessary to remember that the areas examined are small and may not be representative of the entire range.

With regard to the greater proportion of larger earthquakes at high elevation; activation of fewer, larger, more stable faults is the most energetically favourable situation. This applies at least until a critical elevation at which the work required against gravity is too extensive to overcome (Masek & Duncan 1998). Based on this, the increase in the proportion of $M \geq 5$ earthquakes with elevation is supportive of a conservation of energy controlled system, although it remains possible that these higher concentrations are simply the artefact of a small sample area which is easily skewed by the presence of one large earthquake.

However, the evidence in support of the G.P.E hypothesis is not unambiguous. A literature review of the localities used in this report identified a concentration of deformation in the higher and steeper regions of the Longmen Shan rather than the surrounding lowlands. The 2008 M 7.9 Wenchuan and 2013 M 6.6 Lushan earthquakes within the Longmen Shan both

occurred in the south - the highest and steepest area (Sun et al. 2016). Although these did occur just below the predicted seismicity cut-off, the internal thickening in the highest areas is somewhat contrary to the G.P.E. model. Sun et al. (2016) proposed this to be the response of the critical Coulomb wedge to the lengthening of the deformation zone by the development of the Longquan fold. If this is the case, it suggests that deformation to maintain the critical Coulomb wedge taper is the predominant driver rather than work minimisation.

The energetics associated with earthquakes are extremely complicated and can be affected by numerous factors, including both endogenous and exogenous conditions. Fault zone properties can be highly variable even between separate earthquake events on the same fault surface (Shipton et al. 2006). Therefore, the notion of a uniform cut-off in seismicity given such an inhomogeneous geology appears somewhat counter-intuitive.

In addition, the supposed uniform elevation cut-off of $M \geq 5$ earthquakes is hard to reconcile with the suggested presence of the Indian Shield under half the Tibetan Plateau (Styron et al. 2015). Molnar & Lyon-Caen's (1988) work assumes that horizontal forces, orientated perpendicular to the range, are transmitted across the range if there are no shear stresses at the base. Reconstruction of the Indian plate movement shows that the onset of extension sweeps northward ahead of the subducted Indian Shield by 50 km (Styron et al. 2015) indicating its influence on the overriding surface structures. Shear tractions from the Indian shield would be expected to affect the transfer of horizontal forces and result in a different energetic system. Likewise, the convergence and strain rates between India and Eurasia decrease from east to west along the Himalayas (Hirschmiller et al. 2014). Intuitively, it seems unlikely that a system which varies in this way would result in the uniform cut-off in thrust seismicity that is seen within the Himalayas and the surrounding plateau. However, it is possible that G.P.E. is simply massively dominant in its influence.

5.3 Evaluating the thickening ductile interlayer hypothesis

Experiments were performed in order to assess how a brittle fault propagates into a ductile medium. Thin section analysis of Experiment 7 showed that initially a fault continues to localise aseismically within a ductile medium but eventually becomes distributed, dissipating at the extremities of the sample core. This work supports the idea that a thickened ductile layer within the sedimentary layer can inhibit the propagation of large earthquakes initiating within the brittle basement.

Such evidence of aseismic localisation is particularly relevant to the Zagros, where a mismatch is seen between the rate of strain released seismically and the convergence accommodated by the range (Nissen et al. 2011). If moderate (M 5.0-5.9) to large scale ($M \geq 6.0$) earthquakes are considered, then seismic activity accounts for ~ 30 % of the overall strain rate in the Zagros (considering a seismogenic layer of 15 km). This mismatch appears mainly to occur at 10-20 km depth – i.e within the basement. The basement is, therefore, considered to be largely aseismic, yet the need to maintain strength in order to enable the occurrence of occasional large magnitude earthquakes at up to 20 km means it is unlikely to be ductile or plastic. Aseismic fault creep within the basement has been previously proposed as an explanation for the mismatch (Nissen et al. 2011). The experimental data presented here demonstrates aseismic shortening originating from brittle deformation which could be used in support of this theory.

These experiments, though of great interest, are subject to a number of specific conditions which mean that it is potentially invalid to extrapolate the results to the scale of a mountain range. Time constraints also prevented the repetition of any experiments. Therefore, while the experimental data can be used to support Hypothesis 3 for the cut-off in seismicity with elevation, in isolation it is incapable of providing a conclusive explanation for the lack of $M \geq 5$ earthquakes at high elevations. In addition, the model is likely to be transient, and therefore not applicable to regions deforming for millions of years.

5.4 Comparing and contrasting the different models

Three hypotheses put forward for the cut-off in M ≥ 5 earthquakes were explored within this study and evidence was found which supported aspects of them all. No one hypothesis appears to account for all the known data. However, these hypotheses are not mutually exclusive. A combination of the critical Coulomb wedge and G.P.E. hypotheses appears to offer the best explanation for the observed cut-off in seismicity, as well as for the overall plateau geometry. Figure 5.2 presents a hybrid of these two models.

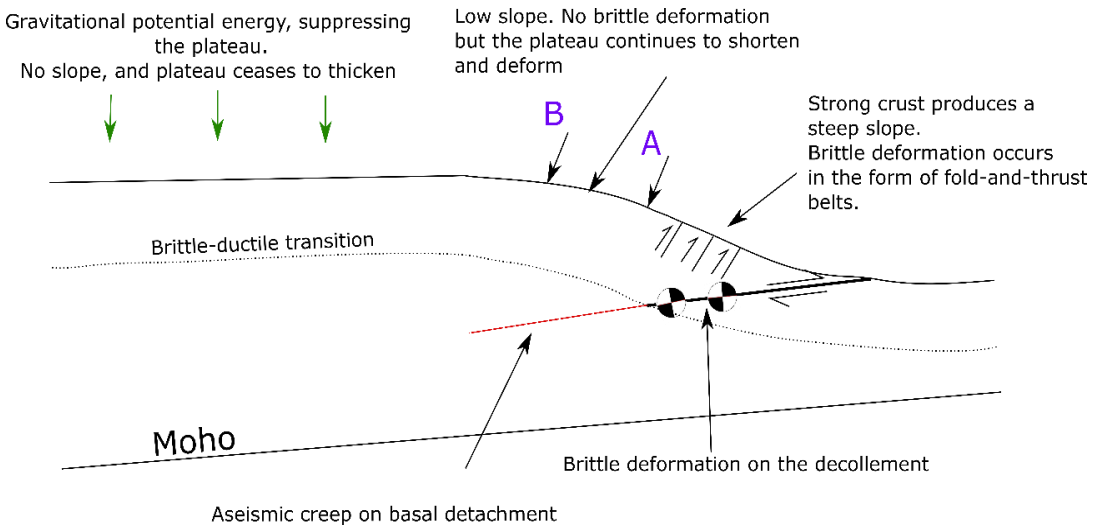

Figure 5.2: Modification of Figure 5.1 to include the limiting influence of G.P.E. 'A' again refers to the initial change in gradient which coincides with the cut-off in M ≥ 5 earthquakes extracted from the elevation vs. magnitude plots constructed in Chapter 2 and 'B' refers to the second change in gradient associated with the formation of a plateau. This model is based originally on Williams et al's (1994) brittle-ductile critical coulomb wedge model and has been vertically exaggerated.

Swath profile analysis identified two changes in gradient. Firstly, the slope gradient decreased but continued to be positive until a second turning point, after which a true flat plateau developed. A strong correlation is present between the reduction in M ≥ 5 earthquakes and the first change in gradient. Therefore, in all cases the fold-and-thrust belt continues to shorten and deform after the cut-off in major thrust earthquakes. This suggests that the cut-off in M ≥ 5 earthquakes occurs independently of the formation of a plateau but also that orogenies have a limiting elevation that they will reach regardless of the deformation mechanism. This limiting elevation is likely to be controlled by G.P.E.

How this continued aseismic deformation occurs is still a matter of debate. Potentially this could result from aseismic creeping on the basal decollement. One separate model investigated here is the influence of a thickened ductile interlayer on the propagation of large magnitude earthquakes originating in the basement. The aseismic localisation seen in Experiment 7 could, therefore, offer an explanation for the continued thickening of the orogeny after the reduction in $M \geq 5$ earthquakes.

5.5 Areas for future work

In the course of this project, many areas for further work have presented themselves and specific proposals for additional research have been touched upon within each of the individual chapters. Here, a few key areas for future research are suggested. In summary, the two main areas warranting further research are 1) quantifying the energetics of a plateau system to test further the G.P.E. model and 2) further experimental investigation of the propagation of a fault into a ductile medium.

5.5.1 Further examining the energy of a system

There is a large area of further research warranted in linking the seismicity cut-off to the G.P.E./minimum work model. Evidence in Chapter 2 suggests that fewer, larger magnitude, earthquakes were more favourable at higher elevations. To advance this work it would be interesting to quantify mathematically the total earthquake energy produced by thrusts at each elevation. The rate of change in the increasing demand of G.P.E. and the reduction in earthquakes could be evaluated to see if they are consistent by equating the sum of the energy at each elevation with the expected increase in G.P.E.

Within the experimental work it would be of interest to integrate the graphs of Figure 4.14 (Experiment 6) and Figure 4.16 (Experiment 7) to see if the aseismic localisation seen in Figure 4.16 is more energy efficient than the purely ductile behaviour in Figure 4.14. The strength of the ductile medium in Figure 4.14 will be greater than the marble in Figure 4.16 as a result of the smaller length:diameter (L:D) ratio of the nonlinearly deforming section (Hudson & Harrison 2000). Therefore, prior to comparing the energy associated with the graphs it might be necessary to re-run Experiments 6 & 7 with the marble thickness in Experiment 6 being a comparable length to the entire section of Experiment 7.

The presence of the Indian Shield under half of the Tibetan Plateau seems inconsistent with the uniform cut-off in seismicity. The interactions of the down going plate are likely to affect the overall energetics of the system and it would, therefore, be expected that the limiting

elevation was different above these regions. An attempt to try and model quantitatively the effect the Indian Shield has on the energetics of the Tibetan Plateau would be interesting. An overall mathematical analysis of the energetics, including the density of the rocks, the elevation and the convergence rate would be useful in determining if G.P.E was the controlling factor in plateaux geometry.

5.5.2 Expansion of the experimental data

The experimental data presented some interesting and previously unreported results. Initial further work would require ensuring the result from Experiment 7 is repeatable. Stopping the experiment at different accumulated strains would enable a better understanding of how the fault propagates (Figure 5.3).

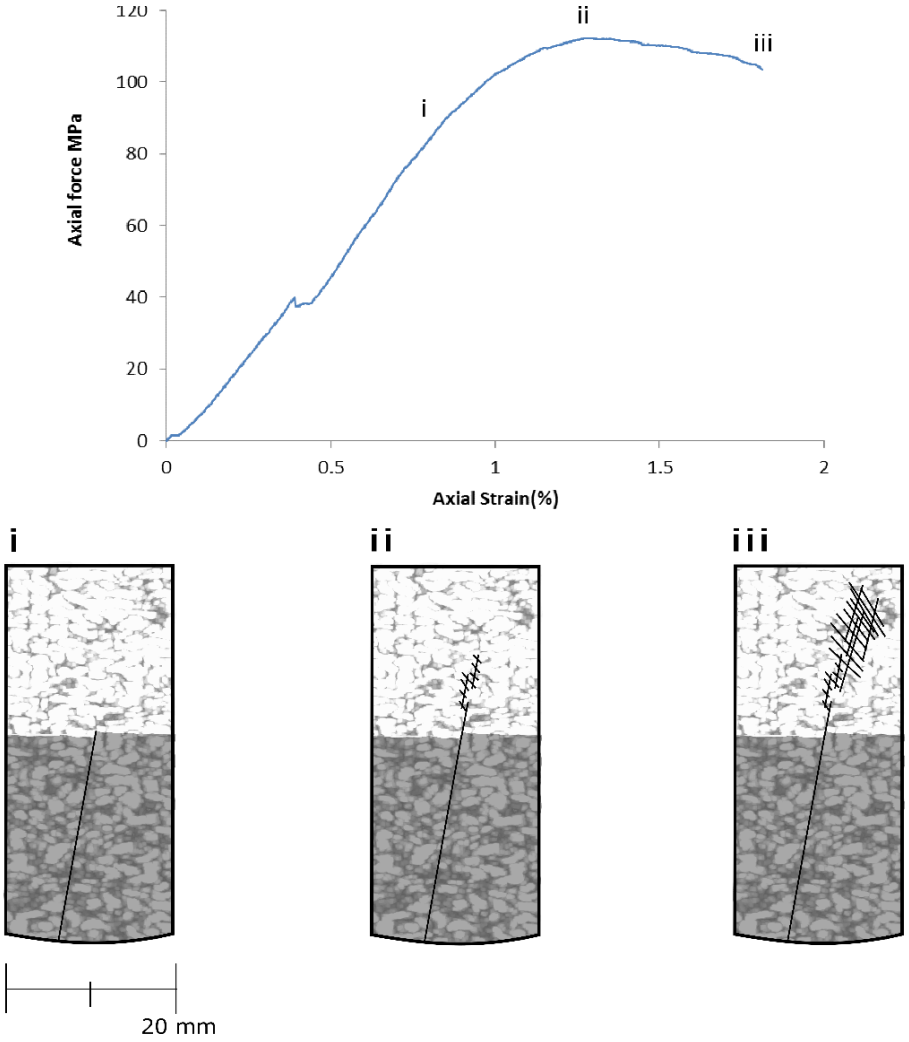

Figure 5.3: Suggested points at which to stop further combination experiments.

Constructing further combination experiments with different geometries would be another path worth exploring. A set up which involves an inner core of granite and an outer core of marble could be one approach. Attempting to induce failure of the granite in such a geometry, without a pre-cut fault, could give more understanding on the inhibiting influence of a ductile layer in an un-deformed section of crust. A schematic of the suggested core set up is shown in Figure 5.4.

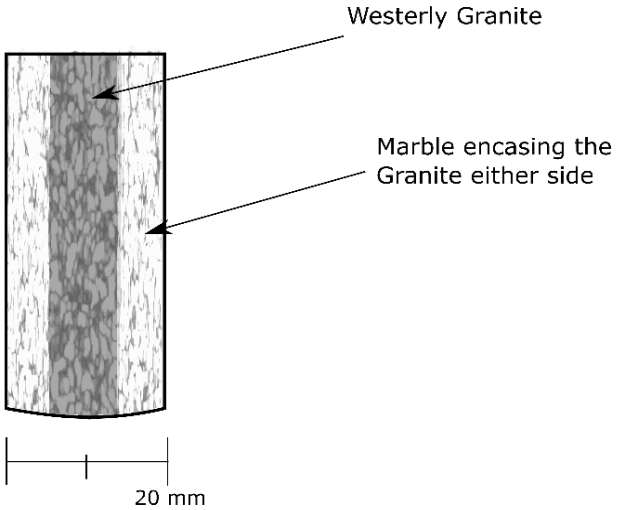

Figure 5.4: Suggested core set up for further dual lithology experiments.

5.6 Conclusions

It has previously been noted that larger thrust earthquakes (M > ~5) are rare at high elevations in continental fold-and-thrust belts. Data presented here have examined this seismicity phenomenon at a range of scales and using various techniques, and has drawn the following conclusions:

- All four studied regions appear to fit a modified brittle-ductile critical Coulomb wedge which contains two turning points in the average topographic profiles associated with changes in gradient.
- The cut-off in M ≥ 5 earthquakes is associated with the first turning point at an elevation lower than the plateau edge.
- The convergent margin continues to build aseismically after the cut-off in M ≥ 5 earthquakes.
- Plateaux form as a result of a limiting elevation controlled by G.P.E.
- The mechanism by which the continental margin continues to deform aseismically is unclear. In experimental data it has been seen that faults appear to localise aseismically when propagating into a ductile medium. Therefore, a thickened ductile interlayer within the sedimentary layer may inhibit large earthquakes, forming in the brittle basement, from propagating. This allows shortening in the brittle section of the sediments via smaller earthquakes while losing M ≥ 5 earthquakes.
- An alternative explanation to that suggested above is that aseismic creep on a ductile deforming basement thrust allows the continental margin to continue to deform.

Therefore, this thesis rejects the 'pure' versions of Hypotheses 1-3 as complete explanations for the empirical relationship between large thrust earthquakes and elevation. Instead the hybrid model of Hypotheses 1 and 2, seen in Figure 5.2, is favoured.

References

Allen, M.B. et al., 2013. Orogenic plateau growth: Expansion of the Turkish-Iranian Plateau across the Zagros fold-and-thrust belt. *Tectonics*, 32(2), pp.171–190.

Brantut, N., Schubnel, A. & Guéguen, Y., 2011. Damage and rupture dynamics at the brittle-ductile transition: The case of gypsum. *Journal of Geophysical Research: Solid Earth*, 116(1), pp.1–19.

Chapple, W.M., 1978. Mechanics of thin-skinned fold-and-thrust belts. *Bulletin of the Geological Society of America*, 89(8), pp.1189–1198.

Chen, Y. et al., 2002. New paleomagnetic constraints on central Asian kinematics: Displacement along the Altyn Tagh fault and rotation of the Qaidam Basin. *Tectonics*, 21(5), pp.6–1–6–19.

Craig, T.J., Copley, A. & Jackson, J., 2012. Thermal and tectonic consequences of India underthrusting Tibet. *Earth and Planetary Science Letters*, 353-354, pp.231–239.

Dahlen, F. a, 1990. Critical Taper Model of Fold-And-Thrust Belts and Accretionary Wedges. *Annual Review of Earth and Planetary Sciences*, 18(1), pp.55–99.

Dahlen, F.A., Suppe, J. & Davis, D., 1984. Mechanics of fold-and-thrust belts and accretionary wedges: Cohesive Coulomb Theory. *Journal of Geophysical Research*, 89(B12), pp.10,087–10,101.

Das, S. & Scholz, C.H., 1983. Why large earthquakes do not nucleate at shallow depth. *Nature*, 305(September), pp.621–623. Available at: http://dx.doi.org/10.1038/305621a0.

Davis, D., Suppe, J. & Dahlen, F.A., 1983. Mechanics of fold-and-thrust belts and accretionary wedges. *Journal of Geophysical Research*, 88(B2), pp.1153–1172.

Day, S.M., 1982. Three-dimensional finite difference simulation of fault dynamics: rectangular faults with fixed rupture velocity. Bulletin of the Seismological Society of America, 72(3), pp.705-727.

Duncan, C., Masek, J. & Fielding, E., 2003. How steep are the Himalaya? Characteristics and implications of along-strike topographic variations. *Geology*, 31(1), pp.75–78.

Dziewonski, a. M., Chou, T.-A.T. -a. & Woodhouse, J.H., 1981. Determination of earthquake source parameters from waveform data for studies of global and regional seismicity. *Journal of Geophysical Research*, 86(B4), pp.2825–2852.

Ekström, G., Nettles, M. & Dziewoński, A.M., 2012. The global CMT project 2004-2010: Centroid-moment tensors for 13,017 earthquakes. *Physics of the Earth and Planetary Interiors*, 200-201, pp.1–9.

Elliott, J.R. et al., 2010. Extension on the Tibetan plateau: Recent normal faulting measured by InSAR and body wave seismology. *Geophysical Journal International*, 183(2), pp.503-535.

England, P.C. & Houseman, .G.A., 1988. The mechanics of the Tibetan Plateau. *Philosophical Transactions of the Royal Society A*, 326, pp.301–320.

Fan, W. & Shearer, P.M., 2015. Detailed rupture imaging of the 25 April 2015 Nepal earthquake using teleseismic P waves. *Geophysical Research Letters*, 42(14), pp.5744-5752.

Ferrill, D.A. et al., 2004. Calcite twin morphology: A low-temperature deformation geothermometer. *Journal of Structural Geology*, 26(8), pp.1521–1529.

Fossen, H., 2010. *Structural Geology* 1st ed., Cambridge: Cambridge University press.

Fredrich, J.T., Evans, B. & Wong, T-F., 1989. Micromechanics of the Brittle to Plastic Transition in Carrara Marble. *Journal of Geophysical Research*, 94(B4), pp.4129–4145.

Freed, A.M., 2005. Earthquake Triggering By Static, Dynamic, and Postseismic Stress Transfer. *Annual Review of Earth and Planetary Sciences*, 33(1), pp.335–367.

Grandin, R. et al., 2012. Long-term growth of the Himalaya inferred from interseismic InSAR measurement. *Geology*, 40(12), pp.1059–1062.

Gu, C. et al., 2013. Triggering cascades and statistical properties of aftershocks. *Journal of Geophysical Research: Solid Earth*, 118(8), pp.4278–4295.

Haimson, B. & Chang, C., 2000. A new true triaxial cell for testing mechanical properties of rock, and its use to determine rock strength and deformability of Westerly granite. *International Journal of Rock Mechanics and Mining Sciences*, 37(1-2), pp.285–296.

Helmstetter, A. & Sornette, D., 2002. Diffusion of epicenters of earthquake aftershocks, Omori's law, and generalized continuous-time random walk models. *Physical Review*, 66(6).

Hirschmiller, J. et al., 2014. What controls the growth of the himalayan foreland fold-and-thrust belt? *Geology*, 42(3), pp.247–250.

Hubbard, J. & Shaw, J.H., 2009. Uplift of the Longmen Shan and Tibetan plateau, and the 2008 Wenchuan (M = 7.9) earthquake. *Nature*, 458(7235), pp.194–197.

Hudson, J. & Harrison, J., 2000. *Engineering Rock Mechanics: An Introduction to the Principles* 1st ed., Oxford: Pergamon.

Lin, A., Rao, G. & Yan, B., 2014. Structural analysis of the right-lateral strike-slip qingchuan fault, northeastern segment of the longmen shan thrust belt, central China. *Journal of Structural Geology*, 68(PA), pp.227–244.

Lockner, D.A., 1998. A generalized law for brittle deformation of Westerly granite. *Journal of Geophysical Research*, 103(B3), pp.5107–5123.

Lockner, D.A., 1995. Rock Failure. In T. J. Ahrens, ed. *Rock Physics & Phase Relations*. American Geophysical Union, pp. 127–147.

Masek, J.G. & Duncan, C.C., 1998. Minimum-work mountain building. *Journal of Geophysical Research B: Solid Earth*, 103(1), pp.907–917.

McQuarrie, N., 2004. Crustal scale geometry of the Zagros fold-thrust belt, Iran. *Journal of Structural Geology*, 26(3), pp.519–535.

Meyer, B. et al., 1998. Crustal thickening in Gansu –Qinghai, lithospheric mantle subduction, and oblique, strike –slip controlled growth of the Tibetan plateau. *Geophysical Journal International*, 135, pp.1–48.

Mitchell, T.M. & Faulkner, D.R., 2008. Experimental measurements of permeability evolution during triaxial compression of initially intact crystalline rocks and implications for fluid flow in fault zones. *Journal of Geophysical Research: Solid Earth*, 113(11), pp.1–16.

Miyakawa, A., Yamada, Y. & Matsuoka, T., 2010. Effect of increased shear stress along a plate boundary fault on the formation of an out-of-sequence thrust and a break in surface slope within an accretionary wedge, based on numerical simulations. *Tectonophysics*, 484(1-4), pp.127–138.

Molnar, P. & Lyon-Caen, H., 1988. Some simple physical aspects of the support, structure, and evolution of mountain belts. *Processes in Continental Lithospheric Deformation*, 218, pp.179–207.

Moore, D.E. & Lockner, D.A., 1995. The role of microcracking in shear-fracture propagation in granite. *Journal of Structural Geology*, 17(1), pp.95–114.

Mouthereau, F., Lacombe, O. & Meyer, B., 2006. The Zagros folded belt (Fars, Iran): Constraints from topography and critical wedge modelling. *Geophysical Journal International*, 165(1), pp.336–356.

Nielsen, S.B., Carlson, J.M. and Olsen, K.B., 2000. Influence of friction and fault geometry on earthquake rupture. Journal of Geophysical Research: Solid Earth, 105(B3), pp.6069-6088.

Nissen, E. et al., 2011. New views on earthquake faulting in the Zagros fold-and-thrust belt of Iran. *Geophysical Journal International*, 186(3), pp.928–944.

De Paola, N., Faulkner, D.R. & Collettini, C., 2009. Brittle versus ductile deformation as the main control on the transport properties of low-porosity anhydrite rocks. *Journal of Geophysical Research: Solid Earth*, 114(6).

Passchier, C.W. & Trouw, R.A.J., 2005. *Microtectonics* 2nd ed., Berlin: Springer Berlin Heidelberg.

Paterson, M.S. & Wong, T.F., 2005. *Experimental rock deformation - The brittle field* 1st ed., Berlin: Springer Berlin Heidelberg.

Paul, A. et al., 2010. Seismic imaging of the lithospheric structure of the Zagros mountain belt (Iran). *Geological Scociety of London*, 330, pp.5–18.

Petr, T. & Swar, D., 2002. Cold Water Fisheries in the Trans-Himalayan Countries. *FAO Fisheries Technical Paper*, 431, p.376.

Pieri, M. et al., 2001. Rheological and microstructural evolution of Carrara marble with high shear strain: Results from high temperature torsion experiments. *Journal of Structural Geology*, 23(9), pp.1393–1413.

Roe, G.H. & Brandon, M.T., 2011. Critical form and feedbacks in mountain-belt dynamics: Role of rheology as a tectonic governor. *Journal of Geophysical Research: Solid Earth*, 116(2), pp.1–17.

Scholz, C., Molnar, P. & Johnson, T., 1972. Detailed studies of frictional sliding of granite and implications for the earthquake mechanism. *Journal of Geophysical Research*, 77(32), pp.6392–6406.

Scholz, C.H., 1968. The frequency-magnitude relation of microfracturing in rock and its relation to earthquakes. *Bulletin of the Seismological Society of America*, 58(1), pp.399–415.

Schubnel, A. et al., 2006. Transient creep, aseismic damage and slow failure in Carrara marble deformed across the brittle-ductile transition. *Geophysical Research Letters*, 33(17), pp.1-6.

Serdengecti, S. & Boozer, G.D., 1961. The effects of strain rate and temperature on the behaviour of rocks subject to triaxial compression. In *Proceedings of the 4th U.S. Symposium on Rock Mechanics (USRMS)*. American Rock Mechanics Association, pp. 83–97.

Shcherbakov, R., Turcotte, D.L. & Rundle, J.B., 2004. A generalized Omori's law for earthquake aftershock decay. *Geophysical Research Letters*, 31(11), pp.1–5.

Shipton, Z.K. et al., 2006. The Missing Sinks: Slip Localization in Faults, Damage Zones, and the Seismic Energy Budget. *Earthquakes: Radiated Energy and the Physics of Faulting*, pp.217–222.

Sibson, R.H., 1989. Earthquake faulting as a structural process. *Journal of Structural Geology*, 11(1-2), pp.1–14.

Sloan, R.A. et al., 2011. Earthquake depth distributions in central Asia, and their relations with lithosphere thickness, shortening and extension. *Geophysical Journal International*, 185(1), pp.1–29.

Styron, R., Taylor, M. & Sundell, K., 2015. Accelerated extension of Tibet linked to the northward underthrusting of Indian crust. *Nature Geoscience*, 8(2), pp.131–134.

Sun, C. et al., 2016. Sandbox modeling of evolving thrust wedges with different preexisting topographic relief: Implications for the Longman Shan thrust belt, eastern Tibet. *Journal of Geophysical Research: Solid Earth*, 121, pp.1–16.

Talebian, M. & Jackson, J., 2004. A reappraisal of earthquake focal mechanisms and active shortening in the Zagros mountains of Iran. *Geophysical Journal International*, 156(3), pp.506–526.

Tapponnier, P. et al., 2001. Oblique Stepwise Rise and Growth of the Tibet Plateau. *Science*, 294(5547), pp.1671–1677.

Taylor, M. & Yin, a., 2009. Active structures of the Himalayan-Tibetan orogen and their relationships to earthquake distribution, contemporary strain field, and Cenozoic volcanism. *Geosphere*, 5(3), pp.199–214.

Tullis, J. & Yund, R. a., 1977. Experimental deformation of dry westerly granite. *Journal of Geophysical Research*, 82(36), pp.5705–5718.

Vallée, M., 2013. Source time function properties indicate a strain drop independent of earthquake depth and magnitude. *Nature communications*, 4.

Vanderhaeghe, O. et al., 2003. Evolution of orogenic wedges and continental plateaux: Insights from crustal thermal-mechanical models overlying subducting mantle lithosphere. *Geophysical Journal International*, 153(1), pp.27–51.

Vernant, P. et al., 2004. Present-day crustal deformation and plate kinematics in the Middle East constrained by GPS measurements in Iran and northern Oman. *Geophysical Journal International*, 157(1), pp.381–398.

Wang, K. & Hu, Y., 2006. Accretionary prisms in subduction earthquake cycles: The theory of dynamic Coulomb wedge. *Journal of Geophysical Research: Solid Earth*, 111(6), pp.1–16.

Williams, C. et al., 1994. Effect of the Brittle-Ductile Transition on the Topography of Compressive Mountain Belts on Earth and Venus. *Journal of Geophysical Research-Solid Earth*, 99(B10), pp.19,947–19,974.

Wong, L.N.Y. & Einstein, H.H., 2009. Crack coalescence in molded gypsum and carrara marble: Part 1. macroscopic observations and interpretation. *Rock Mechanics and Rock Engineering*, 42(3), pp.475–511.

Wong, T.F., 1982. Micromechanics of faulting in westerly granite. *International Journal of Rock Mechanics and Mining Sciences and*, 19(2), pp.49–64.

Yin, A. et al., 2008a. Cenozoic tectonic evolution of Qaidam basin and its surrounding regions (Part 1): The southern Qilian Shan-Nan Shan thrust belt and northern Qaidam basin. *Bulletin of the Geological Society of America*, 120(7-8), pp.813–846.

Yin, A. et al., 2008b. Cenozoic tectonic evolution of the Qaidam basin and its surrounding regions (Part 3): Structural geology, sedimentation, and regional tectonic reconstruction. *Bulletin of the Geological Society of America*, 120(7-8), pp.847–876.

Zhang, P.Z. et al., 2004. Continuous deformation of the Tibetan Plateau from global positioning system data. *Geology*, 32(9), pp.809–812.

Zhang, S., Cox, S.F. & Paterson, M.S., 1994. The influence of room temperature deformation on porosity and permeability in calcite aggregates. *Journal of Geophysical Research*, 99(B8), pp.15,761–15,775.